solids

MDPI

Review

Luminescence Properties of Defects in GaN: Solved and Unsolved Problems

Michael A. Reshchikov

Department of Physics, Virginia Commonwealth University, Richmond, VA 23220, USA; mreshchi@vcu.edu

Abstract

Gallium Nitride (GaN) is a wide-bandgap semiconductor that has revolutionized optoelectronic applications, enabling blue/white light-emitting devices and high-power electronics. Point defects in GaN strongly influence its optical and electronic properties, producing both beneficial and detrimental effects. This review provides a comprehensive update on the current understanding of point defects in GaN and their impact on photoluminescence (PL). Since our earlier review (Reshchikov and Morkoç, *J. Appl. Phys*. **2005**, *97*, 061301), substantial progress has been made in this field. PL bands associated with major intrinsic and extrinsic defects in GaN are now much better understood, and several defects in undoped GaN (arising from unintentional impurities or specific growth conditions) have been identified. Notably, the long-debated origin of the yellow luminescence band in GaN has been resolved, and the roles of Ga and N vacancies in the optical properties of GaN have been revised. Zero-phonon lines have been discovered for several defects. Key parameters, such as electron- and hole-capture coefficients, phonon energies, electron–phonon coupling strength, thermodynamic charge transition levels, and the presence of excited states, have been determined or refined. Despite these advances, several puzzles associated with PL remain unsolved, highlighting areas for future investigation.

Keywords: photoluminescence; GaN; semiconductors; point defects; yellow band

Academic Editor: Ling Huang

Received: 2 July 2025
Revised: 25 July 2025
Accepted: 1 September 2025
Published: 10 September 2025

Citation: Reshchikov, M.A. Luminescence Properties of Defects in GaN: Solved and Unsolved Problems. *Solids* **2025**, *6*, 52. https://doi.org/10.3390/solids6030052

1. Introduction

Gallium nitride (GaN), a wide-bandgap semiconductor with a direct bandgap of 3.43 eV at room temperature, is a cornerstone of modern optoelectronics and power electronics. Applications include bright blue and white light-emitting diodes (LEDs), blue lasers, and high-power and high-frequency electronic devices. Its outstanding material properties, including a high breakdown voltage and the availability of both *n*- and *p*-type doping, have established GaN as a key platform for next-generation semiconductor technologies [1–4]. However, defects significantly degrade optical and electrical performance. While structural defects are well-characterized, point defects—including vacancies, interstitials, antisites, impurities, and their complexes—remain insufficiently understood. Identifying and characterizing these defects is essential for improving the efficiency, reliability, and operational lifetime of GaN-based devices.

Point defects in GaN are probed using a wide range of experimental techniques, including photoluminescence (PL), cathodoluminescence (CL), secondary ion mass spectrometry (SIMS), Hall effect measurements, positron annihilation spectroscopy (PAS), Raman and Fourier-transform infrared (FTIR) spectroscopy, deep-level transient spectroscopy (DLTS), electron paramagnetic resonance (EPR), and optically detected magnetic resonance

(ODMR) [5]. Among these, PL stands out as the most versatile and widely used method for probing optically active defects. PL enables the determination of key defect parameters, such as concentration, charge states, charge transition levels (with ~1 meV precision), carrier capture coefficients, electron–phonon coupling strengths, and excited-state characteristics. While excitonic luminescence, or, in general, near-band-edge (NBE) emission in GaN is well-understood [6–16], the origins of broad defect-related PL bands remain controversial. Persistent misattributions in the literature have hindered progress in the field.

The review by Reshchikov and Morkoç (2005) [16] provided a comprehensive analysis of PL in undoped and intentionally doped GaN. Since then, advances in material growth, experimental techniques, and first-principles calculations, particularly density functional theory (DFT), have prompted substantial revisions to earlier models. For example, the carbon impurity on a nitrogen site (C_N) was previously misidentified as a shallow acceptor with a $-/0$ charge transition level ~0.2 eV above the valence band maximum (VBM) [17–22], and was believed to be responsible for the ultraviolet luminescence (UVL) band at 3.28 eV [23]. However, modern DFT calculations and experimental evidence have reclassified C_N as a *deep* acceptor with a $-/0$ level at 0.9 eV above the VBM, now linked to the yellow luminescence (YL) band centered at ~2.2 eV [24–27]. Another illustrative case concerns the role of the gallium vacancy (V_{Ga}) and its complex with oxygen ($V_{Ga}O_N$) in PL from GaN. Early DFT calculations [17,22] and the results of PAS experiments [28] led to the incorrect conclusion that transitions from the conduction band (or shallow donors) to these defects cause the YL band in undoped GaN [16]. More accurate calculations have since revised the energy levels of V_{Ga} and $V_{Ga}O_N$ by 1–2 eV [29–32], and recent experimental findings conclusively rule out their contribution to YL in undoped GaN (Section 3.1.5).

Although many controversies surrounding defect-related PL in GaN have been resolved since 2005, incorrect attributions, outdated theoretical interpretations, and misinterpretations of experimental data persist in the literature. This review aims to consolidate and disseminate an updated understanding of PL arising from major point defects in wurtzite GaN, with a focus on areas where significant revisions have been made. PL phenomena associated with excitons, structural defects, alloys, low-dimensional structures, transition metals, or rare-earth elements are beyond the scope of this work.

Table 1 summarizes the principal PL bands and their updated parameters. Figure 1 illustrates the corresponding electronic transitions schematically.

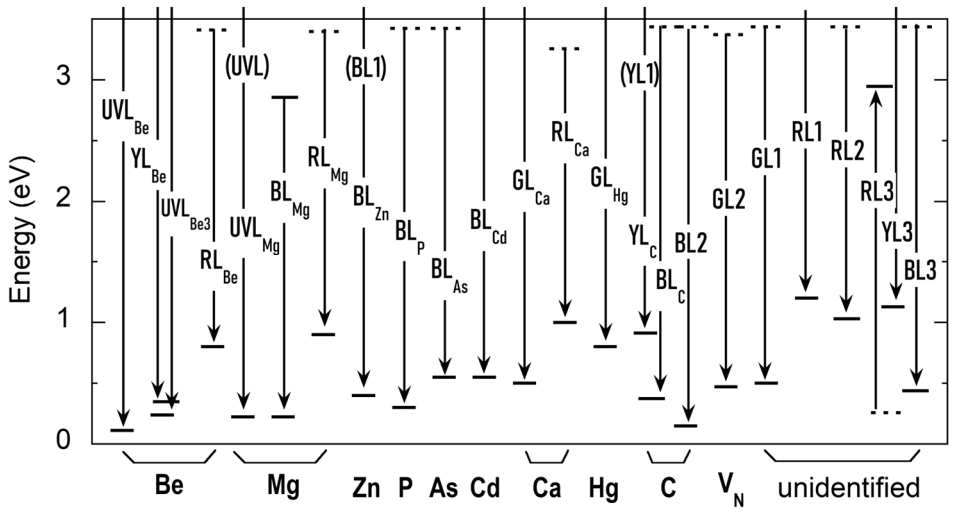

Figure 1. Band diagram with main radiative transitions and names of PL bands in undoped GaN and GaN doped with major impurities (limited to GaN grown by MOCVD, MBE, and HVPE).

Table 1. Classification and main parameters of defect-related PL bands in GaN.

Dopant	PL Band	$\hbar\omega_{max}$ (eV)	ZPL (eV)	E_A (eV)	FWHM (eV)	C_p (cm^3s^{-1})	C_n (cm^3s^{-1})	τ (μs) [a]	Attribution	Comments	Ref.
C	RL_C	1.62							C_N-C_{Ga}-C_N ?	[C] > 10^{18} cm^{-3}	[33]
–	RL1	1.75		~1.1	0.42	3×10^{-7}	4.3×10^{-14}		Cl? (−/0)?	HVPE GaN	[34]
–	RL2	1.74		~1	0.35			1000	AV_N? (0/+)?	SI, Ga-rich GaN	[16,35–37]
Mg	RL_{Mg}	1.67		~0.9	0.41			1.3	$Mg_{Ga}V_N$ (0/+)		[36]
Be	RL_{Be}	1.77		~0.8	0.44			3	$Be_{Ga}V_N$ (0/+)		[36]
Ca	RL_{Ca}	1.82		~1.0	0.43			1900	$Ca_{Ga}V_N$ (0/+)		[36]
–	RL3	1.77		~2.8	0.38	~10^{-5}		0.010	RY3 (−/0)	HVPE GaN	[38]
–	RL4	1.6–1.7		~1.2	~0.44				$V_{Ga}3O_N$? (0/+)?	AT GaN	[39]
F,Cl,Cd,Ca,Hg	RL5	~1.6							?	Implantation damage	
F	OL1	1.88			~0.47				$V_{Ga}F_N$?		
-	OL3	2.09			~0.47				$V_{Ga}O_N2H_i$? (0/+)?	AT GaN	[39]
– C	YL1, YL_C	2.19	2.59	0.916	0.43	3.7×10^{-7}	1.1×10^{-13}		C_N (−/0)	Omnipresent, MOCVD	[25,40,41]
–	YL2	2.3		~0.6	~0.49				$V_{Ga}3H_i$? (0/+)?	AT GaN	[39,41,42]
–	YL3	2.07	2.38	1.130	0.40	~10^{-7}	2×10^{-13}		RY3 (−/0)	HVPE GaN	[38,41,43,44]
Be	YL_{Be}	2.15		0.34	0.57	~1×10^{-6}	1×10^{-13}		Be_{Ga} (−/0)	YL_{Be1}, YL_{Be2}	[45,46]
–	GL1	2.35		~0.5	0.48			1	? (0/+)	HVPE GaN	[34]
–	GL2	2.33		~0.5	0.24			300	V_N (+/2+)	SI, Ga-rich GaN	[34,47]
Hg	GL_{Hg}	2.44		0.8	0.39	(1–5) × 10^{-7}	3×10^{-13}		Hg_{Ga} (−/0)		[48]
– Ca	GL_{Ca}	2.49		0.50	0.43	6×10^{-7}	1×10^{-13}		Ca_{Ga} (−/0)	undoped MBE	[49]
– Zn	BL1, BL_{Zn}	2.86	3.10	0.400	0.36	5×10^{-7}	6.8×10^{-13}		Zn_{Ga} (−/0)	Dual nature?	[34,50–54]
– C	BL2	3.00	3.33	0.15	0.42	4.5×10^{-8}		0.3	C_NH_i (0/+)	Bleaching	[55]
–	BL3	2.8	3.01	~0.46	0.45	~10^{-9}		0.001	RY3 (0/+)	HVPE GaN	[56]
P	BL_P	2.89	3.20	0.29	0.37				P_N (0/+)		[57,58]
As	BL_{As}	2.6	2.95	0.54	~0.4			0.09	As_N (0/+)		[57]
Cd	BL_{Cd}	2.70	2.95	0.55	0.35	3×10^{-7}	2.6×10^{-13}		Cd_{Ga} (−/0)		[48,59]
C	BL_C	2.85	3.15	0.33	~0.43	10^{-10} ?		0.001	C_N (0/+)		[25,60]
Be	BL_{Be}	2.6		0.15	0.57	~10^{-8}		0.8	Be_{Ga} (0/+) ?		[61]
Mg	BL_{Mg}	~2.8		0.22	~0.3				DD→Mg_{Ga}	Large shifts	[62,63]
– Mg	UVL, UVL_{Mg}	3.28	3.28	0.223	0.01	1×10^{-6}	3.2×10^{-12}		Mg_{Ga} (−/0)	Dual nature?	[40,62,63]
Be	UVL_{Be}	3.38	3.38	0.113	0.01	~1×10^{-6}	1×10^{-11}		$Be_{Ga}O_NBe_{Ga}$ (−/0)	Dual nature?	[64]

[a] τ at $T \approx 18$ K for internal transitions, independent of n.

Traditionally, PL bands in GaN are labeled according to their perceived emission color, such as red luminescence (RL) or green luminescence (GL). However, multiple defects can produce PL bands with similar spectral positions and overlapping hues, leading to ambiguity. To address this, we adopt a refined nomenclature introduced in Ref. [65], which supplements traditional band names with numerical or index-based identifiers. For instance, the GL band described in Ref. [16] is now designated GL1, while GL2 retains its original classification.

The most important changes and remaining challenges in understanding defect-related PL in GaN (in the author's opinion) are summarized below.

Solved problems:

- The YL band (2.2 eV) in undoped GaN is now conclusively attributed to the C_N acceptor (Section 3.1.2). Remaining issue: Reliable experimental data are lacking for the charge transition levels and PL signatures of V_{Ga} and $V_{Ga}O_N$ complexes (Sections 3.1.5 and 3.6).
- The UVL band (3.28 eV) in undoped GaN originates from the Mg_{Ga} acceptor, and not from C_N, Si_{Ga}, V_{Ga}-related, or structural defects (Section 3.5). Remaining issue: The theoretically predicted dual nature of the Mg_{Ga} acceptor has not been confirmed experimentally (Section 4.3.2).
- The GL2 and RL2 bands are associated with isolated nitrogen vacancies (V_N) and the AV_N complexes, where A denotes a cation-site acceptor (Sections 3.2.2 and 3.3.2). Remaining questions: What is A in the RL2 from undoped GaN? Is there PL from the AV_N complexes with A = Zn_{Ga}, Cd_{Ga}, or Hg_{Ga}? Can GL2 and RL2 be linked to different charge transition levels of these multi-charged defects?
- The fundamental properties of the isolated Be_{Ga} acceptor have been well established (Section 4.2.2). Remaining uncertainties: The identities of the shallow acceptor and deep donor responsible for the UVL_{Be} (3.38 eV) and BL_{Be} (2.6 eV) bands, respectively, should be verified (Sections 4.2.3 and 4.2.5).
- The origin of the aquamarine band in undoped GaN has been clarified (Section 4.6.2).
- Novel mechanisms of PL quenching emerged (Sections 2.2.2 and 4.4.2).
- Significant redshifts of PL bands with decreasing excitation intensity have been explained (Sections 4.3.4 and 4.4.5).

Unsolved problems:

- The predicted dual nature of acceptors (excluding Be_{Ga}) remains unverified experimentally (Sections 4.3.2 and 4.4.1).
- The origins of the GL1 and RL1 bands are still unknown (Sections 3.2.1 and 3.3.1).
- The RY3 defect remains unidentified (Section 3.1.4, Section 3.2.3, and Section 3.4.3).
- The influence of mobile defects at growth temperatures on the formation of complexes is not yet fully understood.
- The effect of the surface and structural defects on PL from point defects remains insufficiently explored.
- Significant discrepancies persist between predictions of first-principles calculations and experimental observations (Section 5.6).

The structure of the Review is the following. Section 2 outlines specific methodologies for conducting and analyzing PL experiments. Sections 3 and 4 review PL bands in undoped and doped GaN, respectively. Section 5 summarizes key developments since the previous review [16] and highlights unresolved issues. Section 6 concludes.

2. Luminescence Methods

2.1. Photoluminescence Setup

Steady-state PL (SSPL) and time-resolved PL (TRPL) measurements, conducted over a wide range of temperatures and excitation intensities, are basic techniques for probing defect-related luminescence in GaN [16]. Figure 2 illustrates a schematic of a typical PL setup, employing a continuous-wave HeCd laser (λ = 325.03 nm) for SSPL and a pulsed nitrogen laser (λ = 337 nm) for TRPL. Detailed descriptions of the experimental configuration are provided elsewhere [25,66].

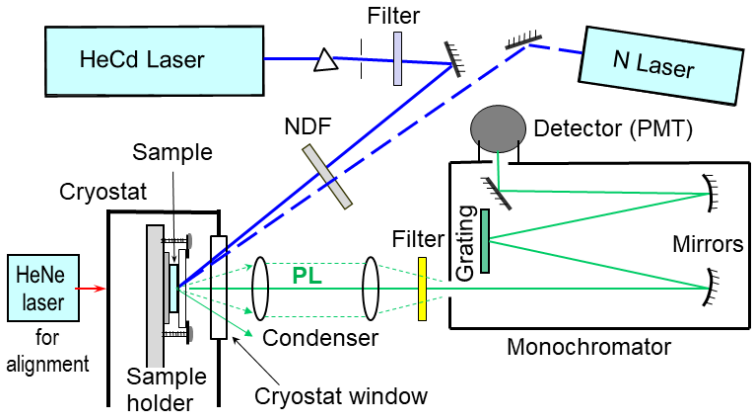

Figure 2. Schematics of the PL experiment. NDF is a neutral density filter, and PMT is a photomultiplier tube.

Since 2018, an improved approach to PL spectral presentation has been proposed to ensure consistency between experimentally measured spectra and theoretically calculated band shapes [25]. As before, as-measured spectra are corrected for the spectral response of the detection system. In addition, the PL intensity is now scaled by a factor of λ^3, where λ is the emission wavelength, so that spectra are expressed in units proportional to the number of emitted photons as a function of photon energy $\hbar\omega$. These corrections are applied to PL spectra throughout this review (except for Figure 18a, Figure 26a, Figure 35, Figure 36, Figure 37a and Figure 39a). Note that positions and shapes of broad PL bands associated with the same defect may vary when measured on different setups unless proper corrections are applied, partly explaining discrepancies in the literature [66].

The internal quantum efficiency (IQE) of individual PL bands, η, can be estimated by integrating the corrected band intensity and comparing it with that of calibrated GaN standards, as described in previous works [34,52,53]. Challenges associated with measuring external quantum efficiency (EQE) of PL and accurately deriving η have recently been addressed in detail [67–71].

2.2. Phenomenological Models for Defect-Related PL in GaN

Phenomenological models, based on rate equations inspired by the Shockley-Read-Hall formalism [72,73], enable the extraction of key parameters from SSPL and TRPL data, thereby facilitating the identification of defect-related PL bands in semiconductors [65,74,75]. These models, refined specifically for defects in GaN [52,53,76,77], describe carrier recombination dynamics and defect properties, including electron- and hole-capture coefficients, ionization energies, and defect concentrations.

2.2.1. TRPL and Electron-Capture Coefficient

The radiative electron-capture coefficient C_n for a defect (Table 1) can be determined from the PL lifetime τ_0 when the PL arises from electron transitions from the conduction band to the defect level (e-A transitions). The relationship is given by [65,77]:

$$C_n = \frac{1}{n\tau_0} \quad (1)$$

where n is the free electron concentration, typically obtained via Hall effect measurements. Once C_n is determined for a specific PL band, it can be used to estimate n in other GaN samples [65]. For not purely exponential PL decay, such as when e-A and donor-acceptor-pair (DAP) transitions overlap, the effective PL lifetime τ_0* can be extracted from the maximum of the $t \cdot I^{PL}(t)$ dependence [78].

2.2.2. Temperature Dependence of PL and Hole-Capture Coefficient

The nonradiative hole-capture coefficient C_p for a defect (Table 1) can be derived from the temperature dependence of PL intensity, I^{PL}, or PL lifetime, τ. Above a critical temperature T_0, both the I^{PL} and τ decrease exponentially with increasing temperature in an Arrhenius plot—a phenomenon known as PL quenching. For defects in *n*-type GaN, PL quenching arises from the thermal emission of holes from defect levels to the valence band via the Schön–Klasens mechanism [74]. For PL driven by e-A transitions, the $I^{PL}(T)$ and $\tau(T)$ dependences are described with the following expression:

$$\frac{I^{PL}(T)}{I^{PL}(0)} = \frac{\tau(T)}{\tau_0} = \frac{1}{1 + C\exp\left(\frac{-E_A}{kT}\right)} \quad (2)$$

where $C = (1 - \eta_0)\tau_0\ C_p\ N_v\ g^{-1}$; $\eta_0 = \eta$ and $\tau_0 = \tau$ at $T < T_0$; $N_v = 2(2\pi m_p{}^* kT)^{3/2}h^{-3}$ is the effective density of states in the valence band; $m_p{}^*$ is the hole effective mass, k is Boltzmann's constant; g is the defect level degeneracy; and E_A is the activation energy (defect ionization energy), equal to the energy difference between the defect level and the VBM plus any potential barrier to hole capture [52,53]. Note that the values of C_p in Table 1 are calculated under the assumption that $m_p{}^* = 0.8m_0$ and $g = 2$. If these parameters differ, C_p must be scaled by a factor of $0.36g(m_p{}^*)^{-3/2}$. In DLTS measurements, C_p can be found with a similar approach. However, the common practice in DLTS analysis is to calculate the hole-capture cross-section, σ_p. The two quantities are related via $C_p = \langle v_p \rangle \sigma_p$, where $\langle v_p \rangle = (3kT/m_p{}^*)^{1/2}$ is the mean thermal velocity of holes in the valence band.

In semi-insulating (SI) GaN, PL quenching often occurs via a tunable and abrupt quenching (TAQ) mechanism [52]. Although $I^{PL}(T)$ can be formally fitted using Equation (2), the parameters C and E_A lack direct physical meaning in this case. The apparent E_A may significantly exceed the true ionization energy (abrupt quenching), and T_0 increases with excitation intensity P_{exc} (tunable quenching). For such samples, the defect ionization energy is instead obtained from

$$E_A = kT_0 \ln\left(\frac{B'}{P_{exc}}\right), \quad (3)$$

where B' depends on C_p and relative concentrations of defects involved in recombination [52]. The nonlinear rate equations governing carrier dynamics in SI semiconductors can lead to counterintuitive behavior, necessitating numerical simulations for accurate analysis [52,79]. The TAQ mechanism resembles a phase transition: at $T < T_0$, recombination (including PL) is dominated by defects with high hole-capture efficiency, whereas at $T > T_0$, defects with faster electron capture dominate in recombination.

2.2.3. Excitation Intensity Dependence

The defect concentration N can be found from the dependence of SSPL intensity on the excitation photon flux, P, modeled as:

$$\frac{I^{PL}(P)}{I_0^{PL}} = \frac{\eta(P)}{\eta_0} = \frac{P_0}{P}\ln\left(1 + \frac{P}{P_0}\right), \quad (4)$$

where $P_0 = N(\eta_0 \alpha \tau_0)^{-1}$ [80,81]. Here, ${I_0}^{PL}$ and η_0 denote the PL intensity and the absolute IQE, respectively, in the limit of low excitation intensity, and α is the absorption coefficient for incident photons (1.2×10^5 cm^{-1} at 325 nm for GaN [82]). For TRPL, Equation (4) applies with τ_0 replaced by the laser pulse duration t_L [77]. The accuracy of N is limited by uncertainties in η_0 [83]. However, relative defect concentrations for a given sample can be

determined with higher precision, as the light-extraction efficiency—a primary source of η_0 uncertainty—is approximately the same for different PL bands in a given sample.

Once relative concentrations of radiative defects in a particular sample are known, the relative hole-capture coefficients for PL bands can be obtained because, according to Equation (2),

$$\frac{C_{pi}}{C_{pj}} = \frac{I_i^{PL}}{I_j^{PL}} \frac{N_j}{N_i} \tag{5}$$

where I_i^{PL}/I_j^{PL} is the ratio of integrated PL intensities for PL bands i and j at $T < T_0$, and N_i, N_j are the respective defect concentrations. If C_p is known for a reference defect (e.g., the C_N acceptor responsible for the YL1 band), Equation (5) enables the determination of C_p for other defects.

2.3. Configuration Coordinate Model for Defect-Related PL

Parameters associated with electron–phonon coupling can be extracted from PL band shapes modeled within a one-dimensional configuration coordinate framework. The spectral shapes of broad PL bands can be fitted using the expression [47]:

$$I^{PL}(\hbar\omega) = I^{PL}(\hbar\omega_{\max}) \exp\left[-2S_e\left(\sqrt{\frac{E_0^* - \hbar\omega + \Delta}{d_{FC}^g}} - 1\right)^2\right] \tag{6}$$

Here, S_e is the Huang–Rhys factor for the excited state of the defect, $d_{FC}{}^g = E_0{}^* - \hbar\omega_{\max}$ is the Franck–Condon shift in the ground state, $E_0{}^* = E_0 + 0.5\hbar\Omega_e$, E_0 is the zero-phonon line (ZPL) energy, $\hbar\Omega_e$ is the effective phonon mode energy in the excited state, $\hbar\omega$ is the photon energy, $\hbar\omega_{\max}$ is the PL band maximum, and Δ is a sample-dependent energy shift (<20 meV) arising from factors such as in-plane biaxial strain in GaN thin layers on sapphire substrates or local electric fields. Typical values of these parameters for broad PL bands are summarized in Table 2.

Note that, unless the ZPL is explicitly identified, parameters $E_0{}^*$ (or $d_{FC}{}^g$) and S_e remain ambiguous; namely, similar PL band shapes can be obtained by simultaneous increase (or decrease) of these parameters [34]. Nevertheless, three parameters from Table 2 (e.g., $E_0{}^*$, $\hbar\omega_{\max}$, and S_e) are sufficient to define bands' positions and shapes, allowing distinctive defect-related PL bands in GaN to be recognized (provided appropriate corrections are applied to as-measured low-temperature PL spectra), and overlapped PL bands to be deconvoluted.

The effective phonon energy $\hbar\Omega_e$ can be extracted from the temperature dependence of the PL band's full width at half maximum (FWHM), $W(T)$. For a Gaussian-like PL band shape, the FWHM is modeled by [16,47]:

$$W(T) = W_0\sqrt{\coth\left(\frac{\hbar\Omega_e}{2kT}\right)} \tag{7}$$

where W_0 is the FWHM at $T = 0$. Values of W_0 and $\hbar\Omega_e$ for selected broad PL bands are listed in Table 2.

Table 2. Vibrational parameters of broad PL bands (at low temperatures).

PL Band	$\hbar\omega_{max}$ (eV)	E_0* (eV)	S_e	$d_{FC}{}^g$ (eV)	W_0 (eV)	$\hbar\Omega_e$ (eV)
RL1	1.73	2.3	9.5	0.57	0.42	
RL2	1.74	2.3	12.5	0.56	0.35	0.033
RL_{Mg}	1.67	2.6	27	0.93	0.41	
RL_{Be}	1.78	2.65	20	0.87	0.44	0.042
RL_{Ca}	1.82	2.23	15	0.41	0.25	0.027
RL4	1.6–1.7	2.26	9	0.56–0.66	0.44	
OL1	1.88	2.6	12	0.72	0.47	
OL3	2.09	2.8	13	0.71	0.47	
YL1	2.17	2.67	7.8	0.50	0.43	0.056
YL2	2.30	2.86	7.3	0.56	0.49	
YL3	2.07	2.45	5.0	0.38	0.40	0.06
YL_{Be}	2.15	3.2	24	1.05	0.52	0.038
GL1	2.35	2.97	10.3	0.62	0.48	0.041
GL2	2.33	2.70	13.5	0.24	0.24	0.023
GL_{Hg}	2.44	2.7	5	0.26	0.39	0.053
GL_{Ca}	2.49	3.02	8.5	0.53	0.43	0.041
BL1	2.86	3.10	3.2	0.36	0.36	0.043
BL2	3.00	3.38	4.6	0.38	0.42	
BL3	2.81	3.08	2.0	0.27	0.45	
BL_{Cd}	2.70	3.0	4.0	0.3	0.35	0.053
BL_C	2.85	3.20	3.7	0.35	0.43	
BL_P	2.88				0.37	0.050
BL_{Be}	2.6	3.4	12	0.8	0.57	
BL_{Mg}	2.8	3.1	5.0	0.4	0.31	

2.4. Electron Transition Mechanisms

Analysis of PL provides insights into the nature of electronic transitions responsible for defect-related luminescence [66]. In *n*-type GaN, at low temperatures (T < 50 K), most PL bands originate from DAP recombination, involving shallow donors and various acceptors [84,85]. The high efficiency of the DAP transitions at low temperatures arises from the extended electron wavefunctions for shallow donors, which overlap substantially with acceptor states. These PL bands exhibit a blueshift of up to ~10 meV as excitation intensity P_{exc} increases from 10^{-5} to 0.3 Wcm^{-2} [16,40,44,62], since emission from distant DAPs, contributing at lower photon energies due to weaker Coulomb interactions, saturates at lower P_{exc}. The PL decay following a laser pulse is nonexponential in this regime (often exhibiting the t^{-m} dependence with $m \approx 1$), reflecting the distribution of DAP separations [85]. At elevated temperatures, transitions from the conduction band to the same acceptors (the e-A transitions) dominate, gradually replacing DAP recombination. In this regime, the PL decay becomes exponential, with a characteristic lifetime τ_0, which is inversely proportional to the concentration of free electrons, see Equation (1).

PL from deep donors in GaN is typically caused by internal transitions: from an excited state (located near the conduction band) of a positively charged donor to its ground

state [66]. These transitions yield exponential PL decays even at very low temperatures, with τ_0 independent of n (Table 1).

DAP transitions involving deep donors are rarely observed in GaN. A notable exception is the BL_{Mg} band, which shifts from ~2.8 to 2.94 eV as P_{exc} increases from 10^{-6} to 0.3 Wcm^{-2} [62]. This band is attributed to electron transitions from an unidentified deep donor to the shallow Mg_{Ga} acceptor, as discussed in Section 4.3.3. The strongly localized electron wavefunction for the deep donor requires small DAP separations for efficient recombination, thereby restricting the BL_{Mg} band to heavily Mg-doped GaN ([Mg] > 10^{18} cm^{-3}) [62]. Note that large PL band shifts (up to 0.5 eV) with varying P_{exc} may also arise from potential fluctuations in SI GaN or due to local electric fields induced by structural defects or the surface [54]. For instance, the UVL_{Mg} band can exhibit a giant redshift and broadening with decreasing P_{exc}, potentially causing confusion with the BL_{Mg} band [54,62].

3. Luminescence Associated with Defects in Undoped GaN

Over the past two decades, there has been significant progress in explaining defect-related PL in undoped GaN and resolving longstanding controversies, most notably the origin of the yellow luminescence (YL) band. Several PL bands in nominally undoped GaN arise from unintentional impurities such as Mg_{Ga}, Zn_{Ga}, Ca_{Ga}, and C_N, which are responsible for the UVL, BL1, GL_{Ca}, and YL1 bands, respectively. Additionally, the GL2 and RL2 bands, observed in SI GaN, have been attributed to V_N and the V_N-acceptor complexes. Conversely, the RL1 and GL1 bands in GaN grown by hydride vapor phase epitaxy (HVPE) technique remain unidentified, though a better understanding has emerged. A novel defect, tentatively assigned to Fe and labeled RY3, has recently been recognized in undoped HVPE GaN. Importantly, V_{Ga}-related defects have been ruled out as sources of any observed PL bands in undoped GaN. The following sections classify defect-related PL bands in undoped GaN by color and provide concise analyses.

3.1. Yellow Luminescence in Undoped GaN (YL1, YL2, YL3)

3.1.1. Historical Overview

The YL band with a maximum at about 2.2 eV is the dominant defect-related PL feature observed in both undoped and doped GaN across various growth techniques, including HVPE, metal–organic chemical vapor deposition (MOCVD), and molecular beam epitaxy (MBE) [41]. Its microscopic origin, a subject of debate for nearly four decades, has now been conclusively identified. Early studies by Ogino and Aoki [86] provided compelling evidence linking the YL band to carbon impurities. In contrast, Pankove and Hutchby [87] observed the YL band in GaN implanted with 35 different ions, with negligible intensity in unimplanted controls, suggesting that implantation-induced native defects, such as V_{Ga}, were responsible for it. Supporting this view, early DFT calculations predicted that electron transitions from the conduction band to deep acceptor levels, namely the $3-/2-$level of V_{Ga} and the $2-/-$ level of the $V_{Ga}O_N$ complex, calculated at ~1.1 eV above the VBM, caused the YL band [22]. PAS experiments further seemed to support this model by suggesting a correlation between YL intensity and V_{Ga} concentration [28]. During this period, multiple competing hypotheses were proposed regarding both the identity of the defect responsible for YL and the nature of the optical transition involved [16].

Nevertheless, accumulating experimental evidence pointed to carbon as the source of the YL band [88]. Although early DFT calculations misidentified C_N as a shallow acceptor with a predicted $-/0$ level at ~0.2 eV above the VBM [20,22], more accurate hybrid functional DFT calculations have since corrected this assignment. These modern

calculations place the C_N $-/0$ transition level at 0.9 eV above the VBM, confirming that C_N acts as a deep acceptor and is the primary candidate for the YL band [24].

At one point, a widely accepted view prevailed that several distinct defects could produce YL bands with similar shapes and positions [29,89–92]. In particular, Armitage et al. [89] suggested that the YL band in undoped GaN originates from V_{Ga}-related defects, while a nearly indistinguishable YL band in C-doped GaN is caused by C-related defects. However, current experimental evidence definitely attributes the YL band at ~2.2 eV in undoped GaN—referred to as YL1—to the isolated C_N acceptor. The prominence of YL1 is especially notable in GaN grown by MOCVD, where residual carbon contamination is unavoidable. Nonetheless, the YL1 band may also be observed in HVPE- and MBE-grown GaN, even when carbon levels fall below the SIMS detection limit of ~10^{16} cm^{-3}. The prominence of the YL band stems from the high hole-capture efficiency of C_N acceptors, which outcompete nonradiative or weakly radiative defects introduced by contamination, doping, or ion implantation.

Additional yellow luminescence bands include the YL_{Be} band, induced by intentional doping or implantation with Be (Section 4.2.2), and the YL2 band, observed in bulk GaN crystals grown by ammonothermal (AT) method (Section 3.1.3). The YL3 band, exclusive to Fe-contaminated HVPE GaN, is discussed in Section 3.1.4. The V_{Ga} and $V_{Ga}O_N$ defects are not associated with any observed PL bands in GaN (Section 3.1.5).

3.1.2. C_N-Related YL1 Band

The YL1 band, attributed to the C_N acceptor, exhibits distinctive spectral features [41]. At low temperatures (T < 40 K), it has a maximum at 2.17 ± 0.05 eV, with a slightly asymmetric shape, and a FWHM of about 0.43 eV when well resolved (Figure 3a). In high-quality samples with minimal spectral overlap from other PL bands, a sharp ZPL can be resolved at 2.57 eV. At these low temperatures, the YL1 band arises from DAP recombination, specifically electron transitions from shallow donors to the $-/0$ level of C_N, located at 0.916 ± 0.003 eV above the VBM [40].

At higher temperatures (T > 50 K), electrons are thermally excited from shallow donors to the conduction band, and e-A transitions contribute to the YL1 band. The C_N defect also exhibits a 0/+ transition level at 0.33 eV above the VBM, which is responsible for the BL_C band (Section 4.1.1).

The YL1 band can be excited with photons below the bandgap, down to ~2.7 eV. Early PL excitation (PLE) studies modeled the PLE band of YL1 with a Gaussian shape, estimating a characteristic photoabsorption energy $\hbar\omega_{abs}$ between 3.19 and 3.32 eV [86,93]. However, for transitions from a defect to the conduction band, the excitation band is asymmetric due to the continuum of conduction band states [94], yielding a corrected value of $\hbar\omega_{abs}$ = 3.00 ± 0.05 eV [66].

From combined PL and PLE analyses, Ogino and Aoki predicted the ZPL of the YL1 band at 2.64 ± 0.05 eV [86]. More recent studies have directly observed the ZPL at 2.57 eV (at T < 40 K) [40]. The ZPL blue-shifts with increasing excitation intensity, consistent with the DAP recombination mechanism. At higher temperatures, an e-A-related ZPL emerges at 2.59 eV. In some undoped GaN samples (presumably with a low concentration of shallow donors), the e-A-related ZPL dominates already at T = 18 K [41]. Subtracting a smooth shape of the YL1 band reveals phonon replicas, including the longitudinal optical (LO) phonon mode at 91.5 ± 0.5 meV and a pseudo-local phonon mode at 39.5 ± 0.5 meV (Figure 4).

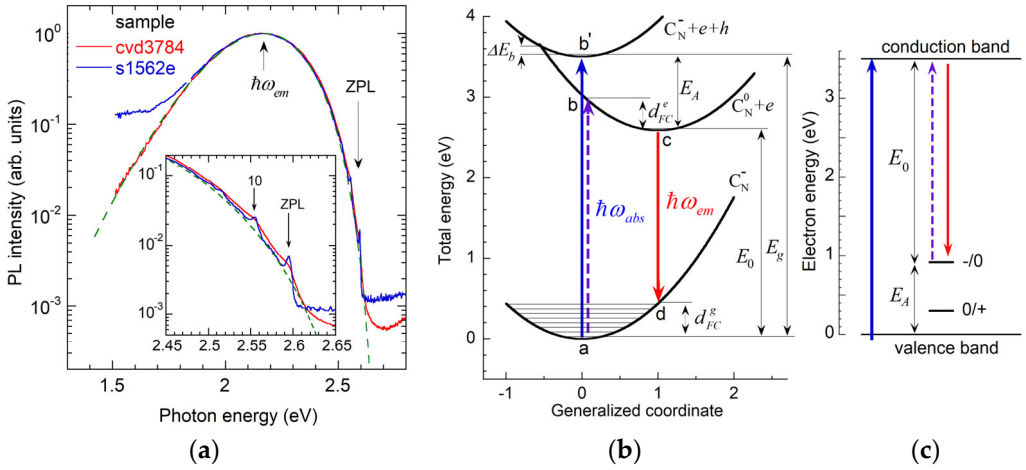

Figure 3. The YL1 band in GaN. (**a**) Normalized PL spectra measured at T = 18 K for two n-type GaN samples grown by MOCVD. The dashed line is calculated using Equation (6) with parameters from Table 2. The inset shows the region near the ZPL. (**b**) Configurational coordinate diagram. (**c**) Band diagram. Excitation and PL transitions are shown with blue and red arrows, respectively. Reproduced with permission from [41].

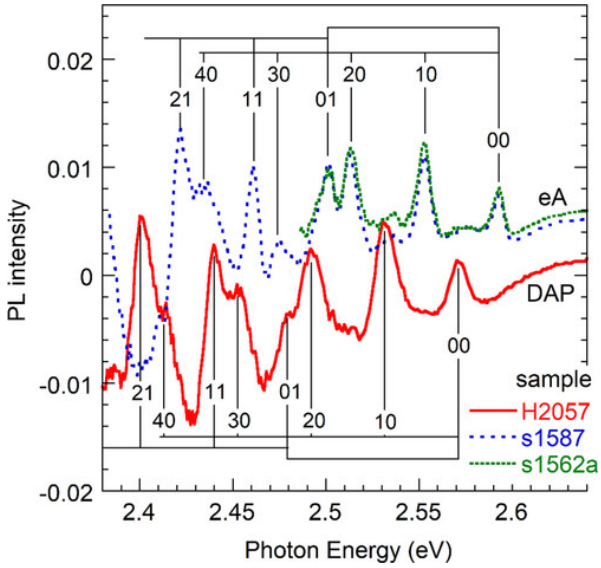

Figure 4. Difference spectra between the experimental normalized PL and simulated with Equation (6) PL band shape for HVPE GaN (sample H2057) and two MOCVD GaN samples (s1587 and s1562a) at T = 18 K. Curves for MOCVD samples are offset by 0.005 for clarity. ZPL and its phonon replicas are labeled as mn, where m and n denote the number of emitted pseudo-local phonons (with energy 39.6 meV) and LO phonons (91.5 meV), respectively. Reproduced with permission from [41].

In TRPL experiments, the YL1 band in nondegenerate n-type GaN samples exhibits nonexponential decay at T < 50 K, consistent with DAP recombination dynamics, gradually transitioning to exponential decay at higher temperatures due to the increasing contribution of e-A recombination [78]. In degenerate n-type GaN samples, e-A transitions dominate at all temperatures. The effective PL lifetime τ_0, is inversely proportional to the free electron concentration n (Figure 5), yielding an electron-capture coefficient $C_n = (1.1 \pm 0.2) \times 10^{-13}$ cm^{3}s^{-1} for the YL1 band [41,65]. Knowing this parameter, the concentration of free electrons can be found in GaN samples from TRPL measurements [65].

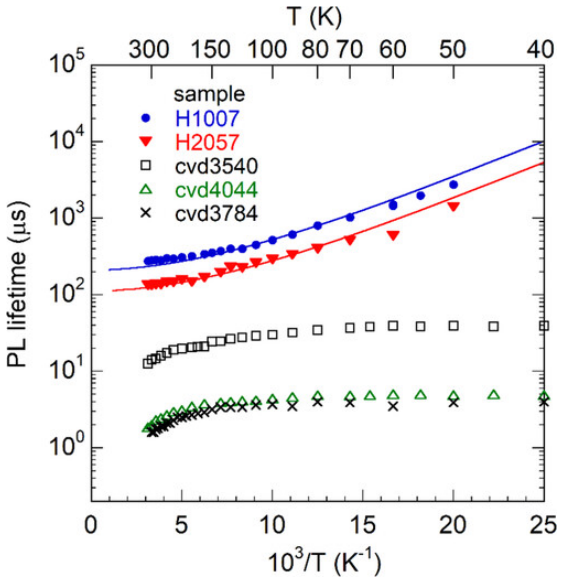

Figure 5. Temperature dependence of PL lifetime for the YL1 band in GaN samples with the following concentrations of free electrons at room temperature, n (cm^{-3}): 5×10^{16} (H1007), 7×10^{16} (H2057), 4×10^{17} (cvd3540), 2×10^{18} (cvd4044 and cvd3784). Reproduced with permission from [41].

Thermal quenching of the YL1 band occurs well above room temperature. In conductive n-type GaN, its temperature dependence follows Equation (2) with $E_A \approx 0.9$ eV. The critical temperature T_0, at which the PL quenching begins, is $T_0 = E_A(k\ln C)^{-1}$. From the PL quenching, the temperature-independent hole-capture coefficient C_p is determined as $(3.5 \pm 1.5) \times 10^{-7}$ cm^3s^{-1} (assuming $g = 2$ and $m_p = 0.8\ m_0$). The YL1 band broadens with increasing temperature in agreement with Equation (7), and analysis of the temperature dependence of the band width $W(T)$ yields an effective phonon energy $\hbar\Omega_e = 56 \pm 2$ meV [41]. In SI GaN samples, the YL1 quenching follows the TAQ mechanism [52]. The T_0 shifts with excitation intensity, and $E_A \approx 0.9$ eV can be found from Equation (3) [95].

Similar to PL from other acceptors in GaN, the YL1 band exhibits excitation intensity-dependent shifts. In conductive n-type GaN samples, the YL1 band blueshifts by up to 10 meV with increasing P_{exc} over several orders of magnitude at low temperatures, consistent with the DAP recombination model. In SI or heavily Si-doped GaN samples, the YL1 band may blue-shift by as much as 0.1 eV with increasing P_{exc} due to screening of potential fluctuations by photogenerated charge carriers [54]. A redshift in the YL1 band with a time delay after a laser pulse is also observed in TRPL measurements. The YL1 band saturates with increasing P_{exc} in agreement with Equation (4), enabling estimation of C_N defect concentrations [41,80].

Hybrid functional DFT calculations accurately reproduce key properties of the C_N-related YL1 band [24,96–99]. Theoretical predictions include a ZPL energy $E_0 = 2.48$–2.71 eV, a band maximum $\hbar\omega_{max} = 2.01$–2.18 eV, the $-/0$ level at $E_A = 0.78$–1.1 eV, and characteristic resonant excitation energy $\hbar\omega_{abs} = 2.91$–3.04 eV, in close agreement with experimental values ($E_0 = 2.59$ eV, $\hbar\omega_{\max} = 2.19$ eV for e-A transitions, $E_A = 0.916$ eV, and $\hbar\omega_{abs} = 3.0$ eV [40,41]). Calculations predict a classical barrier for hole capture by C_N ($\Delta E_b = 0.49$–0.73 eV with the calculated $-/0$ level at 1.02 eV [100,101]), which is expected to cause a pronounced temperature dependence of C_p. However, experimentally, the YL1 intensity (which is proportional to C_p) remains nearly constant from very low temperatures up to T_0, suggesting a negligible capture barrier (Figure 3b). Other parameters of the configuration coordinate model extracted from experimental data are also close to theoretical predictions. In particular, the experimental Huang–Rhys factor $S_e = 8 \pm 1$ [41] agrees with the calculated $S_e = 10.3$ [102].

Attempts to assign defects by formally matching theoretical predictions and experimental data are common [96,103], and they often lead to errors [104]. A recent example includes the incorrect attribution of the YL1 band to the C_NO_N complex [105]. First-principles calculations in that study predicted PL band maxima for the C_N and C_NO_N defects at 1.88 eV and 2.25 eV, respectively. The YL1 band with a maximum at ~2.2 eV was accordingly attributed to the C_NO_N complex [105]. This attribution gained some theoretical support [106], but was subsequently challenged [98,103,107]. According to current advanced calculations, the concentration of isolated C_N defects should be orders of magnitude higher than that of the C_NSi_{Ga} and C_NO_N complexes, and PL bands from these complexes are predicted at higher photon energies (at 2.23–2.71 eV) [98,103,106]. Finally, experimental evidence consistently supports C_N as the sole contributor to the YL1 band, with no signatures of C_NO_N or C_NSi_{Ga} in PL spectra [25,41], likely due to their low concentrations and/or low hole-capture efficiencies (Section 4.1.4).

3.1.3. YL2 Band in Ammonothermal GaN

Unlike GaN layers deposited on sapphire substrates by MOCVD, MBE, or HVPE techniques, bulk GaN crystals grown by the AT method contain high concentrations of V_{Ga} or V_{Ga}-related complexes [108–111]. These samples are typically degenerate *n*-type ($n = 10^{18}$–10^{19} cm^{-3}), contain high concentrations of O and H (10^{18}–10^{19} cm^{-3}), as well as significant levels of Si, C, Mg, and Zn (~10^{17} cm^{-3}) [111]. Their PL spectra contain Mg-related UVL, Zn-related BL1, and a new yellow band at ~2.3 eV, designated YL2 (Figure 6).

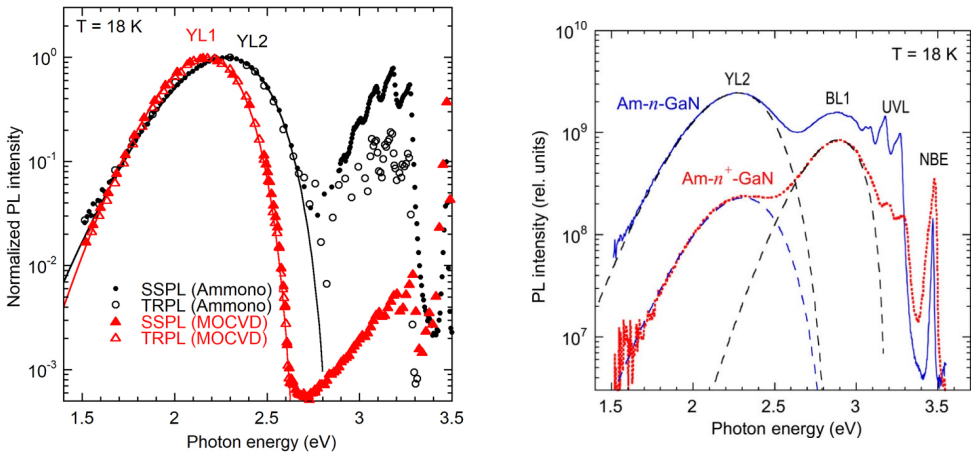

Figure 6. PL spectra from ammonothermal GaN samples at T = 18 K. (**a**) Comparison of the YL2 band in AT GaN (Ammono) with the YL1 band in MOCVD GaN. (b) PL spectra from two AT GaN samples. Solid lines in (**a**) and dashed lines in (**b**) are calculated using Equation (6) with parameters from Table 2. Reprinted with permission from [39,42].

The YL2 band, distinct from the C_N-related YL1 (Figure 6a), shifts from 2.28 to 2.34 eV as the excitation intensity in SSPL increases from 10^{-4} to ~100 Wcm^{-2}, and exhibits a red shift of ~0.1 eV over time delays in TRPL measurements. These shifts may indicate possible contributions from multiple defects [42]. The position of the YL2 maximum and the defect ionization energy, estimated as ~0.7 eV from the band shape, agree with predictions from first-principles calculations for deep donors such as $V_{Ga}3H_i$ and $V_{Ga}O_N2H_i$ [39,42]. Acceptor complexes (e.g., $V_{Ga}2H_i$ and $V_{Ga}O_NH_i$) are predicted to have $-/0$ levels at 1.4–1.6 eV above the VBM [29,39] and, thus, are not expected to contribute to visible PL. FTIR absorption measurements on degenerate *n*-type AT GaN samples revealed high concentrations (more than 10^{18} cm^{-3}) of complexes containing V_{Ga} and up to three H atoms, in agreement with the estimates from PAS [108,110].

3.1.4. YL3 Band in HVPE GaN

The YL3 band, peaking at 2.07 eV, with a ZPL at 2.36 eV at $T \approx 18$ K, is observed in undoped HVPE GaN. It is associated with the RY3 defect, which also gives rise to the RL3 band (Section 3.2.3) [34,38,44]. The RY3 defect is an acceptor, with two deep states (A_1 at 0.5–1.0 eV below the CBM, and A_2 at 1.13 eV above the VBM) and a shallow state (A_3 at $\sim$ 0.2 eV above the VBM) [38]. Photogenerated holes are quickly captured by the excited state A_3. The RL3 component of the broad RY3 band arises from radiative transitions of the bound hole from A_3 to A_1 with a characteristic time of about 10 ns. Transitions of the bound hole from A_3 to A_2 are nonradiative, over a 0.06–0.07 eV barrier. The YL3 component of the RY3 band arises from DAP transitions (shallow donors to A_2) at $T < 40$ K or e-A transitions to A_2 at $T > 50$ K with $\tau_0 \approx 100$ μs [38,44]. The very different lifetimes of RL3 and YL3 allow us to resolve the YL3 component (Figure 7). The fine structure of the YL3 band includes the DAP-related ZPL at 2.36 eV and the e-A-related ZPL at 2.38 eV, both followed by phonon replicas from three sets of phonons: the LO mode with $\hbar\Omega = 91$ meV and two pseudo-local modes (19 and 36 meV) [43,44].

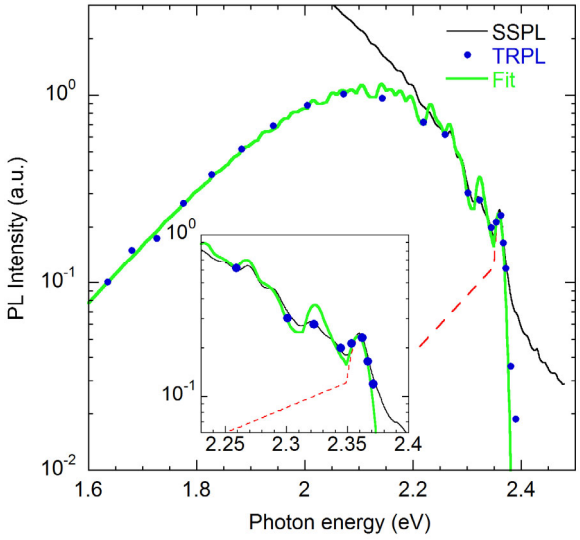

Figure 7. PL spectra of the YL3 band at $T = 18$ K. Solid circles represent the normalized TRPL spectrum (at time delay of 100 μs), and the thin black solid line shows the SSPL spectrum at $P_{exc} = 0.007$ Wcm^{-2}. The thick light green line is calculated as a superposition of PL involving three phonon modes. Reprinted from [44].

The RY3 defect is tentatively associated with Fe_{Ga} or Fe_{Ga}-containing complexes, as the RY3 band correlates with the Fe_{Ga}-related 1.31 eV PL line. Interestingly, the RY3 band is absent in Fe-doped SI GaN, where the Fermi level is expected to lie near the $-/0$ level of Fe_{Ga}, ~0.6 eV below the conduction band minimum (CBM) [112–114]. The absence of RY3 in SI GaN is presumed to arise from competition for photogenerated electrons. In such samples, electrons are preferentially captured by nonradiative donors, suppressing radiative recombination. In contrast, in conductive *n*-type GaN, PL intensity is governed by the capture of photogenerated holes, and the hole capture by the excited state A_3 is very efficient.

3.1.5. Exclusion of V_{Ga} and $V_{Ga}O_N$ as Sources of the YL Band

The V_{Ga} and $V_{Ga}O_N$ defects, both deep, multi-charged acceptors, are unlikely contributors to the YL band in *n*-type GaN, where the Fermi level lies near the CBM. Under such conditions, only the $3-/2-$ level for V_{Ga} and the $2-/-$ level for $V_{Ga}O_N$ are expected to be active. While early DFT calculations placed these levels near 1 eV above the VBM [22,115],

more accurate hybrid functional DFT calculations have since revised their positions to significantly higher energies: 1.75–3.13 eV above the VBM for V_{Ga} [29–32,116,117] and 1.55–2.17 eV above the VBM for $V_{Ga}O_N$ [29,39]. Electron transitions from the CBM to these levels are most likely nonradiative [30,39], precluding PL contributions above 1.5 eV.

Lyons et al. [29] suggested that hole capture at the V_{Ga} $3-/2-$ level is radiative and can cause a PL band similar to the YL band. However, such radiative capture would be much slower than competing nonradiative hole capture by more efficient acceptors, such as C_N. As a result, any emission from this mechanism would be masked by stronger PL bands. Similarly, transitions via the $2-/-$ level of the $V_{Ga}O_N$ complex are nonradiative or weakly radiative with a PL signal in the infrared region [39]. Alkauskas et al. [118] proposed that hole capture by this level in *n*-type GaN occurs nonradiatively, via an excited state located at 1.15 eV above the VBM. Note that nonradiative capture coefficients depend strongly (approximately exponentially) on the energy of the transition [119].

Wang et al. [117] proposed that the yellow band originates from electron transitions from the CBM to the 0/+ levels of V_{Ga} or $V_{Ga}O_N$. However, this mechanism is not viable in *n*-type GaN, where these defects reside in their fully negative charge states ($3-$ for V_{Ga} and $2-$ for $V_{Ga}O_N$). To date, no reliable experimental evidence supports predictions of PL from either V_{Ga} or $V_{Ga}O_N$. In high-quality HVPE-grown GaN samples, where PL bands are reliably recognized, no PL features could be attributed to V_{Ga}, while the concentration of V_{Ga} (from PAS measurements) varied between 10^{16} and 10^{18} cm^{-3} [66].

Historical observations of the YL band in undoped GaN produced by various growth methods can be attributed to trace contamination with carbon [5,35,41]. In particular, Saarinen et al. [28] reported a correlation between the YL band intensity and the concentration of the V_{Ga}-related defects in GaN. However, the PL in that work was collected from a region near the GaN/sapphire interface, where the concentration of defects is very high. Subsequent studies [92,120,121] have failed to reproduce this correlation and, in some cases, have reported an anticorrelation between the YL intensity and the V_{Ga} concentration, further weakening the case for the V_{Ga}-related YL.

3.2. Red Luminescence Bands in Undoped GaN (RL1, RL2, RL3, RL4)

Red luminescence (RL) bands are frequently observed in undoped GaN, particularly in samples grown by HVPE. Four distinct RL bands—designated RL1 through RL4—have been recognized, each characterized by unique spectral features and recombination dynamics. The RL1 and RL3 bands are prominent in HVPE GaN, distinguished mainly in TRPL experiments due to their contrasting decay behaviors. The RL1 band exhibits nonexponential decay at $T < 50$ K, and exponential slow decay (with lifetimes in the millisecond range) at higher temperatures. The RL3 decays exponentially with $\tau_0 \approx 10$ ns. The RL2 appears at low temperatures in SI GaN grown by various techniques. It exhibits an exponential decay with $\tau_0 > 1$ μs at $T < 100$ K. The RL4 band emerges in AT GaN only after thermal annealing. Below, each RL band is discussed in more detail.

3.2.1. RL1 Band in HVPE GaN

The RL1 band, peaking at ~1.75 eV, is the dominant defect-related PL feature in undoped GaN grown by HVPE, particularly at low P_{exc}, when contributions from YL1 (Section 3.1.2) and GL1 (Section 3.3.1) are minimal (Figure 8a). Its behavior is consistent with a deep acceptor, with an ionization energy $E_A \approx 1.0$–1.2 eV. In conductive *n*-type GaN, the RL1 band is highly efficient at low P_{exc}, with SSPL intensity nearly constant up to 500 K. At low temperatures ($T < 50$ K), non-exponential decay is consistent with DAP recombination involving shallow donors. Above 50 K, e-A transitions dominate, yielding a

long effective lifetime (in the millisecond range), inversely proportional to the free electron concentration. Due to its long lifetime, the RL1 band saturates at relatively low P_{exc}.

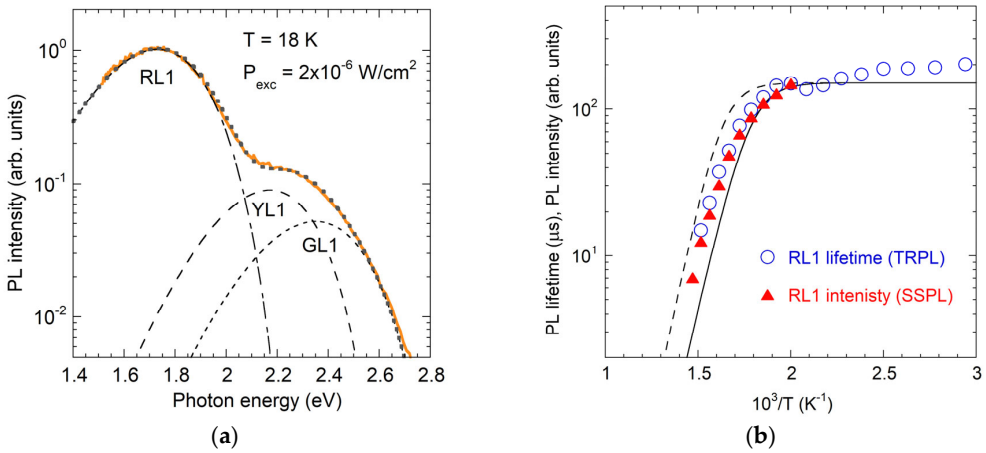

Figure 8. The RL1 band in HVPE GaN. (**a**) Low-temperature PL spectrum at low P_{exc}. The shapes of the RL1, YL1, and GL1 bands, shown with dashed lines, are calculated using Equation (6) with parameters from Table 2. The thick dotted line shows the sum of these three components. (**b**) Temperature dependence of the RL1 lifetime (open circles) and its SSPL intensity (filled triangles). The lines are calculated using Equation (2) with E_A = 1.0 eV (solid line), E_A = 1.1 eV (dashed line), and the following other parameters (for both lines): $C_p = 3 \times 10^{-7}$ cm^{3}s^{-1}, τ_0 = 150 μs, $(1 - \eta_0) = 1$.

Thermal quenching of RL1 begins at $T > 500$ K (Figure 8b), consistent with E_A = 1.0–1.2 eV. TRPL analysis yields $C_n \approx 4.5 \times 10^{-14}$ cm^{3}s^{-1} from Equation (1) [65]. The hole-capture coefficient, $C_p \approx 3 \times 10^{-7}$ cm^{3}s^{-1}, is derived from comparisons of PL intensities and defect concentrations using Equations (4) and (5) [75,83]. These coefficients align with those of other acceptors in GaN (Figure 9). ODMR studies of HVPE-grown freestanding GaN templates revealed an isotropic g = 2.019 factor for the RL1-related defect [122]. The RL1 origin remains uncertain, but it is tentatively linked to Cl or Cl-containing defects, as it is exclusive to Cl-contaminated HVPE GaN and absent in MBE- or MOCVD-grown GaN [66].

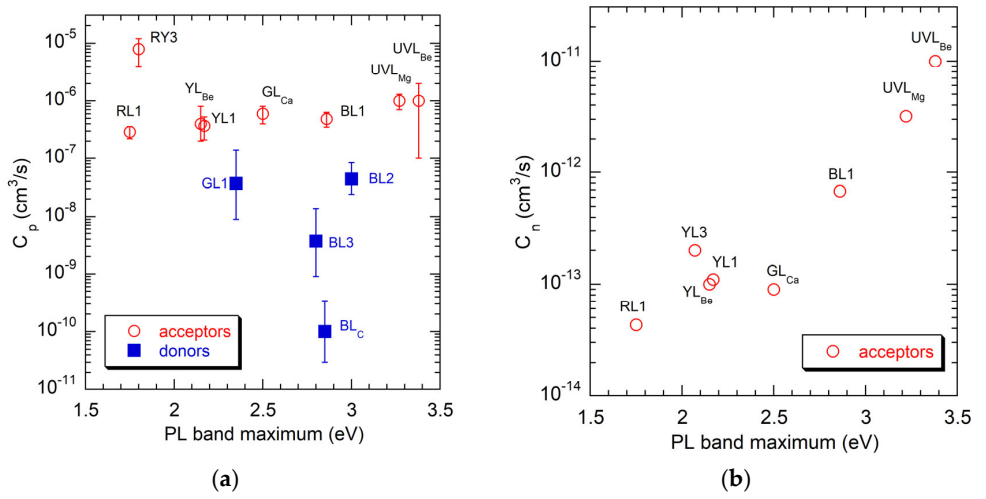

Figure 9. Parameters of defect-related PL bands in GaN. (**a**) Hole-capture coefficients. (**b**) Electron-capture coefficients. Reprinted from [34].

3.2.2. V_N-Related RL2 Band

The RL2 band, peaking at ~1.74 eV, is observed alongside the GL2 band (Section 3.3.2) in SI GaN samples, particularly those grown under extremely Ga-rich conditions (Figure 10a)

or after surface mechanical polishing [37,123]. The RL2 emission is characterized by exponential decay, even at very low temperatures (T < 20 K), suggesting that it originates from an internal transition within a deep donor, from an excited state to the ground state. Figure 10a shows the RL2 band, with a small contribution of GL2 at ~2.33 eV. A substantial body of evidence, accumulated since 2005, supports the assignment of the GL2 band to isolated V_N defects (Section 3.3.2). The RL2 band is attributed to a family of red-emitting centers associated with AV_N complexes, where A is a group-II metal substituting for Ga.

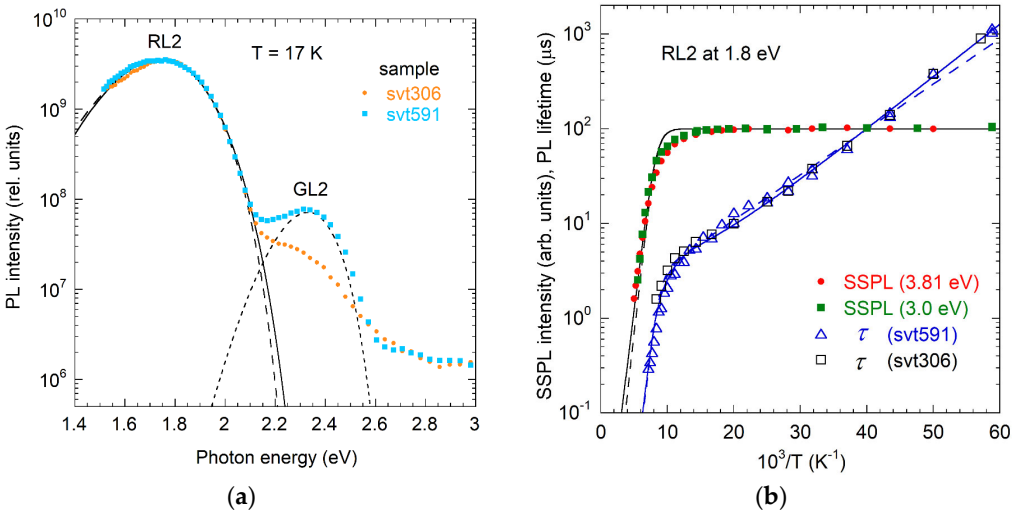

Figure 10. RL2 band in MBE GaN. (**a**) SSPL spectra at T = 17 K. The spectral components are fitted using Equation (6) with parameters from Table 2. (**b**) Temperature dependence of SSPL intensity and PL lifetime for the RL2 band. Lines are the fits with equations obtained with a phenomenological model described in [37]. Reprinted with permission from [37].

In undoped GaN grown by MBE under Ga-rich conditions [16], the RL2 lifetime decreases from 1050 to 3 μs as the temperature rises from 17 to 100 K (Figure 10b) [37]. While the SSPL intensity remains constant below 100 K, it quenches at higher temperatures with an activation energy of 0.1–0.15 eV (Figure 10b). The quenching was initially explained by the Seitz–Mott mechanism, involving a 0.12 eV barrier in the configuration coordinate diagram [16]. However, more recent interpretations favor the Schön–Klasens mechanism, in which quenching is attributed to the thermal emission of electrons from the excited state to the conduction band. This behavior is typical when competition for electrons limits the PL efficiency [36,37]. Although there is a good understanding of the RL2-type bands caused by the AV_N complexes with A = Be_{Ga}, Mg_{Ga}, and Ca_{Ga} (Section 4.2.4, Section 4.3.5, and Section 4.6.3), the specific acceptors involved in the AV_N complexes responsible for the RL2 band in MBE-grown undoped GaN [124,125] remain unidentified. A distinguishing feature of the RL2 band in these samples is the temperature-dependent lifetime behavior, which reveals an activation energy of ~10 meV between 17 and 100 K (Figure 10b). A phenomenological model has been proposed in which two excited states are located near the CBM, while the ground state lies ~1 eV above the VBM [37]. The observed $\tau(T)$ dependence at T < 100 K is attributed to thermal activation of a radiative excited state that lies about 10 meV above a nonradiative (or weakly radiative) excited state.

3.2.3. RL3 Band in HVPE GaN

The RL3 band, peaking at 1.77 eV, is observed in HVPE-grown GaN and, together with the YL3 band, forms the RY3 band (Figure 11). The RL3 component of RY3 exhibits fast, exponential decay with a characteristic lifetime $\tau_0 \approx 10$ ns at T = 2–200 K [38,126,127], in stark contrast to the YL3 component, which displays much slower decay ($\tau_0 \approx 100$ μs).

The consistent intensity ratio between RL3 and YL3 across a wide range of HVPE samples strongly supports their origin from the same defect, referred to as RY3. The RL3 is distinguished by a less steep high-energy spectral side. Early reports misassigned the ZPL at 2.36 eV and associated phonon structure to RL3 [43], but this was later corrected: these features belong to the YL3 band [38] (Section 3.1.4).

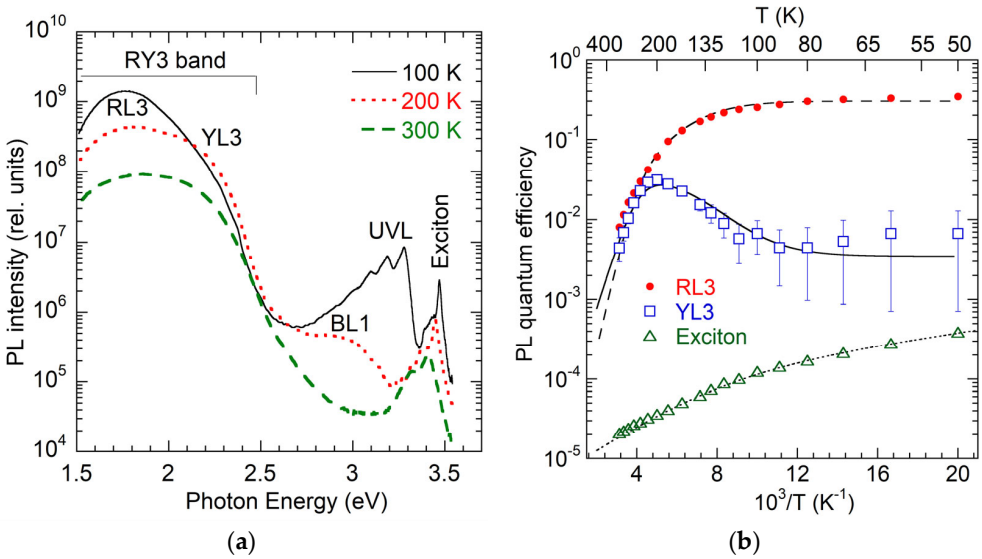

Figure 11. RY3 defect in HVPE GaN. (**a**) Evolution of the PL spectrum with temperature. (**b**) Temperature dependence of the PL quantum efficiency for the RL3 and YL3 components of the RY3 band. Reprinted with permission from [38].

In early works, the RL3 band was attributed to DAP transitions involving C and O impurities that were abundant in HVPE GaN samples (~10^{19} cm^{-3} each) [128,129]. However, the fast and purely exponential decay kinetics of the RL3 emission rule out DAP recombination, indicating an internal transition. Moreover, the RL3 band is strong even in samples with very low concentrations of C and O [38], sometimes below the SIMS detection limit of 5×10^{15} cm^{-3} [127], further invalidating the above attribution. The RY3 defect is tentatively assigned to Fe-related defects, yet the assignment of the RL3 and YL3 bands specifically to isolated Fe_{Ga} acceptors seems ambiguous, as will be discussed later.

A detailed model of the RY3 defect [38] proposes three acceptor levels (Figure 12): a ground state A_1 at 0.7 ± 0.3 eV below the CBM, another deep state A_2 at 1.13 eV above the VBM, and a shallow excited state A_3 at ~0.2 eV above the VBM. In this model, holes captured at A_3 can follow two competing paths: radiative recombination with electrons at A_1, producing the RL3 ($\tau_0 \approx 10$ ns), or nonradiative relaxation to A_2 over a 0.06 eV barrier, followed by DAP or e-A recombination, resulting in the YL3. This model successfully explains the observed temperature- and excitation-dependent interplay between RL3 and YL3 components [38]. Notably, Uehara et al. [127] demonstrated that the RL3 band can be excited below the bandgap by photons with energy of 3.42 eV (but not by 3.06 eV).

The RY3 defect resembles the Cu_{Zn} acceptor in ZnO, which produces the green luminescence (GL_{Cu}) band, peaking at 2.45 eV, with a ZPL at 2.859 eV [130–133]. The GL_{Cu} band originates from internal transitions of holes between an excited state (0.4 eV above the VBM) and the ground state (~0.2 eV below the CBM). Like RL3, the GL_{Cu} band exhibits exponential decay at cryogenic temperatures (even at 1.6 K), with a PL lifetime of 440 ns [130]. In conductive *n*-type ZnO, where the Fermi level lies above the ground $-/0$ level of the Cu_{Zn}, the GL_{Cu} band is observed after photogenerated holes are captured by the excited state. However, resonant excitation of the GL_{Cu} band below the bandgap is possible only in high-resistivity ZnO, where the Fermi level is below the $-/0$ level of the

Cu_{Zn} [132–134]. In contrast, the RL3 band in GaN can be excited below the bandgap (at 3.42 eV) in moderately conductive ($n \approx 10^{16}$–10^{17} cm^{-3}) HVPE GaN samples [127].

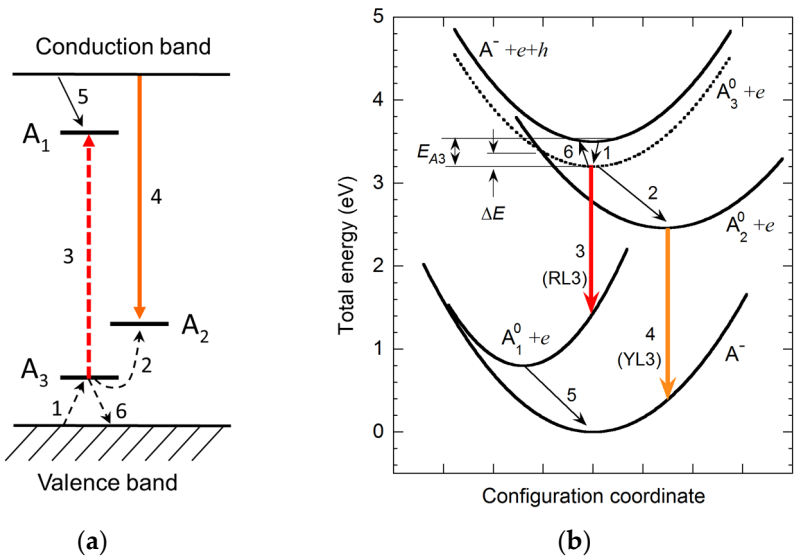

(**a**) (**b**)

Figure 12. Electron and hole transitions associated with the RY3 defect in GaN. (**a**) Band diagram. (**b**) Configuration coordinate diagram. A^- is the ground state of the RY3 center in *n*-type GaN (negatively charged acceptor); $A_1{}^0$ is the ground state of the neutral acceptor with a strongly localized hole; $A_2{}^0$ is the deep excited state with a localized hole; $A_3{}^0$ is the shallow excited state with a weakly localized hole. Transitions 3 and 4 are responsible for the RL3 and YL3 components of the RY3 band. Reprinted with permission from [38].

By analogy, the RY3 center in GaN is likely associated with a transition metal impurity. Indeed, Fe concentration appears to correlate with the RY3 band intensity. In particular, the concentration of Fe in a sample with a strong RY3 band was elevated (2.5×10^{15} cm^{-3}), matching the concentration of the RY3 defect estimated from PL measurements [38]. A rough correlation between the intensities of the RL3 band and the Fe-related 1.31 eV line was also noted in a set of HVPE-grown undoped GaN samples. Furthermore, the ground level of the RY3 center (0.7 ± 0.3 eV below the CBM) is close to the reported position of the ground level of Fe_{Ga} acceptors (at ~0.63 eV [135]). The RY3 band is not observed in Fe-doped SI GaN samples, and this can be explained by conditions where the PL efficiency is dictated by the fast capture of electrons, not holes. However, in some works, the RY3 was not observed in the low-temperature PL spectra, whereas samples were *n*-type and contained substantial concentrations of Fe [136,137]. This may indicate that the RY3 is a complex defect, not just an isolated Fe_{Ga}.

3.2.4. RL4 Band in Ammonothermal GaN

The RL4 band, peaking at 1.6–1.7 eV, emerges in PL spectra from AT GaN after thermal annealing (Figure 13a), and its IQE approaches unity at $T_{ann} \approx 1000$ °C [39]. As-grown AT GaN samples contain high concentrations of V_{Ga}, O, H, and related complexes, as confirmed by FTIR studies [110,111,138,139]. First-principles calculations suggest that complexes such as $V_{Ga}3H_i$ and $V_{Ga}O_N2H_i$ contribute to yellow PL, whereas $V_{Ga}2O_NH_i$ and $V_{Ga}3O_N$ can produce red PL (Figure 13b) [29,39]. The RL4 band has been tentatively attributed to the $V_{Ga}3O_N$ complex, which may form via the annealing-induced dissociation of nonradiative $V_{Ga}3O_NH_i$ complexes [39]. The emission energy of the RL4 band is sample-dependent. It has a maximum at 1.7 eV in n^+-GaN samples with high V_{Ga}, O, and H concentrations and at 1.6 eV in *n*-GaN samples with lower concentrations, suggesting possible compositional

variations [39]. Spectral deconvolution also reveals a distinct orange PL band (OL3) with a maximum at 2.09 eV in annealed AT GaN samples (Figure 13a) [39].

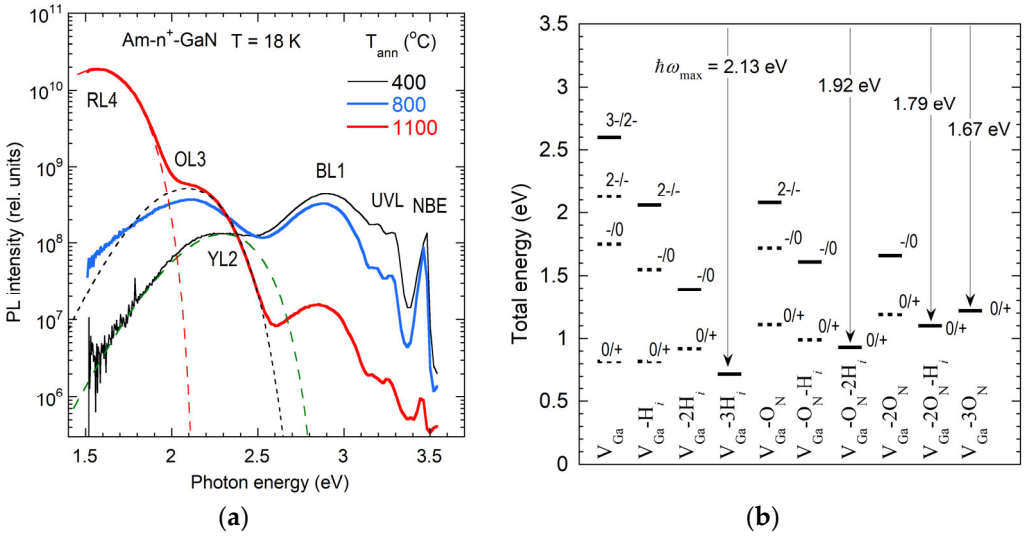

(**a**) (**b**)

Figure 13. PL bands in AT GaN. (**a**) Low-temperature PL spectra from AT n^+-GaN annealed in N_2 under atmospheric pressure at selected T_{ann}. Dashed lines are calculated using Equation (6) with parameters from Table 2. (**b**) Calculated charge transition levels of defect complexes containing V_{Ga}, H_i, and O_N. Solid horizontal bars represent levels that participate in electron-hole recombination and possible PL in conductive *n*-type GaN. Dashed bars correspond to levels inactive under these conditions and therefore unobservable in PL. Vertical arrows show candidate radiative transitions, with indicated photon energies corresponding to $\hbar\omega_{max}$ (not the ZPL). Reprinted with permission from [39].

All candidate defects proposed to contribute to the V_{Ga}-related PL in as-grown and annealed AT GaN (shown with arrows in Figure 13b) are deep donors. However, the observed high intensities and nonexponential decays of the YL2, OL3, and RL4 bands distinguish them from typical deep-donor-related PL bands in GaN, which are weak in conductive *n*-type GaN and exhibit exponential decays due to internal transitions (Table 1). The nonexponential decay may indicate that the related defects are, in fact, acceptors. Alternatively, potential fluctuations due to the nonuniform distribution of charged defects or overlapping PL bands may be the reason for the nonexponential decays. High PL efficiency (close to unity for the RL4 band) is another puzzle. Known deep donors in GaN generally have low hole-capture coefficients and produce inefficient PL in conductive *n*-type samples. However, to explain the exceptionally high IQE of the RL4 band in degenerate *n*-type AT GaN, the hole-capture coefficient for the related defect was estimated as ~10^{-6} cm^3s^{-1} (if its concentration is close to 10^{20} cm^{-3}) or even larger (if the concentration is lower) [39]. Note that the defect assignments in [39] were based on hybrid functional DFT predictions, which may lack precision, necessitating further experimental validation.

3.3. Green Luminescence Bands (GL1, GL2, GL_{Ca})

Several distinct green luminescence (GL) bands are observed in undoped GaN, each characterized by unique spectral and temporal properties. The GL1 band, peaking at 2.35 eV, is prominent in HVPE-grown GaN. A spectrally similar but narrower GL2 band, also near 2.35 eV, appears exclusively in SI GaN grown by various techniques. These bands are readily differentiated by their distinct shapes and behaviors in SSPL and TRPL experiments. Additionally, a Ca-related GL_{Ca} band appears in MBE-grown GaN contaminated with Ca. Each band is discussed in detail below.

3.3.1. Unidentified GL1 Band in HVPE GaN

The GL1 band, peaking at 2.35 eV, is a prominent defect-related PL feature in undoped HVPE GaN (named GL band in [16]). Its intensity scales super-linearly (nearly quadratically) with excitation intensity, suggesting a secondary PL process requiring sequential capture of two holes by a deep defect [140]. TRPL reveals exponential decay kinetics, consistent with internal transitions. Figure 14 shows PL spectra from an HVPE GaN sample at T = 100 K. At low excitation intensity (P_{exc} = 2 × 10^{-6} Wcm^{-2}), the RL1 band dominates, with a weak YL1 band at higher photon energy, while the GL1 band is not resolved. As P_{exc} increases, RL1 and YL1 saturate due to their long lifetimes, while GL1 intensity rises super-linearly (PL intensities are divided by P_{exc} in Figure 14a). The NBE luminescence (at 3.47 eV, with LO phonon replicas) also shows super-linear increase, typical of SI GaN. TRPL spectra resolve these PL bands at different time delays (Figure 14b). Analysis of the GL1 band shape and temperature-dependent intensity yields the following parameters: $E_A \approx 0.50$ eV, $C_p = (3.7 \pm 1.3) \times 10^{-8}$ cm^{3}s^{-1}, and $S_e \approx 10$ [66,83].

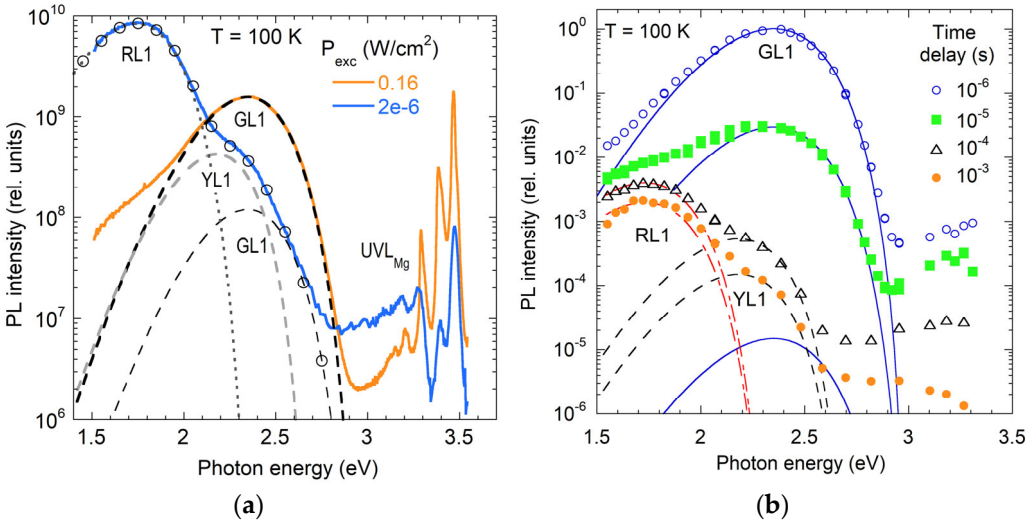

Figure 14. The GL1 band in HVPE GaN (sample AH1177 from Kyma). (**a**) SSPL spectra at two excitation intensities, normalized by P_{exc}. Dashed lines are calculated using Equation (6) with parameters from Table 2. Empty circles show the sum of three calculated components at P_{exc} = 2 × 10^{-6} Wcm^{-2}. (**b**) TRPL spectra at selected time delays. Lines are calculated using Equation (6) with parameters from Table 2.

A unique feature of the GL1 band is a significant increase in its lifetime (by 20–50 times) with increasing temperature from 100 to 300 K [141–144]. A model proposed in [144] explains this behavior (Figure 15a): following above-bandgap excitation, the defect captures two holes and becomes positively charged. The capture of a free electron into an excited state near the CBM (level 1) occurs via the nonradiative Lax mechanism [145] (characteristic time τ_1), followed by a radiative internal transition to level 2 (with the characteristic time $\tau_2 \approx 1$ μs), producing the GL1 band. The PL intensity decays with time t after a laser pulse as [144]:

$$I^{PL}(t) = I^{PL}_{\max}\left[\exp\left(\frac{-t}{\tau_1}\right) - \exp\left(\frac{-t}{\tau_2}\right)\right] \quad (8)$$

At low temperatures, the cascade capture of free electrons by the excited state 1 is very fast ($\tau_1 << \tau_2$), and Equation (8) reduces to $I^{PL}(t) \approx I^{PL}{}_{\max} \exp(-t/\tau_2)$. As temperature rises, τ_1 increases as T^3 (typical of "giant traps" [145]), while τ_2 remains nearly constant, leading to $\tau_1 >> \tau_2$ and $I^{PL}(t) \approx I^{PL}{}_{\max} \exp(-t/\tau_1)$ at high temperatures. Overall, at any temperature, the decay of PL is nearly exponential, where τ is determined by the slower process (Figure 15b).

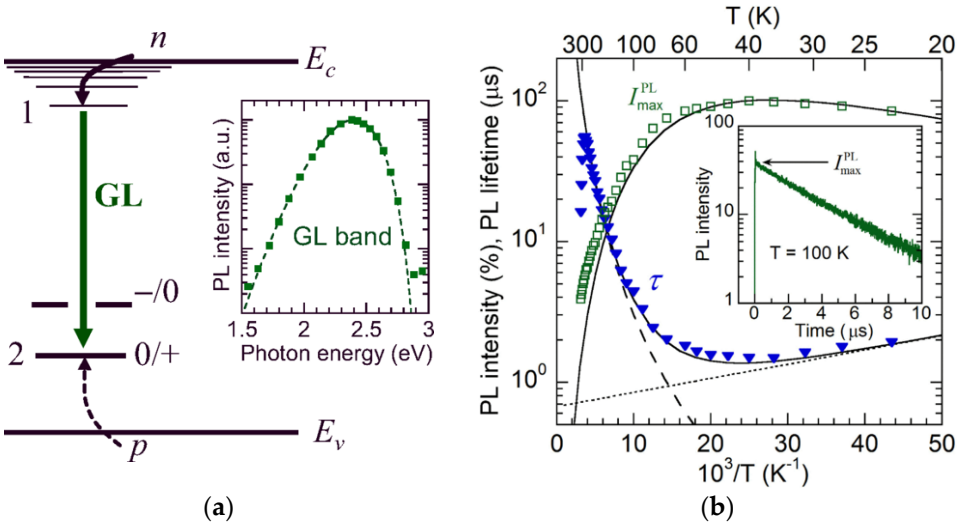

Figure 15. GL1 band in HVPE GaN. (**a**) Schematics of transitions. The defect becomes positively charged after capturing two holes. In the electron-hole recombination process, a free electron is first captured at the excited state (level 1) by the Lax mechanism, a nonradiative process. Then, the internal transition from level 1 to level 2 causes the GL1 band. The PL lifetime in TRPL experiments is dictated by the slower of these two processes. The inset shows the shape of the GL1 band at 30 K (note the log scale). (**b**) The temperature dependence of the PL lifetime (solid triangles) and the peak PL intensity after a laser pulse (empty squares) for the GL1 band. The solid lines are $\tau(T) = \tau_1 + \tau_2$ and $I^{PL}{}_{max}(T)$ calculated using Equation (8). The calculated τ_1 and τ_2 components are shown with the dashed and dotted lines, respectively. The inset shows the decay kinetics at 100 K. Reprinted with permission from [144].

Identifying the defect responsible for GL1 is critical, as it is prominent in high-quality freestanding GaN grown by HVPE, which has low dislocation and point defect densities. ODMR studies of HVPE-grown GaN freestanding templates revealed g factors $g_{\parallel}$ =1.975 and $g_{\perp}$ = 1.969 for the defect responsible for GL1 [122]. Early studies attributed YL and GL1 bands, respectively, to the $2-/-$ and $-/0$ levels of the $V_{Ga}O_N$ complex [16,140,141]. However, hybrid functional DFT calculations later ruled out $V_{Ga}O_N$ as a visible PL source and instead proposed the C_N and C_NO_N defects as responsible for the YL bands [24,98,103,105]. The YL band at 2.1 eV (now called YL3) and the GL1 band were tentatively linked to two charge states of the C_N defect, while the YL band at 2.2 eV (now called YL1) was thought to be caused by the C_NO_N [142,143]. These assignments have since been disproven. Current understanding identifies the $-/0$ and $0/+$ levels of the C_N as responsible for the YL1 (Section 3.1.2) and BL_C (Section 4.1.1) bands, respectively, while the C_NO_N donor does not contribute observable PL (Section 4.1.4). Lack of correlation between GL1 and either YL1 or YL3 further supports the conclusion that they originate from distinct centers.

The GL1 and RL1 arise from unidentified point defects with estimated concentrations of 10^{15}–10^{16} cm^{-3} in high-quality HVPE GaN [142,146]. Defects containing V_{Ga} or V_N are unlikely to be responsible [66] (Section 3.6). While Cl, with typical concentrations of ~10^{16} cm^{-3} in HVPE-grown GaN, appears to correlate with RL1 intensity in some samples, this may be coincidental [38,142]. The super-linear excitation behavior of GL1 suggests it is a secondary PL process, becoming prominent only after a primary PL band (denoted X) saturates. The X and GL1 may be caused by transitions via the $-/0$ and $0/+$ levels of a deep defect. In *n*-type GaN, where PL efficiency is governed by hole capture, the IQE of X at low P_{exc} should exceed that of GL1 at high P_{exc}, similar to the behavior observed for the C_N defect [25]. While RL1 is a candidate for the X, no consistent correlation has been observed between RL1 and GL1, leaving the identities of both bands unresolved.

3.3.2. V_N-Related GL2 Band

The GL2 band, peaking at ~2.33 eV, with a FWHM of 0.23–0.25 eV (Figure 16), is attributed to internal transitions from an excited state to the +/2+ level of the isolated V_N [47]. This band is usually observed in high-resistivity or SI GaN, particularly in samples grown under Ga-rich conditions or doped/implanted with acceptor impurities such as Mg or Be [16,47,147–151]. A distinguishing feature of the GL2 band is its exponential decay after pulsed excitation, with a lifetime of ~300 μs at T < 100 K. Its relatively narrow FWHM is consistent with the configuration-coordinate model (Figure 17a), and the spectral shape can be quantitatively described with Equation (6) [35,37,47,152].

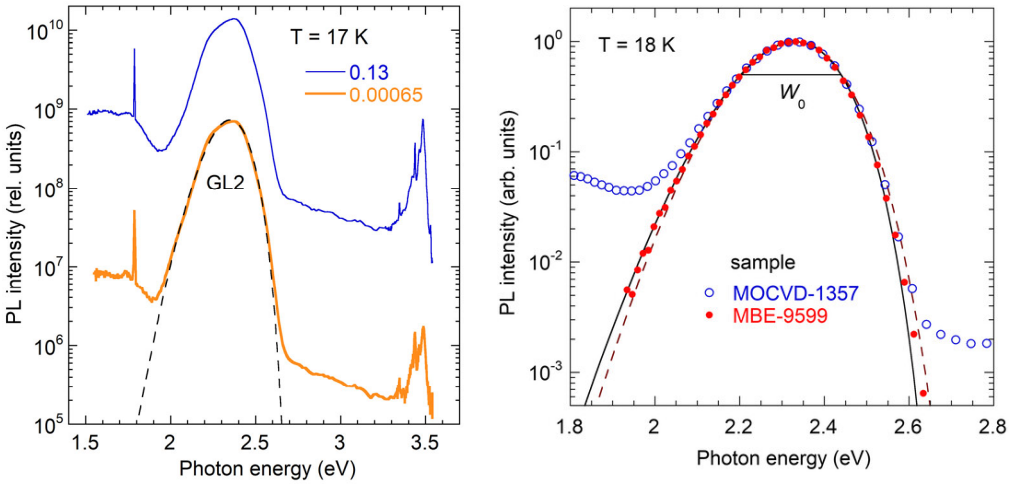

Figure 16. GL2 band. (**a**) SSPL spectra form undoped MBE-grown GaN at T = 17 K and two excitation intensities (P_{exc} = 0.00065 and 0.13 Wcm^{-2}). The dashed line is calculated using Equation (6) with parameters from Table 2. (**b**) Normalized PL spectra at T = 18 K for two GaN:Mg samples. W_0 = 0.234 eV. Reproduced with permission from [47].

The GL2 intensity is temperature-independent below 100 K, decreasing exponentially between 100 and ~200 K with an activation energy $E_1 \approx 0.15$ eV. Unlike the RL2 band (Section 3.2.2), both the $I^{PL}(T)$ and $\tau(T)$ show identical temperature behavior (Figure 17b). This quenching is attributed to thermal electron emission from the excited state to the conduction band, with E_1 representing the depth of the excited state below the CBM.

At temperatures above ~180 K, the quenching accelerates and follows distinct mechanisms depending on the sample conductivity: the TAQ mechanism in SI GaN:Mg and the Schön–Klasens mechanism in conductive *p*-type GaN:Mg [47]. This high-temperature quenching is attributed to the thermal emission of holes from the +/2+ level to the valence band. The +/2+ level is located at E_2 = 0.40–0.43 eV above the VBM as determined from Equation (3) for SI GaN:Mg or Equation (2) for *p*-type GaN:Mg [47]. In principle, transitions from an excited state to the 2+/3+ level may also cause a similar PL band in *p*-type GaN:Mg, since the calculated +/2+ and 2+/3+ levels are very close [47]. However, no clear experimental evidence exists to support the existence of two distinct GL2 bands associated with two charge transition levels in GaN. Thus, the question of whether the experimentally observed GL2 band arises from transitions via the +/2+ or 2+/3+ level remains unresolved.

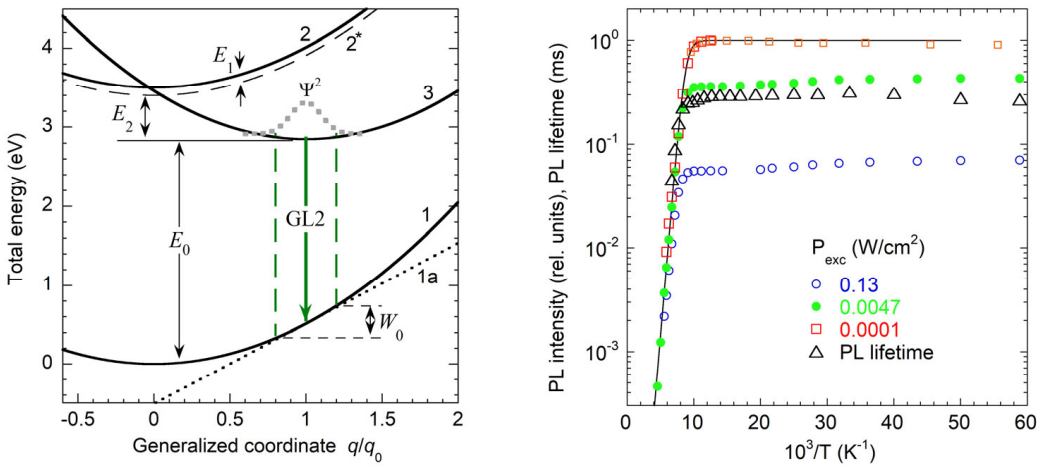

(**a**) (**b**)

Figure 17. GL2 band in GaN. (**a**) Configuration coordinate diagram for the GL2 band. Potential 1 is the ground state. Potential 2 is identical to 1 but shifted up by E_g. Potential 2* describes the defect that captured an electron at a shallow excited state located at E_1 below the CBM. Potential 3 corresponds to the excited state of the defect after it additionally captured a hole at the +/2+ level located at E_2 above the VBM. (**b**) Temperature dependence of the GL2 intensity at three excitation intensities (divided by P_{exc}) and the GL2 lifetime. The line is calculated using Equation (2) with $E_A = E_1 = 0.15$ eV and $C = 4 \times 10^6$.

3.3.3. Aquamarine Band in MBE GaN

A PL band, peaking at ~2.5 eV, was observed in GaN layers grown by MBE on freestanding HVPE GaN substrates [153]. Initially termed the aquamarine luminescence (AL) band due to its color [153,154], it has been eventually identified as the Ca_{Ga}-related GL_{Ga} band [49]. Low-temperature MBE growth of GaN and InGaN often introduces Ca contamination [155–157]. A more detailed analysis of the GL_{Ca} band is provided in Section 4.6.

3.4. Blue Luminescence Bands in Undoped GaN (BL1, BL2, BL3)

Two broad blue luminescence (BL) bands are commonly observed in undoped GaN: the BL1 band, peaking at 2.9 eV, and the BL2 band at 3.0 eV. The third band, BL3, emerges at high excitation intensities in HVPE GaN and is associated with the RY3 defect. All three bands exhibit ZPL and phonon-related fine structure in high-quality GaN samples. These spectral features allow for detailed analysis of their vibrational properties.

3.4.1. Zn_{Ga}-Related BL1 Band

The BL1 band, peaking at 2.9 eV, is observed in undoped GaN grown by MOCVD, HVPE, or AT techniques due to Zn contamination. The assignment of BL1 to Zn_{Ga} acceptors is well established and supported by both experimental and theoretical studies [51,52,57]. The BL1 band exhibits a ZPL at 3.10 eV and distinctive phonon-related fine structure (Figure 18a). At low temperatures ($T < 50$ K), BL1 results from DAP recombination involving shallow donors and the Zn_{Ga} acceptors. A slight blueshift (up to 7 meV) with increasing excitation intensity (inset to Figure 18a) reflects saturation of distant pairs contributing at lower energies, a hallmark of DAP recombination. This shift is constrained by the shallow donor's ionization energy [84,158].

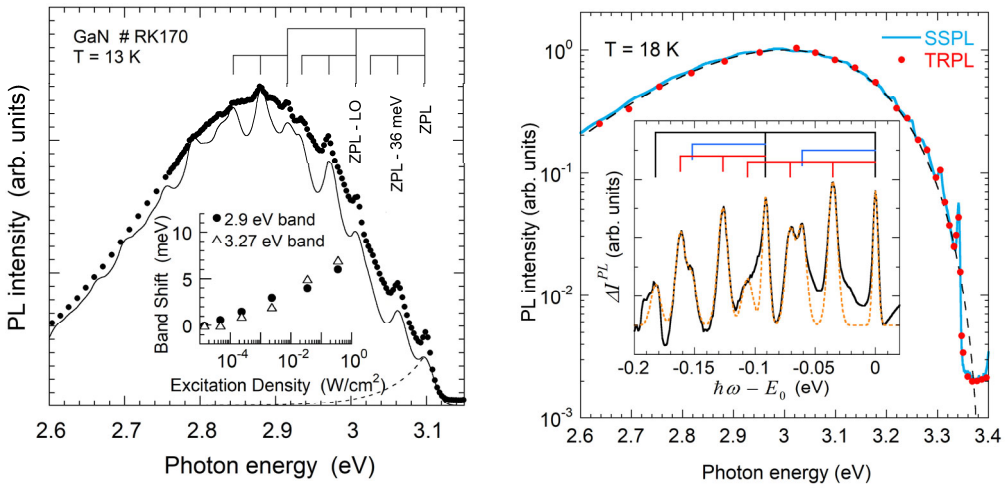

Figure 18. Blue PL bands in undoped GaN grown by MOCVD. (**a**) The Zn_{Ga}-related BL1 band at T = 13 K. The filled circles are the experiment, and the line is the simulation. The superposition of two phonon modes ($\hbar\Omega_{LO}$ = 91.5 meV and $\hbar\Omega_1$ = 36 meV) explains the fine structure. The inset shows the BL1 shift with P_{exc}. Reproduced with permission from [50]. (**b**) Normalized PL spectra of the C_NH_i-related BL2 band. The dashed black curve is calculated using Equation (6) with parameters from Table 2. The inset shows the extracted fine structure (solid black curve) and its deconvolution into Gaussian peaks (dashed orange curve). The BL2 fine structure is formed by a superposition of three phonon modes ($\hbar\Omega_{LO}$ = 91.2 meV, $\hbar\Omega_1$ = 35.4 meV, and $\hbar\Omega_2$ = 61 meV).

The fine structure of the BL1 band, observable at low temperatures, consists of two sets of sharp peaks (Figure 18a). Peaks separated by 36 meV are attributed to a pseudo-local phonon mode, while those at 91.5 meV correspond to the LO phonon mode of the GaN lattice [50]. Vibrational parameters for BL1 and other PL bands in GaN are summarized in Table 3. The Zn_{Ga}-related BL1 band (also referred to as BL_{Zn}) is prevalent in MOCVD- and AT-grown GaN, and occasionally in HVPE GaN, due to unintentional Zn incorporation.

Table 3. Pseudo-local and bulk crystal (LO) phonon modes for PL bands in GaN.

PL Band	Attribution	E_0 (eV)	$\hbar\omega_{max}$ (eV)	$\hbar\Omega_{LO}$ (meV)	$\hbar\Omega_1$ (meV)	$\hbar\Omega_2$ (meV)	$\hbar\Omega_3$ (meV)	Reference
YL1	C_N (−/0)	2.57	2.17	91.5	–	39.5	–	[40]
YL3	Fe? (−/0)	2.38	2.07	91	19	36	–	[43,44]
BL1	Zn_{Ga} (−/0)	3.10	2.86	91	–	36	–	[50]
BL2	C_NH_i (0/+)	3.33	3.0	91.2	–	35.4	61	[55]
BL3	Fe? (0/+)	3.01	2.81	91.3	–	39.6	68.2	[56]
BL_C	C_N (0/+)	3.15	2.85	91.2	–	34.3	–	[60]
BL_{Cd}	Cd_{Ga} (−/0)	2.95	2.70	91	–	39	74	[48,59]
BL_{As}	As_N (0/+)	2.95	2.60	91	–	38	75	[57]
BL_P	P_N (0/+)	3.20	2.89	91	–	37–39	73–77	[57]
UVL_{Mg}	Mg_{Ga} (−/0)	3.28	3.28	91.5	–	–	–	[62]
UVL_{Be3}	Be_{Ga} (−/0)	3.26	3.26	91.5	–	–	–	[45,46]
UVL_{Be}	$Be_{Ga}O_NBe_{Ga}$ (−/0)	3.38	3.38	91.5	–	37.5	–	[64]

3.4.2. C_NH_i-Related BL2 Band

The BL2 band, peaking at 3.0 eV, with a ZPL at 3.33 eV, is distinguished by photo-induced metastability—specifically, PL bleaching under continuous UV laser exposure. In early studies, it was linked to Ga vacancies [159] and was often confused with Zn-related BL1. The concurrent bleaching of BL2 and the rise in the YL1 band upon UV illumination [159–164] suggested a relationship, later attributed to the dissociation of the C_NH_i complex [55]. Under UV exposure, C_NH_i complexes dissociate, the BL2 intensity decreases, and the C_N-related YL1 intensity increases. This metastability is analyzed in Section 4.1.2, while other features of the BL2 band are briefly discussed below (Figure 19).

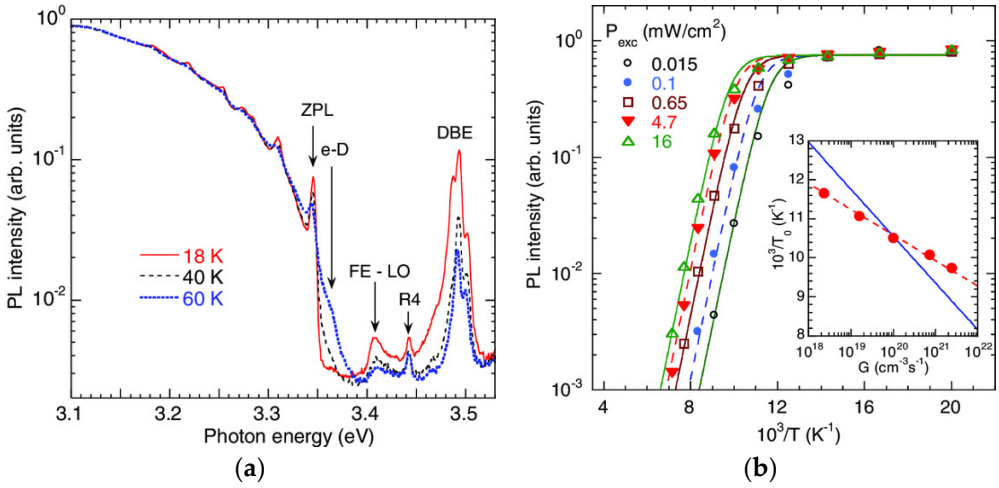

Figure 19. BL2 band in undoped GaN. (**a**) Evolution of the high-energy side of the BL2 band in MOCVD GaN:C (sample MD9856) with increasing temperature at P_{exc} = 0.02 Wcm^{-2}. A high-energy shoulder, labeled e-D, is attributed to electron transitions from the CBM to the ground state of the C_NH_i donor. (**b**) Temperature dependence of the BL2 intensity (normalized at T = 30 K) for selected P_{exc}. Lines are calculated using Equation (2) with E_A = 165 meV. The inset shows the dependence of the critical temperature T_0 on the electron-hole generation rate G fitted with Equation (3). Reproduced with permission from [55].

The BL2 band arises from internal transitions within the C_NH_i donor, specifically from an excited state ~20 meV below the CBM to the ground state 0.15 eV above the VBM [55]. Its exponential decay after a laser pulse at low temperatures ($\tau \approx 300$ ns at $T < 20$ K) confirms the internal transition mechanism. At ~60 K, a high-energy shoulder emerges near the ZPL, indicating contributions from CBM-to-defect transitions (Figure 19a). The ZPL energy remains constant (±0.2 meV) across three orders of magnitude in P_{exc}, further supporting the internal transition model over DAP-type recombination. The fine structure of the BL2 band exhibits phonon replicas involving the LO mode (91–92 meV) and two pseudo-local modes (35.4 and 61 meV) (Figure 18b and Table 3).

The thermal quenching of BL2 is tunable with P_{exc} but not abrupt (Figure 19b), driven by thermal hole emission from the 0/+ level of C_NH_i to the valence band. The hole-capture coefficient for this defect is estimated as $C_p = (4.4 \pm 2.0) \times 10^{-8}$ cm^{3}s^{-1} [55].

3.4.3. RY3-Related BL3 Band

In undoped HVPE GaN samples exhibiting strong RL3 and YL3 bands (Sections 3.1.4 and 3.2.3), a blue band, BL3, emerges at high P_{exc} (Figure 20a). It has super-linear dependence on P_{exc}, a signature of a secondary PL arising from radiative recombination following two-hole capture by a defect [56]. Two ZPLs at 3.0071 and 3.0147 eV are observed, followed by phonon replicas, including LO phonons ($\hbar\Omega_{LO}$ = 91.3 meV) and two pseudo-local vibrational modes ($\hbar\Omega_1$ = 39.6 meV, $\hbar\Omega_2$ = 68.2 meV) (Figure 20b). The BL3 band is attributed to

transitions from excited states 20–30 meV below the CBM to the 0/+ level of the RY3 defect, located ~0.47 eV above the VBM. The two ZPLs likely arise from excited states separated by 7.6 meV [56]. The PL lifetime is short (τ_0 < 10 ns), further supporting a fast internal transition mechanism in a donor-type defect.

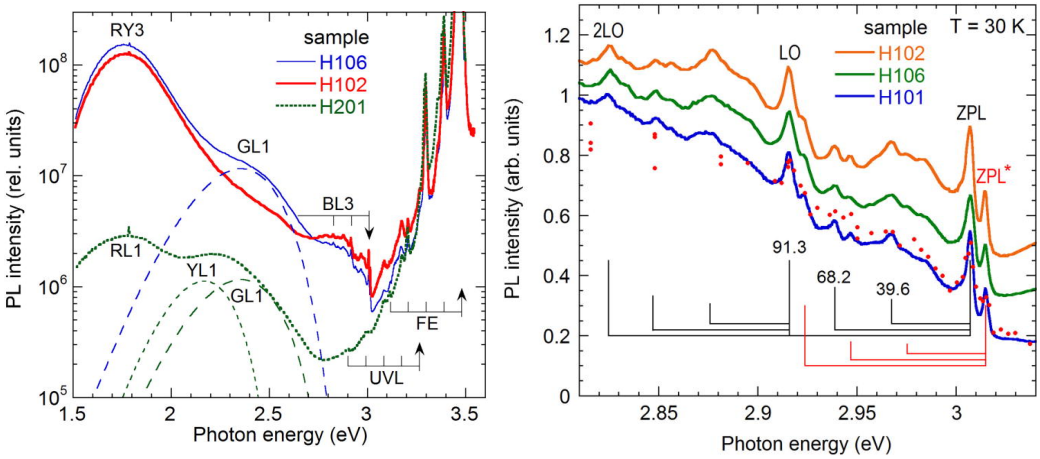

Figure 20. The BL3 band in undoped HVPE GaN at P_{exc} = 100 Wcm^{-2} and T = 30 K. (**a**) SSPL spectra from samples with strong (H102 and H106) and weak (H201) RY3 band. The ZPL and LO phonon replicas of the free exciton (FE), UVL_{Mg}, and BL3 are indicated by arrows and vertical bars, respectively. The long-dashed and short-dashed lines show the contribution of the GL1 and YL1 bands to the spectra simulated using Equation (6) with parameters from Table 2. (**b**) Fine structure at the high-energy side of the BL3 band. The solid curves are SSPL spectra, and the filled circles depict the TRPL spectrum obtained at a time delay of ~5 ns. Two sets of phonon replicas of the ZPL and ZPL* peaks are observed: the LO phonon mode with $\hbar\Omega_{LO}$ = 91.3 meV and two pseudo-local phonon modes with $\hbar\Omega_1$ = 39.6 meV and $\hbar\Omega_2$ = 68.2 meV. Reproduced with permission from [56].

3.5. Ultraviolet Luminescence Band (UVL)

The UVL band peaking at ~3.27 eV, is ubiquitous in undoped GaN grown by various techniques. It results from electron transitions from the conduction band (or shallow donors at low temperatures) to the shallow Mg_{Ga} acceptor with a −/0 level at 0.223 eV above the VBM [40,62,165]. Also known as the shallow DAP or shallow donor-shallow acceptor (SD-SA) band [9,76,166], it is denoted hereafter UVL (or UVL_{Mg} to reflect its Mg_{Ga} origin), as DAP transitions dominate all acceptor-related PL in GaN at low temperatures [66].

Early studies proposed alternative shallow acceptors, including V_{Ga}, C_N, and Si_N [16,166–168]. In particular, Glaser et al. [166] observed a UVL band in MOCVD-grown Si-doped GaN, indistinguishable from UVL_{Mg} in Mg-doped GaN. In those experiments, Si concentrations were (2–3) × 10^{17} cm^{-3}, and the UVL intensity increased with increasing Si content [166,167]. Interestingly, ODMR studies revealed the identical behavior of the UVL band in both Mg- and Si-doped samples, suggesting the involvement of shallow effective-mass acceptors in both cases [166,169]. Note that early theoretical calculations also predicted that C_N and Si_N are shallow acceptors in GaN [17–22]. However, more recent hybrid functional DFT calculations have demonstrated that these impurities form deep acceptor levels: at 0.9 eV for C_N [24] and 2.1 eV for Si_N [103,170].

Based on analysis of a variety of undoped and doped GaN samples grown by various techniques, we concluded that the Mg_{Ga} acceptor is the sole source of the UVL band in undoped GaN (see also Section 4.3.2). Its large hole-capture coefficient (C_p = 10^{-6} cm^{3}s^{-1}) enables efficient hole capture in conductive *n*-type GaN, allowing UVL detection at Mg concentrations as low as 10^{13} cm^{-3} [83], well below the SIMS detection limit (~10^{15} cm^{-3}).

In AT GaN, the UVL_{Mg} band exhibits an atypical shape, particularly reduced ZPL intensity [39,42]. This distortion of the UVL_{Mg} band shape can be explained by self-absorption of PL originating from deeper regions of bulk, high-quality GaN templates, where the diffusion length of photogenerated carriers is relatively large.

3.6. Role of V_{Ga} in GaN Luminescence

Gallium vacancies and related complexes were historically considered the primary origin of the YL band in undoped GaN [16]. However, recent studies have revised this view. Given their high mobility at typical GaN growth temperatures, isolated V_{Ga} are unlikely to persist in as-grown material; instead, they tend to form stable complexes with donors during the cooling phase [14,171,172]. PAS studies by Chichibu et al. [14] identified $V_{Ga}V_N$ complexes as the dominant vacancy-type defects in *n*-type GaN grown by HVPE, MOCVD, and MBE, with concentrations ranging from 10^{16} to 5×10^{17} cm^{-3}, lowest in freestanding HVPE templates (<1×10^{16} cm^{-3}). Tuomisto et al. [172] also concluded that isolated V_{Ga} do not persist in as-grown GaN. In samples with a high concentration of O, they form the $V_{Ga}O_N$ complexes that are stable at growth temperatures [171–175]. Interestingly, in Si-doped HVPE GaN ([Si] = 10^{17}–10^{19} cm^{-3}), V_{Ga} concentrations remain below 10^{16} cm^{-3} [176]. V_{Ga} may also associate with H [139,177,178] and form multi-component complexes, which is common for GaN grown by the AT method [139,179,180]. Nevertheless, in high-quality GaN samples grown by HVPE, MOCVD, and MBE, V_{Ga}-related defects are generally at or below the PAS detection limit (~10^{16} cm^{-3}) [172].

V_{Ga}-related defects are often regarded as nonradiative defects [14,179]. No PL bands in HVPE- or MOCVD-grown GaN could be attributed to the V_{Ga} or the complexes mentioned above [66]. Hybrid functional DFT calculations place the $2-/-$ level of the $V_{Ga}V_N$ complex at 1.75–1.97 eV above the VBM [30,181,182], which excludes it as a candidate for producing PL bands in *n*-type GaN between 1.3 and 3.5 eV. However, a broad band at 0.93 eV, observed after electron irradiation [183], may originate from transitions via this defect. The $V_{Ga}O_N$ complexes are likely nonradiative [35,39,118]. The YL2, OL3, and RL4 bands in AT GaN (Sections 3.1.3 and 3.2.4) are tentatively linked to $V_{Ga}3H_i$, $V_{Ga}O_N2H_i$, $V_{Ga}2O_NH_i$, and $V_{Ga}3O_N$. Nevertheless, these assignments remain speculative and require further experimental validation.

4. Luminescence from Intentionally Introduced Defects

This section examines the PL characteristics of defects intentionally introduced in GaN, with a focus on C, Be, Mg, and Zn.

4.1. Carbon-Related Defects (YL1, BL_C, BL2, RL_C)

Carbon impurities in GaN form C_N acceptors, responsible for the YL1 band, and C_NH_i complexes, associated with the BL2 band. Another blue luminescence (BL_C) band arises as a secondary PL process from C_N upon capturing two holes. The red RL_C band is attributed to C-containing complexes.

4.1.1. PL from the $-/0$ and $0/+$ States of C_N (YL1 and BL_C)

The YL1 band, peaking at ~2.2 eV, is a dominant defect-related PL feature in undoped, Si-doped, or C-Si co-doped *n*-type GaN thanks to efficient hole capture by C_N acceptors (Section 3.1.2). Its long PL lifetime (~100 µs for $n \approx 10^{17}$ cm^{-3}) leads to saturation at low excitation intensities. Subsequent capture of a second hole activates the $0/+$ level, located 0.33 eV above the VBM, producing the BL_C band at 2.85 eV [25]. Figure 21a shows the BL_C emerging superlinearly with P_{exc} as YL1 saturates in conductive *n*-type GaN co-doped with Si and C. Comparing PL efficiencies of YL1 (pre-saturation) and BL_C (after its IQE stops rising) yields a hole-capture coefficient for the $0/+$ level of $C_p \approx 10^{-10}$ cm^3s^{-1}, significantly

lower than values from DLTS [184] or first-principles calculations [185]. This unexpectedly low radiative efficiency could be attributed to the trap-assisted Auger-Meitner (TAAM) recombination, which may become dominant at high P_{exc} [185].

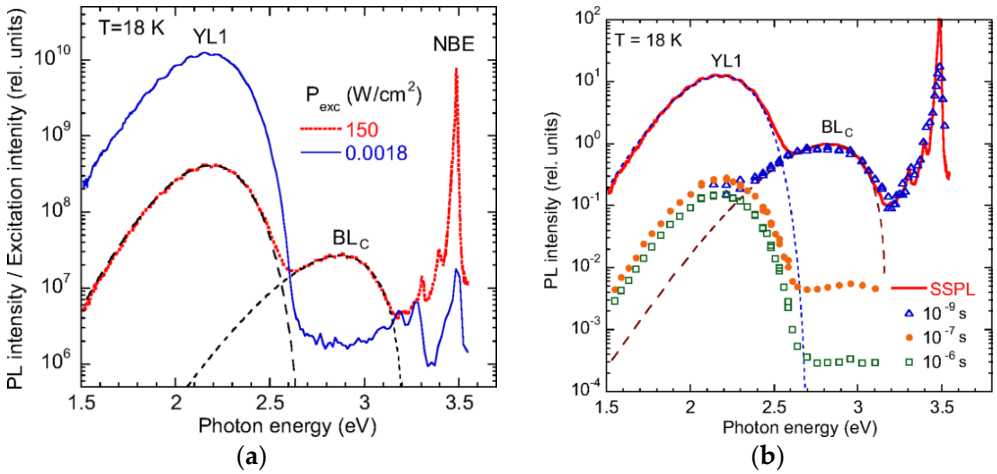

Figure 21. The YL1 and BL_C bands in GaN:C,Si ($n_0 = 7.5 \times 10^{17}$ cm^{-3}) at $T = 18$ K. (**a**) SSPL spectra at low and high excitation intensity. PL intensity is normalized to P_{exc} for the convenience of comparison. (**b**) Comparison of SSPL ($P_{exc} = 150$ Wcm^{-2}) and TRPL (at indicated time delays) spectra. Dashed lines are calculated using Equation (6) with parameters from Table 2. Reproduced with permission from [25].

TRPL reveals fast (~1 ns) and exponential BL_C decay, with only YL1 persisting beyond 0.1 μs after a laser pulse (Figure 21b). Across samples with free electron concentrations between 3×10^{16} cm^{-3} and 3.8×10^{18} cm^{-3}, BL_C lifetimes range from 0.27 to 1.3 ns [25]. This short and almost insensitive to n PL lifetime is modeled by competing internal transitions (from an excited state near the CBM to the 0/+ level) and transitions from the conduction band, with contributions varying with n (Figure 22a). The model yields a high electron-capture coefficient for BL_C ($C_n \approx 10^{-9}$ cm^{3}s^{-1}). A configuration-coordinate diagram in Figure 22b illustrates transitions leading to YL1 and BL_C in C-doped GaN. The experiments supported theoretical predictions of two charge transition levels for C_N [105,107] and confirmed that the YL1 band is caused by the isolated C_N [24,25]. The C_NO_N complexes, erroneously considered as the origin of YL1 [105,106,142], are either weakly radiative or not formed in sufficient concentration, and therefore are absent in PL spectra (Section 4.1.4).

DLTS studies provided independent evidence that the C_N defect in GaN possesses two charge transition levels. Employing low-frequency capacitance DLTS for MOCVD-grown *p*-type GaN:Mg, Narita et al. [26] found the 0/+ level of the C_N at 0.29 eV above the VBM at $T \approx 135$ K by correlating the DLTS signals with C concentration. The most precise determination of the 0/+ level at low temperatures was achieved via PL measurements (Figure 23). From the ZPL at 3.172 eV, the 0/+ transition level of C_N is found at 0.33 ± 0.01 eV above the VBM [60]. Phonon-related fine structure reveals coupling to the LO crystal mode and a pseudo-local mode of 34.3 meV (Figure 23b). The experimentally determined 0/+ level of the C_N agrees with values of 0.23–0.36 eV obtained from first-principles calculations [25,107,182].

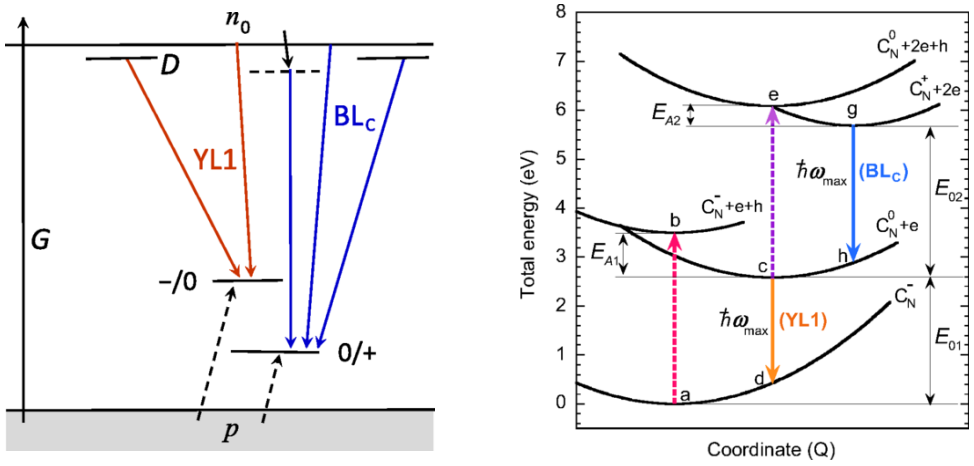

(**a**) (**b**)

Figure 22. Transitions leading to YL1 and BL_C in C-doped GaN. (**a**) Schematic band diagram with transitions leading to YL1 and BL_C. (**b**) Configuration coordinate diagram for the C_N defect in GaN. E_{01} and E_{02} are the ZPLs of the YL1 and BL_C bands, respectively. The upward red and purple arrows correspond to the generation of free electrons and holes by photons with the energy equal to E_g. Reproduced with permission from [25].

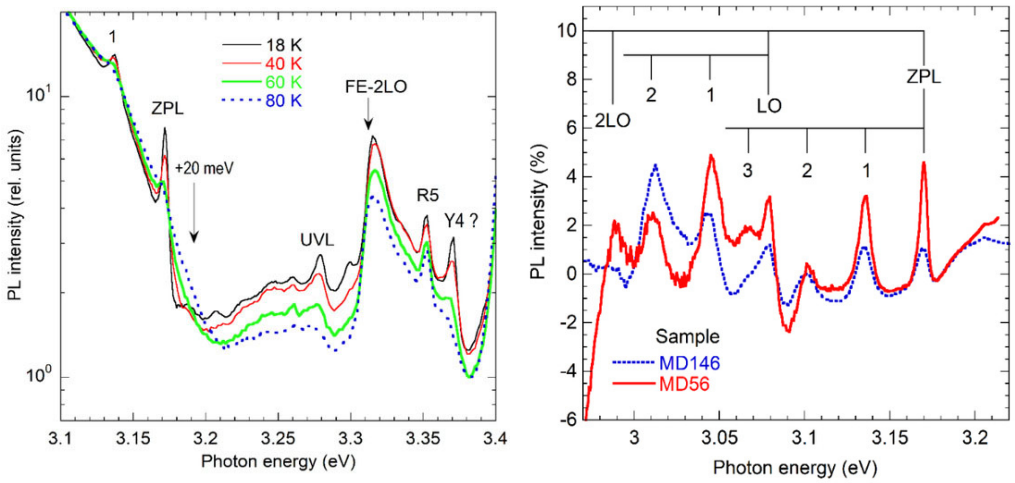

(**a**) (**b**)

Figure 23. Fine structure of the BL_C band in C-doped GaN. (**a**) Transformation of PL spectrum at P_{exc} = 100 Wcm^{-2} with temperature. The ZPL of the BL_C band at 3.172 eV decreases, and a shoulder "+20 meV" increases with temperature. (**b**) Fine structure of the BL_C band after subtracting the smooth component. Two LO phonon replicas of the ZPL at distances integer of $\hbar\Omega_{LO}$ = 91.2 meV and several pseudo-local phonon replicas (labeled with n = 1, 2, 3) with $\hbar\Omega_1$ = 34.3 meV are indicated. Reproduced from [60].

4.1.2. PL from the C_N and C_NH_i (YL1 and BL2)

In high-resistivity or SI GaN, particularly in MOCVD-grown samples, the YL1 and BL2 bands are dominant features in the defect-related low-temperature PL spectrum (Sections 3.1.2 and 3.4.2). These bands originate from carbon-related defects: substitutional carbon (C_N) and its hydrogenated form (C_NH_i). Hydrogen is a ubiquitous impurity in GaN, especially in samples grown by MOCVD. Hydrogen is mobile at growth temperatures only in the form of H^+ ions [186,187], and it is positively charged when the Fermi level lies more than ~0.5 eV below the CBM [55]. Consequently, C_NH_i complexes are formed, and the BL2 band is observed only in high-resistivity n-type and in p-type GaN. The metastable behavior of PL in such samples—specifically, the interplay between the YL1 and BL2 bands,

driven by reversible formation and dissociation of C_NH_i complexes and influenced by UV exposure or thermal annealing—is analyzed below [55,188].

Under continuous above-bandgap excitation at low temperatures (T < 80 K), BL2 band bleaches, while the YL1 intensity increases simultaneously (Figure 24a) [55,159–164,188–191]. This behavior is explained by photo-induced dissociation of C_NH_i, with a dissociation probability per recombination event of $\gamma = 5 \times 10^{-8}$ [55], implying one dissociation per 10^7–10^8 radiative recombination events involving the complex, in agreement with earlier estimates [164]. This bleaching is permanent at low temperatures but can be reversed at room temperature after a few days, implying a barrier of ~1 eV for the complex formation [188]. Quantitative analysis of these processes yields a hole-capture coefficient ratio of $C_{p,BL2}/C_{p,YL1} = 0.12$ and also allows for the extraction of defect concentrations [55].

Thermal annealing has a pronounced effect on the stability of C_NH_i complexes in GaN. Annealing in N_2 ambient at T_{ann} > 700 °C leads to the dissociation of C_NH_i and the subsequent removal of hydrogen from MOCVD-grown GaN samples, resulting in a drastic reduction in the BL2 intensity (Figure 24b). Remarkably, the BL2 band can be fully restored by annealing in an H_2 + N_2 atmosphere at 650–850 °C, confirming the incorporation of H and restoration of C_NH_i complexes [55].

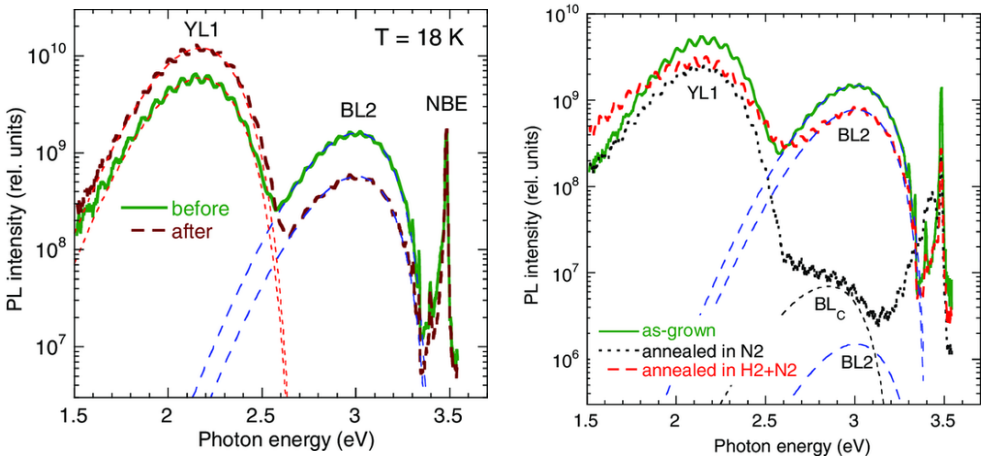

Figure 24. Interplay between YL1 and BL2 in MOCVD-grown GaN at T = 18 K, $P_{exc} = 10^{-4}$ Wcm^{-2}. (**a**) PL spectra before and after 80 min of continuous excitation with a HeCd laser at P_{exc} = 0.13 Wcm^{-2}. The thin dashed lines are calculated using Equation (6) with parameters from Table 2. (**b**) Thermal annealing effects: annealing in N_2 at 850 °C for one hour quenches BL2 (by > 10^3), while additional annealing in H_2 + N_2 at 850 °C for 1 h restores its intensity. Dashed lines are calculated using Equation (6) with parameters from Table 2. The BLc band is caused by electron transitions via the 0/+ level of the C_N defect (Section 4.1.1). Reprinted with permission from [55].

The effect of annealing (in N_2 ambient at T_{ann} between 300 and 1000 °C) on the YL1 band in MOCVD-grown undoped GaN was studied in detail in [188] (filled blue squares in Figure 25a). The drop in the YL1 intensity at T_{ann} = 350–400 °C corresponds to a ~2 eV activation energy. This behavior was explained by the release of hydrogen from unidentified nonradiative defects and its subsequent capture by C_N [188]. One of the samples was isochronally annealed in vacuum (for 30 min with 25 °C steps up to T_{ann} = 400 °C) and exhibited a similar trend (empty squares in Figure 25a). Annealing at T_{ann} > 900 °C permanently removed H from the samples (as evidenced by the disappearance of BL2) and restored YL1 intensity.

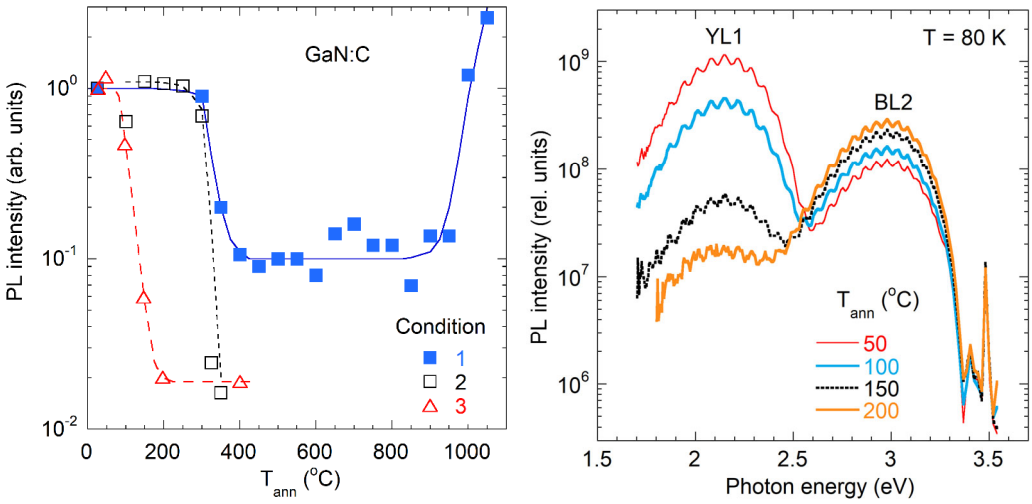

Figure 25. The effect of thermal annealing on the YL1 and BL2 bands in MOCVD GaN. (**a**) The YL1 intensity (T = 18 K and P_{exc} = 10^{-4} Wcm^{-2}) vs annealing temperature (lines are guides to the eye): (1) Solid squares—separate 5 × 5 mm pieces were annealed for one hour in N_2 ambient at selected T_{ann} (350–1000 °C). (2) Empty squares—YL1 intensity in another piece after sequential 30 min annealing in vacuum at (100–350 °C). (3) Empty triangles—after annealing in vacuum at 400 °C, the YL1 intensity was fully restored by a 2 h HeCd laser exposure (P_{exc} = 0.13 Wcm^{-2}) at T = 80 K, and the sample was in situ annealed in vacuum (25–400 °C). (**b**) Evolution of PL spectrum at 80 K after consecutive 30-min-long steps of in situ annealing in vacuum (corresponding to condition (3)) at indicated temperatures. Reprinted from [188].

Interestingly, when C_N defects were initially passivated by H (through annealing at 400–800 °C) and subsequently reactivated via photo-induced dissociation of C_NH_i at cryogenic temperatures, additional annealing at significantly lower temperatures (T_{ann} = 100–150 °C) resulted in a pronounced decrease in YL1 intensity and a concurrent increase in BL2 intensity (Figure 25b and empty triangles in Figure 25a). These observations suggest that after low-temperature photo-induced dissociation of C_NH_i, H remains in close proximity to C_N, separated by an energy barrier of ~1 eV, and readily re-passivates the C_N upon mild annealing or even at room temperature (after a couple of days) [188].

A similar annealing response (except for the photo-induced activation) was observed for the Be_{Ga}-related YL_{Be} band [188]. The YL_{Be} intensity dropped by up to an order of magnitude at $T_{ann} \approx 400$ °C, which was attributed to the release of hydrogen from unknown traps and passivation of Be_{Ga} acceptors. Interestingly, the YL_{Be} intensity slowly recovered at room temperature (on a timescale of months) [188].

4.1.3. RL_C Band in C-Doped GaN

In HVPE-grown GaN doped with carbon, the intensities of the YL1 and BL2 bands decrease markedly as the concentration of C increases from ~10^{18} to 3 × 10^{19} cm^{-3} [33]. This trend has been attributed to the formation of tri-carbon complexes that outnumber isolated C_N centers in heavily doped GaN [33,192]. At these high carbon concentrations, a red luminescence (RL_C) band, peaking at 1.62 eV, emerges [33,193]. The RL_C band is mostly excited under below-bandgap excitation (resonantly), and its PLE spectrum has a Gaussian shape with a maximum at 2.7 eV (Figure 26a). The RL_C is quenched above 80 K, revealing an activation energy of ~0.1 eV. Based on these observations, Zimmermann et al. [33] attributed RL_C to tri-carbon complexes. They proposed that this defect has a ground state at about 1.1 eV above the VBM and an excited state at 0.1 eV below the CBM.

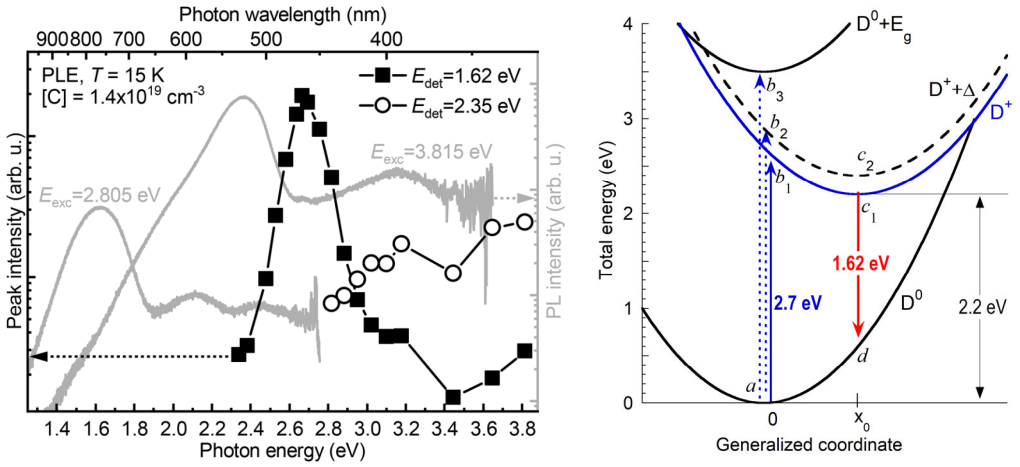

Figure 26. The RL_C band in C-doped GaN. (**a**) PL spectra excited with above-bandgap (3.815 eV) and below-bandgap (2.805 eV) light are shown with light gray curves. The PLE spectrum of the 1.62 eV band is shown with filled squares. Reproduced from [33]. (**b**) Configuration-coordinate diagram with transitions explained in the text.

Figure 26b illustrates a configuration coordinate diagram adapted from [33] to explain the PL and PLE characteristics of the RL_C band. In the ground state, the defect is a neutral donor D^0 (the lowest parabola). Resonant excitation (transition a-b_1) promotes an electron from the donor ground state to an excited state located at Δ = 0.1 eV below the CBM, producing the PLE peak at 2.7 eV. The system then relaxes (b_1-c_1) to a new equilibrium position x_0 via phonon emission. Radiative recombination (c_1-d) produces the RL_C band with a maximum at 1.62 eV, and the defect system returns (d-a) via phonon emission to the initial state. Such internal transitions, not involving the valence or conduction band, are known to produce nearly Gaussian PLE spectra [94], consistent with experimental observations (Figure 26a).

If electrons were excited to the conduction band (transition a-b_2), the PLE spectrum would show a stepwise rise (instead of a Gaussian shape) due to continuous states in the conduction band [94]. According to the results shown in Figure 26a, such contributions are negligible, suggesting that electrons excited to the conduction band predominantly recombine nonradiatively via some other defects.

The transition a-b_3 in Figure 26b corresponds to the above-bandgap excitation of an electron-hole pair when the defect is in the ground state D^0. It appears that the capture of holes (transition b_3-c_2) is inefficient for these defects (because they are donors, and there may also be a potential barrier for the hole capture). This would explain why the RL_C band is very weak (or not observed) under above-bandgap excitation [33].

A similar behavior was observed for F centers that are deep donors in alkali halides, with excited states near the CBM [194–197]. The shapes of PL and PLE bands for F centers are Gaussian. PL quenching begins at $T \approx 100$ K, and the quenching is attributed to thermal emission of electrons from the excited state to the conduction band. Similar to the RL_C band in GaN, PL from F centers is efficiently excited via resonant excitation, but remains undetectable under above-bandgap excitation [198].

4.1.4. Other Carbon-Related Complexes

Although C_NO_N complexes were initially suggested as potential contributors to the YL band [105,106], more recent hybrid functional DFT calculations indicated insufficient binding energies for C_NO_N and C_NSi_{Ga} to form at concentrations comparable to isolated C_N [98]. Specifically, for GaN grown at 1300 K and co-doped with C and Si, the predicted

concentration of C_NSi_{Ga} complexes is less than 1% of the isolated C_N concentration when the concentration of shallow Si_{Ga} donors is ~10^{18} cm^{-3}. The C_NO_N, with lower binding energy, is expected to be present at even lower levels [98].

Figure 27 presents SSPL and TRPL spectra at T = 17 K from a MOCVD-grown GaN sample co-doped with C (7×10^{17} cm^{-3}) and Si (1.4×10^{18} cm^{-3}). The only emission observed below 3 eV is the YL1 band. Its characteristic features (the band shape, hole- and electron-capture coefficients, the ZPL at 2.59 eV, and BL_C band emerging at high P_{exc}) confirm its origin from the isolated C_N. The SSPL and TRPL spectra are identical (the simulated lineshape is shown with the orange dashed line), further confirming that no other PL bands contribute to the broad yellow band. The residual background observed between 2.7 and 3.0 eV is attributed to monochromator stray light, as confirmed by the use of interference filters. A hypothetical C_NSi_{Ga} band, predicted to occur in the 2.3–2.7 eV range [98,103], is not observed. Its estimated intensity, represented with the dotted line in Figure 27, is at least four orders of magnitude lower than YL1. Thus, C_NO_N and C_NSi_{Ga} complexes are not observable in PL, due to low concentrations [98] and relatively low hole-capture coefficients, as these complexes are donors.

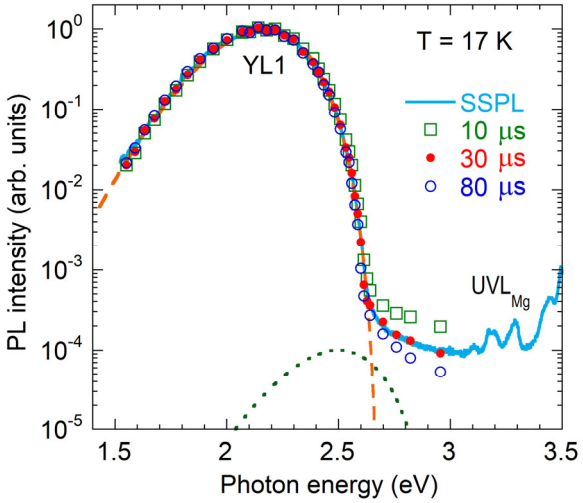

Figure 27. Normalized SSPL and TRPL spectra at T = 17 K from MOCVD-grown GaN co-doped with C (7×10^{17} cm^{-3}) and Si (1.4×10^{18} cm^{-3}). The orange dashed line is calculated using Equation (6) with parameters for the YL1 band from Table 2. The dotted curve with a maximum at 2.5 eV illustrates the maximum possible contribution from C_NSi_{Ga} complexes.

4.2. Beryllium-Related Defects (YL_{Be}, UVL_{Be3}, UVL_{Be}, RL_{Be}, BL_{Be}, GL_{Be})

Beryllium (Be) doping in GaN introduces a variety of defect-related PL bands, including YL_{Be}, UVL_{Be3}, UVL_{Be}, RL_{Be}, BL_{Be}, and GL_{Be}. This section summarizes their experimental characteristics, theoretical interpretations, and associated defect models.

4.2.1. Historical Overview

For a long time, the Be_{Ga} acceptor was regarded by experimentalists and theorists as the shallowest acceptor in GaN and was proposed as an alternative to Mg_{Ga} for achieving *p*-type doping [199–205]. However, more recent first-principles calculations have demonstrated that Be_{Ga} is a deep acceptor with the predicted $-/0$ level at 0.45–0.65 eV above the VBM [206–209]. In addition to this deep state, the theory also predicted a shallow state with a delocalized hole [206,210]. Early experimental PL studies revealed two primary Be-related bands (Figure 28a): a broad yellow band with a maximum at 2.15 eV (YL_{Be}) and a UVL band consisting of a sharp peak at 3.38 eV accompanied by a few LO phonon replicas (UVL_{Be}). Initially, YL_{Be} was attributed to various Be-containing complexes, includ-

ing $Be_{Ga}O_N$ donors [211], $Be_{Ga}V_NBe_{Ga}$ acceptors [150], and Be_iV_{Ga} complexes [212]. The UVL_{Be} band was erroneously attributed to the shallow Be_{Ga} acceptor [150,199–203,210]. PL bands in Be-doped GaN were the subject of continued debate until the dual nature of the Be_{Ga} acceptor was experimentally verified [45]. Comprehensive PL studies [45,46,213,214], in fair agreement with early theoretical predictions [206], have led to a consistent model of the Be_{Ga} acceptor in GaN (Figure 28b).

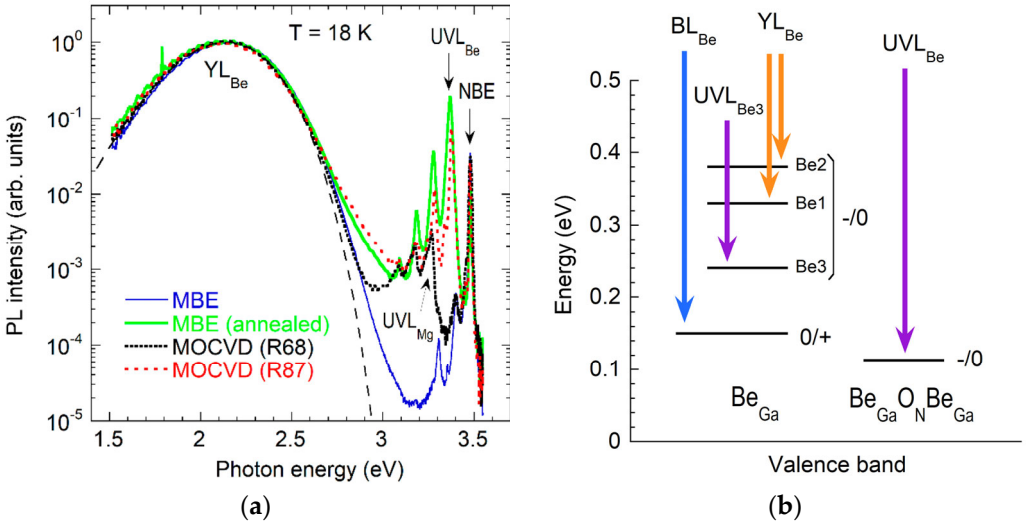

Figure 28. PL bands in Be-doped GaN. (**a**) Normalized PL spectra at T = 18 K from MBE-grown GaN:Be (as-grown and annealed at 800 °C) and two MOCVD GaN:Be (R68 and R87). The dashed line is calculated using Equation (6) with parameters from Table 2. The UVL_{Be} band appears in MBE GaN:Be samples only after thermal annealing. In MOCVD GaN:Be, the UVL_{Be} band is strong in some samples (such as R87) but cannot be resolved in others (R68). The Mg_{Ga}-related UVL_{Mg} band in MOCVD GaN:Be samples is from Mg contamination. Reproduced from [46]. (**b**) Schematic energy level diagram of main Be-related defects. Electron transitions from the conduction band (or shallow donors at T < 50 K) to Be1 and Be2 levels of Be_{Ga} produce the YL_{Be} band; transitions to the shallow Be3 level of Be_{Ga} yield the UVL_{Be3} band. The UVL_{Be} band at 3.38 eV is attributed to $Be_{Ga}O_NBe_{Ga}$ complexes. The BL_{Be} band is proposed to originate from transitions via the 0/+ level of Be_{Ga}.

According to this model, the Be_{Ga} acceptor forms two deep, polaronic states (Be1 and Be2) in which the hole is localized on adjacent nitrogen atoms, and a shallow state (Be3) with a delocalized hole. The −/0 transition levels for these states are experimentally found at 0.35 ± 0.03 eV (Be1), 0.39 ± 0.02 eV (Be2), and 0.24 ± 0.01 eV (Be3) above the VBM [45,46]. Recent temperature-dependent Hall-effect measurements on MOCVD-grown GaN:Be samples have confirmed the *p*-type conductivity associated with the Be_{Ga} acceptor level at 0.40 ± 0.02 eV above the VBM [215]. Electron transitions from the conduction band to Be1 and Be2 levels are responsible for the YL_{Be1} and YL_{Be2} components of the YL_{Be} band. Transitions via the shallow Be3 level result in a distinct PL band (labeled UVL_{Be3}) with a peak at 3.26 eV followed by LO phonon replicas. In bulk GaN:Be grown by the high nitrogen pressure solution (HNPS) method, these PL bands can also be found. However, a significant contribution of the C_N-related YL1 band in those samples and blurred PL bands can complicate the attribution of individual PL features [46].

The UVL_{Be} band at 3.38 (initially thought to be caused by isolated Be_{Ga}) has recently been attributed to the $Be_{Ga}O_NBe_{Ga}$ complex [64]. The BL_{Be} band with a maximum at 2.6 eV is preliminarily attributed to the 0/+ transition level of Be_{Ga} [61].

4.2.2. Three States of Isolated Be_{Ga} (YL_{Be1}, YL_{Be2}, UVL_{Be3})

At temperatures below $T_1 \approx 80$–100 K, photogenerated holes in GaN:Be are efficiently captured by the shallow Be3 level (0.24 eV above the VBM). These holes rapidly relax, via barrier-free transition, into the Be1 level at 0.35 eV. A significant energy barrier (>0.17 eV) between Be1 and Be2 polaronic states prevents hole transfer to the deepest Be_{Ga} level (Be2) at these temperatures. Consequently, the YL_{Be} band is observed, caused by electron transitions from the CBM (or from shallow donors at $T < 50$ K) to the Be1 level (YL_{Be1}). According to ODMR studies on MBE-grown GaN:Be [216], the Be_{Ga} polaronic state (apparently Be1 causing the YL_{Be} at $T = 1.6$ K) is characterized by isotropic $g = 2.004 \pm 0.002$.

At $T \approx T_1$, a thermally activated transition occurs: the hole relocates from an in-plane N atom to the c-axis N atom, corresponding to the lowest energy configuration Be2, and the YL_{Be1} component (transitions to Be1) is replaced by YL_{Be2} (transitions to Be2). As a result, the YL_{Be} band redshifts by about 40 meV at $T \approx T_1$. Though the radiative lifetimes of the two components are comparable ($\tau_{n1}/\tau_{n2} = 1.2 \pm 0.2$), a noticeable discontinuity appears in the measured PL lifetime at $T \approx T_1$ (Figure 29a). This is due to rapid hole transfer from Be1 to Be2, occurring on a timescale shorter than the YL_{Be1} lifetime at $T > T_1$.

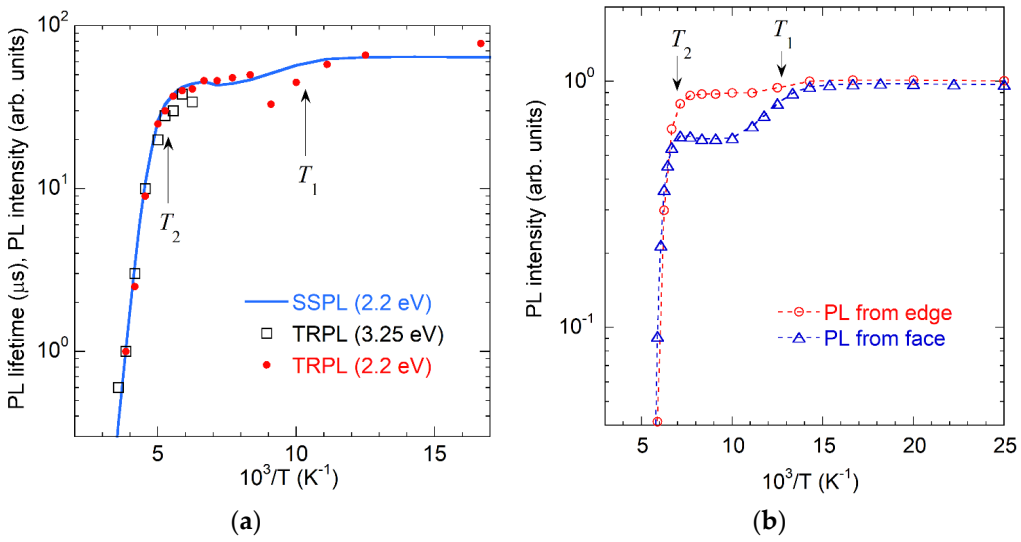

Figure 29. Two-step quenching of the YL_{Be} band in GaN:Be. (**a**) Temperature dependences of PL lifetimes for the YL_{Be} (filled circles) and UVL_{Be3} (empty squares) and the YL_{Be} intensity (solid line) in *n*-type GaN:Be. (**b**) Temperature dependence of the YL_{Be} intensity (normalized at 18 K) in SI GaN:Be for two detection geometries. The YL_{Be} intensity decrease at $T > T_1$ for the "PL from face" case is caused by the drop in extraction efficiency, not IQE loss. Reproduced with permission from [45].

The YL_{Be} band consistently exhibits two-step quenching at temperatures T_1 and T_2 (Figure 29). In SI GaN:Be samples, both quenching steps are tunable with P_{exc}, i.e., T_1 and T_2 increase with increasing P_{exc} (the TAQ mechanism). Notably, the second step is abrupt in SI samples and exhibits an apparent activation energy (up to 1.5 eV) that is unrelated to the ionization energy. In contrast, in conductive *n*-type GaN:Be samples, the two-step quenching is neither tunable nor abrupt. The second quenching step in such samples is described by the Schön–Klasens quenching mechanism, and the activation energy of approximately 0.30 eV corresponds to the Be2 ionization energy, although thermal emission of holes from Be2 occurs via the Be3 level [45].

Interestingly, the IQE of the YL_{Be} band remains unchanged when the temperature passes T_1 [213]. The observed PL intensity drops at $T \approx T_1$ due to reduced light extraction efficiency from c-axis dipoles (Be2 polarons) [45], the axis of which in GaN:Be layers grown on c-plane sapphire coincides with the direction of PL observation. The magnitude of

the PL drop during the first quenching step is sample-dependent and depends on the PL detection geometry (Figure 29b). In agreement with the prediction [45], the YL_{Be} intensity rises at $T > T_1$ in bulk GaN:Be crystals when PL is observed in a direction perpendicular to the GaN c-axis [217].

The dual nature of the Be_{Ga} acceptor, which possesses both deep polaronic and shallow delocalized hole states, was verified with PL experiments, where the UVL_{Be3} band emerging at $T > 100$ K (Figure 30) provided key evidence [45].

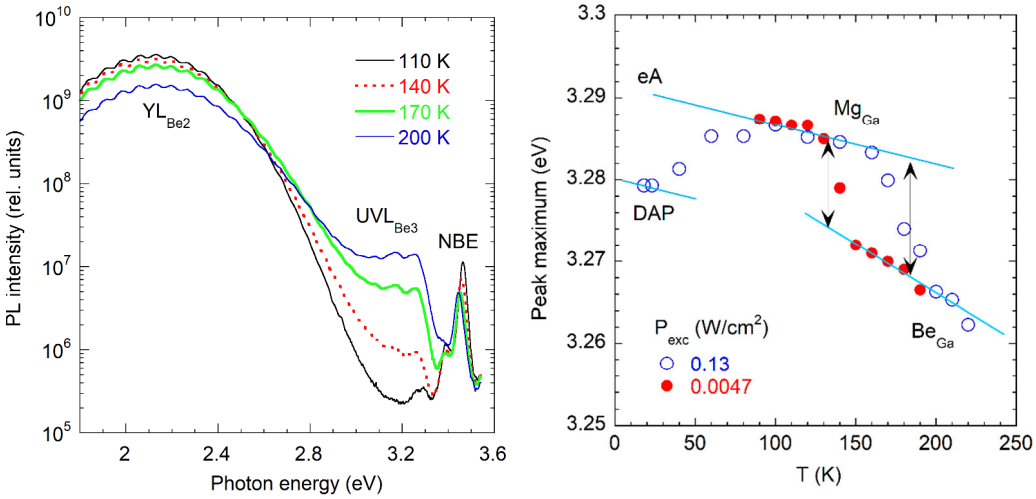

(a) (b)

Figure 30. TheUVL_{Be3} band in GaN:Be. (**a**) SSPL spectra from MBE-grown *n*-type GaN:Be (sample 0020–1) at selected temperatures. (**b**) Temperature dependence of UVL peak position in MOCVD-grown SI GaN:Be (sample R134). The UVL_{Mg} band is quenched at $T \approx 130$ K ($P_{exc} = 0.0047$ W/cm^2) or $T \approx 170$ K ($P_{exc} = 0.13$ W/cm^2) by the TAQ mechanism. At these temperatures, the UVL_{Mg} band is replaced with the UVL_{Be3} band. Reproduced with permission from [45,46].

The UVL_{Be3} band was initially overlooked due to its similarity to the UVL_{Mg} band, which originates from the shallow Mg_{Ga} acceptor (ZPL at 3.27–3.29 eV, followed by LO phonon replicas). The UVL_{Mg} band typically quenches at $T > 100$ K and disappears by 200 K in undoped GaN due to the low ionization energy of the Mg_{Ga} acceptor (0.223 eV). However, in Be-doped GaN, a similar PL band emerges at $T > 100$ K, exponentially increasing with temperature (Figure 30a). In Mg-contaminated GaN:Be samples, both the UVL_{Mg} and UVL_{Be3} can be spectrally resolved, revealing that the UVL_{Be3} ZPL is ~15 meV below the UVL_{Mg} ZPL (Figure 30b).

The UVL_{Be3}/YL_{Be2} intensity ratio increases exponentially with temperature (Figure 31a) and fits well the expression:

$$\frac{I_{Be3}^{UVL}}{I_{Be2}^{YL}} = \delta \exp\left(\frac{-\Delta E_{23}}{kT}\right) \quad (9)$$

where $\delta = \tau_{n2}/\tau_{n3}$, τ_{n2} and τ_{n3} are intrinsic PL lifetimes of radiative transitions via Be2 and Be3, respectively, and ΔE_{23} is the energy difference between the respective levels. Fitting yields $\Delta E_{23} = 0.15 \pm 0.02$ eV and $\delta \approx 10$ across multiple GaN:Be samples grown by MBE and MOCVD. This behavior reflects Boltzmann population redistribution between Be2 and Be3 states [45]. Interestingly, the measured PL lifetimes of the UVL_{Be3} and YL_{Be2} bands are identical at all temperatures (Figure 29a). It was shown in Ref. [45] that the true PL lifetime of PL via the Be3 level is about 10 times shorter than that of the YL_{Be2} band, as is expected for shallow and deep acceptors [34]. However, thanks to dynamic feeding after a laser pulse, the Be3 state is continuously populated by hole transfer from Be2, resulting in synchronized PL decay [45].

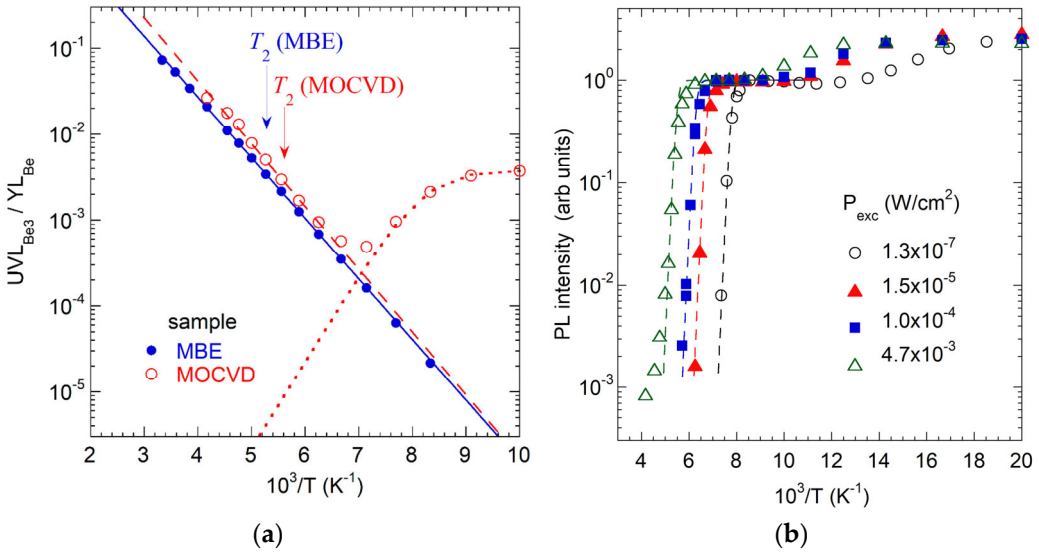

Figure 31. Effect of temperature on PL from the Be_{Ga} acceptor in GaN. (**a**) Temperature dependence of the integrated UVL_{Be3} and YL_{Be} intensities ratio in two GaN:Be samples. The lines are calculated using Equation (9) with the following parameters: ΔE = 140 meV, δ = 18 (solid line), and ΔE = 145 meV, δ = 35 (dashed line). The dotted line is calculated using Equation (2) with $C = 2 \times 10^8$ and E_A = 200 meV. The arrows show the critical temperature of the YL_{Be} quenching. Reproduced from [46]. (**b**) Tunable and abrupt quenching of the YL_{Be} band in *p*-type GaN:Be.

Thermal quenching of UVL_{Be3} and YL_{Be2} begins at $T = T_2 \approx$ 120–200 K. In SI and high-resistivity *p*-type GaN:Be samples, the quenching is tunable and abrupt (Figure 31b). In conductive *n*-type GaN:Be samples, the YL_{Be} quenching begins at $T_2 \approx$ 200 K, and the slope of the quenching reveals an activation energy of 0.30 eV. Initially, the activation energy was attributed to the deep level of Be_{Ga}. However, according to the above model, the quenching is primarily caused by the thermal emission of holes from the shallow Be3 level to the valence band [45]. The effective activation energy for the YL_{Be} quenching corresponds to the sum of Be3 energy (about 0.20 eV at T = 200 K) and the energy difference between the Be3 and Be2 levels (~0.15 eV). It should be noted that activation energies extracted from PL quenching slopes are typically slightly lower than the true defect ionization energy, due to several factors [66,75].

The results of the hydrostatic pressure experiments [211] have been interpreted using a model in which the broad yellow band in HNPS-grown GaN:Be consists of a C_N-related YL1 band and a yellow band caused by the $Be_{Ga}O_N$ complex. According to first-principles calculations in [211], the polaronic 0/+ level of $Be_{Ga}O_N$ shifts from 0.26 eV to 0.12 eV above the VBM as hydrostatic pressure increases from 0 to 8 GPa. At higher pressures, a UVL band (with a peak at ~0.2 eV below the bandgap) emerges and is attributed to the shallow 0/+ level of $Be_{Ga}O_N$ with a delocalized hole, reflecting its dual nature. The model based on isolated Be_{Ga} was dismissed in [211], primarily because the calculated PL band maximum of the Be_{Ga} polaron (1.80 eV) markedly disagreed with the experimentally observed YL_{Be} maximum. However, these experimental results can be well explained with the above-discussed model of the isolated Be_{Ga}, in which the deep Be1 level shifts toward the VBM (by ~0.17 eV under 8 GPa pressure [211]) and intersects with the shallow Be3 level, resulting in a sudden intensification of the UVL_{Be3} band [46].

4.2.3. Shallowest Acceptor in GaN (UVL_{Be})

The UVL_{Be} band at 3.38 eV, initially misattributed to a shallow level of Be_{Ga} [210], arises from Be doping and exhibits all characteristic features of the shallowest acceptor in GaN [64]. Figure 32a shows two components of the UVL_{Be} band (eA and DAP) observed

in two GaN:Be samples grown by MOCVD. Both UVL_{Mg} and UVL_{Be} bands feature a sharp ZPL followed by a few LO phonon replicas. The Huang–Rhys factor, S, defined as the intensity ratio of the first phonon replica to the ZPL, is 0.15 for the UVL_{Be}—the lowest among GaN defects—indicating the lowest electron–phonon coupling strength [64].

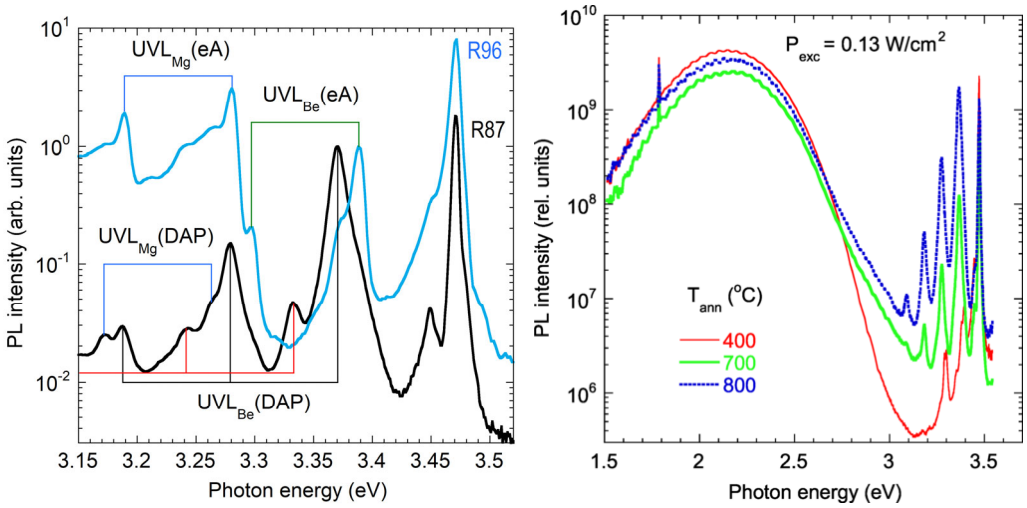

(**a**) (**b**)

Figure 32. The UVL_{Be} band in GaN:Be. (**a**) SSPL spectra at T = 18 K and P_{exc} = 0.005 Wcm^{-2} (normalized to the UVL_{Be} peak) for two Be-doped GaN samples grown by MOCVD (R87 is as-grown GaN:Be and R96 is GaN:Be annealed at 1000 °C). The spectra are red-shifted by 8 meV to compensate for shifts due to biaxial strain in GaN/sapphire layers. The blue, green and black vertical lines indicate ZPLs and their LO-phonon replicas. The red vertical lines show the phonon replicas of the UVL_{Be} (DAP) ZPL associated with the pseudo-local phonon mode (37.5 meV, see Table 3). (**b**) SSPL spectra at T = 18 K from MBE-grown GaN:Be (sample 0408a) annealed in N_2 for one hour at selected temperatures. For T_{ann} = 400 °C, the PL spectrum between 3.2 and 3.4 eV reveals LO phonon replicas of excitonic lines and no trace of the UVL_{Be} band. Reproduced with permission from [64].

Analysis of temperature and excitation-intensity dependences of the DAP and eA components yields the $-/0$ transition levels at 222 meV (Mg_{Ga}) and 114 meV (Be-related defect) at T = 18 K [64]. Due to these low ionization energies, the UVL_{Mg} and UVL_{Be} bands are quenched at relatively low temperatures (above 100 K and 70 K, respectively). Furthermore, it is known that the electron- and hole-capture coefficients generally decrease with increasing ionization energy for acceptors in GaN [34,66]. Consistent with this trend, UVL_{Mg} and UVL_{Be} exhibit the highest C_n (3.2×10^{-12} and 1×10^{-11} cm^3s^{-1}, respectively) and C_p (both about 1×10^{-6} cm^3s^{-1}), see Figure 9.

The differences between the UVL_{Mg} and UVL_{Be} bands offer insights into the origin of the latter. The UVL_{Mg} band is prevalent in undoped n-type GaN due to residual Mg contamination, with its intensity increasing markedly under moderate Mg doping while the material remains n-type [34,62]. In contrast, the UVL_{Be} band is either very weak or absent in conductive n-type GaN:Be samples, regardless of Be concentration, as well as in SI GaN:Be if [Be] < 10^{18} cm^{-3}. In MOCVD-grown GaN, Mg is passivated by hydrogen (with [Mg] ≈ [H]), and Mg_{Ga} activation requires post-growth annealing above 500–600 °C to dissociate Mg-H complexes [218]. In contrast, both UVL_{Be} and YL_{Be} bands are present in as-grown MOCVD GaN:Be (annealing is not required), and [H] does not noticeably increase with Be doping.

On the other hand, in MBE-grown GaN:Be, the UVL_{Be} appears only after annealing at T_{ann} > 700 °C (Figure 32b). At higher annealing temperatures, the RL_{Be} band at 1.8 eV appears (Section 4.2.4), and the YL_{Be} band intensity decreases. The difference between the MOCVD and MBE GaN:Be can be explained as follows. During MOCVD growth in Ga-rich

conditions, mobile species such as V_{Ga} and H are abundant at growth temperatures and promote the formation of Be_{Ga} and $Be_{Ga}O_NBe_{Ga}$ acceptors. In GaN grown by MBE under N-rich conditions, mobile nitrogen vacancies, which act as donors, are abundant and tend to passivate the $Be_{Ga}O_NBe_{Ga}$ acceptors. Post-growth annealing at T = 700–900 °C activates $Be_{Ga}O_NBe_{Ga}$, while the released nitrogen vacancies passivate Be_{Ga} by forming V_NBe_{Ga} complexes, thereby reducing YL_{Be} emission and enhancing RL_{Be} intensities.

First-principles calculations predict that $Be_{Ga}O_NBe_{Ga}$ complex acts as a dual-nature acceptor with shallow and deep levels at 0.12 and 0.34 eV above the VBM, respectively [64]. However, no PL signal could be found from the deep level. One explanation is that the deep level is actually closer to the VBM than the shallow level. Alternatively, the deep state may not participate in electron-hole recombination if a substantial potential barrier exists between the shallow and deep states. Finally, it remains possible that the UVL_{Be} band originates from a distinct Be-containing complex that has not yet been identified.

4.2.4. $Be_{Ga}V_N$-Related RL_{Be} Band

In GaN:Be samples grown by MBE, annealing at $T_{ann} \approx 900$ °C induces a strong RL_{Be} band with a maximum at 1.8 eV (Figure 33a). This band is attributed to transitions involving the $Be_{Ga}V_N$ complex donors [36,150]. In PL spectra from these samples, the V_N-related GL2 band (Section 3.3.2) is also observed. First-principles calculations predict a PL band with a maximum at 1.69 eV for transitions from the CBM to the 0/+ level of the $Be_{Ga}V_N$ complex, which is close to the experimentally determined value of 1.77 eV [36].

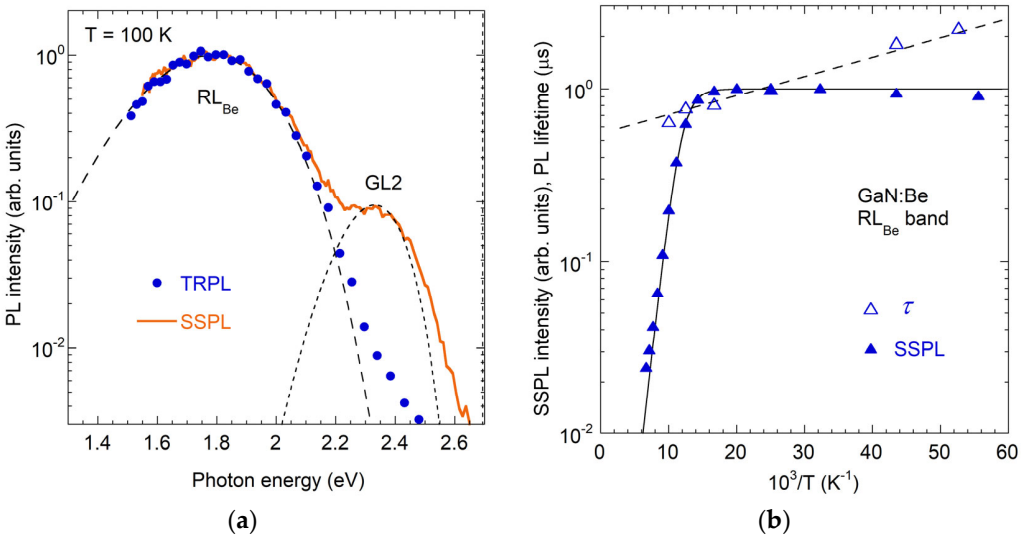

Figure 33. The RL_{Be} band associated with the $Be_{Ga}V_N$ complex in MBE GaN:Be. (**a**) SSPL and TRPL (at 1 μs) spectra. The dashed lines are calculated using Equation (6) with parameters from Table 2. (**b**) $I^{PL}(T)$ and $\tau(T)$ dependences for the RL_{Be} band. The solid line is calculated using Equation (2) with $C = 1.5 \times 10^4$ and E_A = 70 meV, and the dashed line is 0.55·exp(2.5meV/kT).

The SSPL intensity of the RL_{Be} band remains constant up to ~70 K and decreases at higher temperatures, with an activation energy of about 0.1 eV (Figure 33b). In TRPL experiments, exponential decay of RL_{Be} is observed at the lowest temperatures, in line with its attribution to internal transition from an excited state of the deep donor. The PL lifetime of the RL_{Be} decreases from 2 μs at T = 18 K to 1 μs at $T \approx 70$ K (Figure 33b). The PL quenching at $T > 70$ K is explained by thermal emission of electrons from an excited state located at 0.1 eV below the CBM to the conduction band [36]. These $I^{PL}(T)$ and $\tau(T)$ dependences resemble those of the RL2 band in undoped GaN (Section 3.2.2), and the exponential decrease in PL lifetime at $T < 70$ K can be explained by two excited states with

closely spaced levels. However, the slope of the $\tau(T)$ dependence is much smaller, and the separation between the levels is smaller for the $Be_{Ga}V_N$ (2.5 meV) than for the RL2-related defect in undoped GaN (10 meV).

4.2.5. Deep Donor PL (BL_{Be})

At elevated excitation intensities, the YL_{Be} band becomes saturated, and a new band (BL_{Be}) emerges at 2.6 eV (Figure 34). Its shape can be fitted using Equation (6) with parameters from Table 2. The BL_{Be} band is tentatively attributed to transitions via the 0/+ level of the Be_{Ga} defect [61]. When the Fermi level is above the −/0 level of Be_{Ga}, two-hole capture may lead to radiative recombination via the 0/+ level of Be_{Ga}, making BL_{Be} prominent only at high P_{exc}, when the Be_{Ga} defects are saturated with holes. In *p*-type GaN:Be, a significant fraction of the neutral Be_{Ga} defects are expected to be neutral even at low P_{exc}; however, the BL_{Be} intensity remains low. This is likely due to a low hole-capture coefficient for the 0/+ level of Be_{Ga}, similar to what has been observed for the C_N defect (Section 4.1.1).

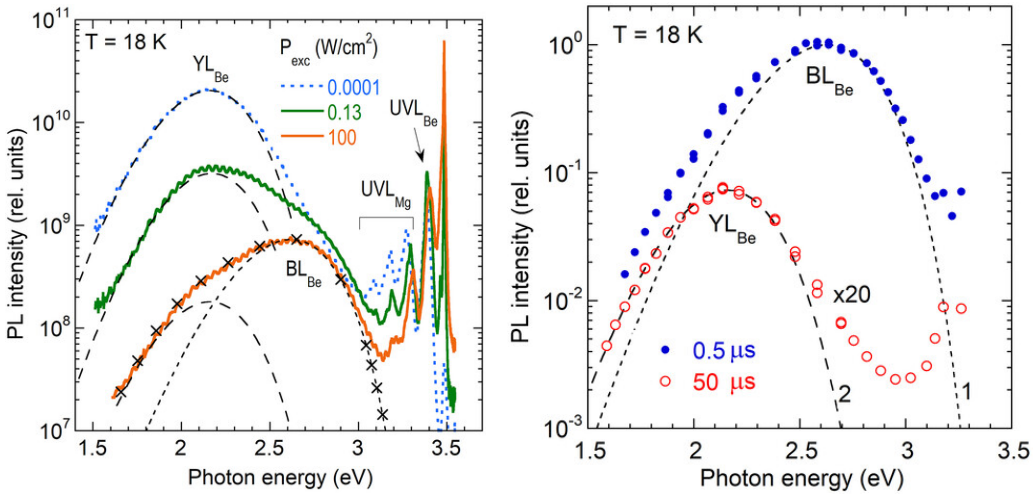

Figure 34. The BL_{Be} band in GaN:Be. (**a**) SSPL spectra at T = 18 K (divided by P_{exc}). Dashed lines are calculated using Equation (6) with parameters from Table 2. The × symbols show the sum of calculated YL_{Be} and BL_{Be} spectra at P_{exc} = 100 Wcm^{-2}. (**b**) TRPL spectra at t = 0.5 μs (filled symbols) and t = 50 μs (empty symbols) at T = 18 K and $P_0 = 5 \times 10^{23}$ cm^{-2}s^{-1}. The data at 50 μs is multiplied by a factor of 20. Dashed lines are calculated using Equation (6) with parameters from Table 2. Reproduced with permission from [61].

After a laser pulse, the BL_{Be} intensity decays exponentially at T = 18 K, with a characteristic lifetime of 0.75 ± 0.15 μs, indicative of an internal transition from an excited state to the ground state [61]. The behavior is typical for deep donors in GaN. The quenching of the BL_{Be} band at T > 100 K is attributed to thermal emission of bound holes to the valence band. Concurrently, the PL lifetime decreases with the same activation energy. From these dependences, the 0/+ level was estimated to lie 0.15 ± 0.05 eV above the VBM, and this value agrees with the position and shape of the BL_{Be} band [61]. Note that hybrid functional calculations for Be_{Ga} in GaN do not find the 0/+ transition level of this defect [61], possibly because of the close location of this level to the VBM.

4.2.6. Other Be-Related Defects

In MOCVD-grown GaN samples, heavily doped with Be, a weak green luminescence (GL_{Be}) band with a maximum at ~2.4 eV may contribute to the high-energy side of the stronger YL_{Be} band. However, this GL_{Be} component remains unresolved in SSPL and

TRPL measurements when the excitation intensity and temperature are varied over wide ranges [61]. This band could be caused by a complex defect containing one or more Be atoms.

$Be_{Ga}O_N$ complexes are expected to form readily in GaN samples containing high concentrations of Be and O, such as bulk GaN crystals grown by the HNPS method with [Be] ≈ [O] ≈ 3×10^{19} cm^{-3} [46,211]. In hydrostatic pressure experiments on such samples, Teisseyre et al. [211] attributed a broad yellow band, which blue-shifted markedly with pressure, to the $Be_{Ga}O_N$ complex. However, as discussed in Section 4.2.2, these results may also be explained by the assumption that the yellow band originated from isolated Be_{Ga}.

Recent PL studies of bulk HNPS GaN:Be,O revealed the Be_{Ga}-related YL_{Be} band and the C_N-related YL1 band, but no distinct emission band could be conclusively assigned to the $Be_{Ga}O_N$ complex [46]. These results were explained by the assumption that the $Be_{Ga}O_N$ complexes, even when they are present with high concentrations (~3×10^{19} cm^{-3}), are either electrically neutral or exhibit poor hole-capture efficiency, such that their emission is overshadowed by stronger YL_{Be} and YL1 bands. Calculations using Heyd-Scuseria-Ernzerhof (HSE) hybrid functional predict that the $Be_{Ga}O_N$ complex is either a deep donor with the 0/+ level at 0.26 eV above the VBM [211], or it is electrically neutral and does not have transition levels in the band gap [150]. Similarly, the $Be_{Ga}H_i$ complex has been predicted to be electrically neutral [219].

4.3. Magnesium-Related Defects (UVL_{Mg}, BL_{Mg}, RL_{Mg})

Magnesium is currently the only impurity reliably used to achieve conductive *p*-type GaN. This section reviews the PL characteristics of Mg-related defects, focusing on the ultraviolet (UVL_{Mg}), blue (BL_{Mg}), and red (RL_{Mg}) luminescence bands. These bands are discussed in terms of spectral features, defect assignments, and theoretical interpretations.

4.3.1. Historical Overview

Maruska et al. [220] were the first to report Mg doping in GaN, for use in m-i-n diodes emitting violet light. PL measurements at 77 K revealed a blue band with a maximum at 2.925 eV, which the authors attributed to an Mg-related defect with a level at ~0.5 eV above the VBM. However, the Mg-doped GaN samples retained their highly resistive nature, and the realization of effective *p*-type conductivity remained elusive for several years. It was not until 1989 that a breakthrough was achieved by the team at Nagoya University, who demonstrated conductive *p*-type GaN through post-growth low-energy electron beam irradiation (LEEBI) treatment of Mg-doped layers [221]. This advance resolved a critical obstacle and ultimately paved the way for the development of bright blue LEDs [222]. Low-temperature (4.2 K) PL spectra from early *p*-type GaN:Mg samples grown by MOCVD showed the UVL_{Mg} band at 3.27 eV (for [Mg] = 1.6×10^{19} cm^{-3}) and a blue band with a maximum at 2.95 eV ([Mg] = 7.1×10^{19} cm^{-3}), both attributed to the Mg acceptor [223,224].

Since then, the Mg-doped GaN has been extensively studied. In particular, it was found that Mg_{Ga} acceptors, passivated by H during MOCVD growth, can be activated not only via LEEBI treatment [221] but also by thermal annealing at temperatures above 500 °C [225,226]. Early studies of MOCVD-grown GaN:Mg, using room-temperature PL, revealed two PL bands: blue and red [226]. The red band was observed in as-grown, high-resistivity GaN:Mg samples and attributed to Mg-H complexes. The blue band was initially assigned to Mg levels [226]. Later, compelling evidence supported the deep DAP nature of transitions, involving a deep donor and the shallow Mg_{Ga} acceptor [63,227,228]. The identity of the deep donor remains uncertain (Section 4.3.3).

Conductive *p*-type GaN can also be achieved without post-growth annealing by MBE technique [169,229,230]. Such samples exhibit the UVL_{Mg} band with a maximum at about

3.27 eV (Section 4.3.2). The BL_{Mg} band at ~2.9 eV is typically observed in GaN grown by MOCVD heavily doped with Mg and less often in HVPE GaN:Mg (Section 4.3.3). Mg-doped GaN often exhibits the V_N-related GL2 band (Section 3.3.2) and the RL_{Mg} band (Section 4.3.5).

4.3.2. Shallow or Dual-Nature Acceptor?

Lany and Zunger [206] proposed that Mg_{Ga} is a dual-nature acceptor. A shallow level with a delocalized hole was predicted at 0.18 eV, and a deep level with a localized hole is calculated at 0.21 eV above the VBM. Transitions of electrons via the shallow level produce the UVL_{Mg} band, whereas the BL_{Mg} band was hypothesized to arise from the deep level. According to this model, at room temperature and in the dark, holes predominantly populate the deep level, which is therefore responsible for *p*-type conductivity [206]. Several theoretical studies supported this dual nature [231,232], though others identify only the deep state [233,234]. In particular, Lyons et al. [233] proposed that the Mg_{Ga} with the calculated deep level at 0.26 eV is responsible for the blue band with a maximum at 2.7 eV, while the UVL_{Mg} band is caused by the $Mg_{Ga}H_i$ complexes with the 0/+ level at 0.13 eV above the VBM.

PL experiments consistently identify only the shallow Mg_{Ga} level producing the UVL_{Mg} band (Figure 35).

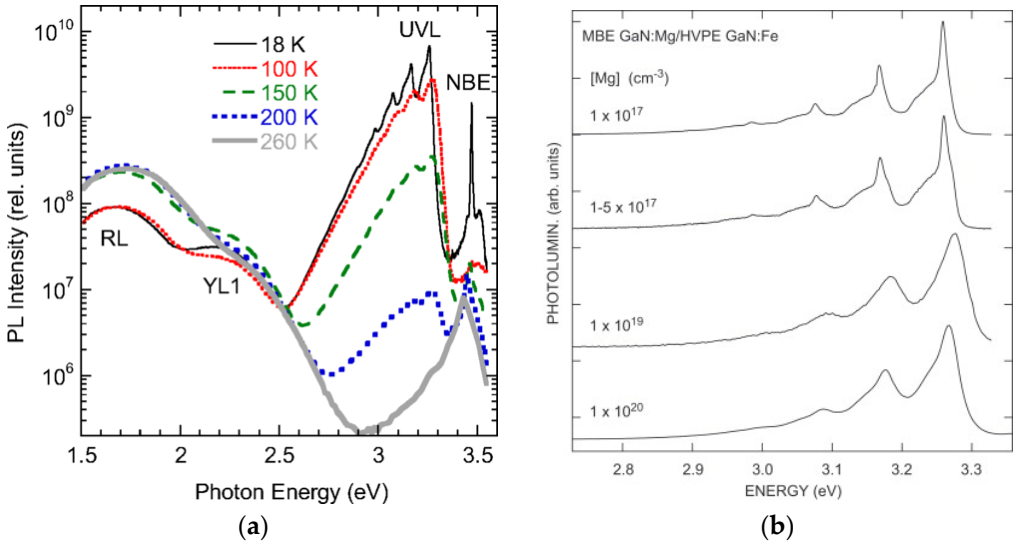

Figure 35. The UVL_{Mg} band in Mg-doped GaN. (**a**) Evolution of the PL spectrum with temperature for *n*-type GaN:Mg ([Mg] = 1.3×10^{17} cm^{-3}) grown by HVPE. Reproduced with permission from [62]. (**b**) PL spectra at $T = 2$ K for *p*-type GaN:Mg samples grown by MBE. Reproduced with permission from [169].

The BL_{Mg} band, observed in heavily Mg-doped MOCVD-grown samples, cannot be attributed to the predicted deep-state of Mg_{Ga}. Indeed, PL intensities from shallow and deep states of dual-nature acceptors must correlate [45]. In particular, their relative contribution may vary with temperature according to the Boltzmann occupation of levels with holes, but the ratio should remain consistent across samples, as it was observed for Be_{Ga} (Section 4.2.2). However, in *n*-type GaN:Mg and in MBE-grown *p*-type GaN:Mg, only the UVL_{Mg} band is found (Figure 35). If Mg_{Ga} is a dual-nature acceptor, the absence of deep-level PL suggests either identical transition energies for both states or a substantial potential barrier separating them [45,235].

Heavily Mg-doped GaN contains a variety of defects that affect PL. The analysis of PL is complicated by the fact that even *p*-type GaN:Mg becomes semi-insulating at low

temperatures due to an insufficiently shallow Mg_{Ga} level. In such material, potential fluctuations due to nonuniform distribution of charged defects or local electric fields associated with structural defects may lead to unstable PL [236–238], significant shifts and broadening of PL bands (Section 4.3.4). PL results from GaN:Mg are often difficult to reproduce, and misinterpretations are common.

Pozina et al. [239] initially proposed that two distinct Mg-related acceptors exist in GaN: A1 is responsible for the UVL_{Mg} band at 3.27 eV, and A2 is responsible for a broader band at 3.15 eV. However, later these researchers attributed only the 3.27 eV peak to the isolated Mg_{Ga} acceptor, whereas the 3.15 eV band was explained as PL from Mg_{Ga} perturbed by a nearby basal plane stacking fault [165].

Callsen et al. [240] proposed that the UVL_{Mg} band consists of three components related to three acceptor states, with levels E_A = 164, 176, and 195 meV. In their opinion, these results supported the dual nature of the Mg_{Ga} acceptor proposed earlier [206]. However, these components were not clearly resolved, and variations in the UVL_{Mg} peak position across samples are more plausibly explained by donor variability, strain or local electric fields. Even if the proposed states are real, they all look like shallow states with delocalized holes, distinct from the broad blue band expected for the deep Mg_{Ga} state [206,233].

4.3.3. BL_{Mg} Band in Heavily Doped GaN:Mg

The BL_{Mg} band, peaking between 2.7 and ~3.0 eV, is commonly observed in MOCVD-grown GaN when Mg concentrations exceed ~10^{18} cm^{-3} [16,226,241]. This band exhibits a pronounced blue shift with increasing excitation intensity in SSPL and a red shift with time delay in TRPL (Figure 36). Such behavior is characteristic of deep DAP transitions, specifically involving deep donors and shallow Mg_{Ga} acceptors [63,227,228].

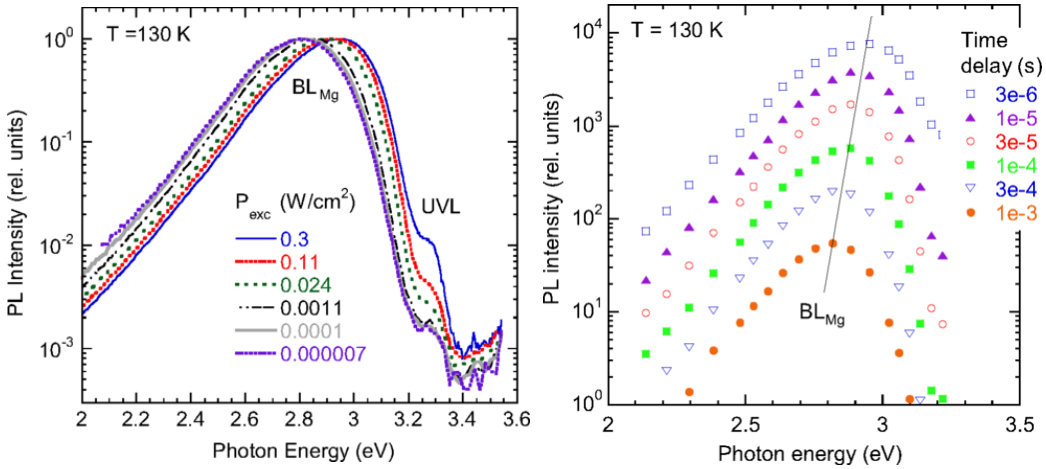

Figure 36. The BL_{Mg} band at 130 K in Mg-doped *p*-type GaN ([Mg] = 2 × 10^{19} cm^{-3}) grown by HVPE. (**a**) Normalized SSPL spectra at selected excitation intensities. (**b**) Evolution of the TRPL spectrum after a laser pulse. Reproduced with permission from [62].

In contrast, DAP transitions, involving shallow donors (Si_{Ga} or O_N) and various acceptors in GaN, show only minor spectral shifts (<10 meV) [66]. The large shifts observed for deep DAPs are attributed to the strongly localized nature of the carrier wavefunctions [63,242]. For deep donors with energy levels 0.4–0.6 eV below the CBM, the electron wavefunction is highly confined. In such cases, tunneling to nearby Mg_{Ga} acceptors is efficient only at high acceptor concentrations (>10^{18} cm^{-3}). Strong Coulomb interactions between closely spaced DAPs result in a broad distribution of recombination energies, thereby explaining the substantial spectral shifts observed in both SSPL and TRPL.

The BL_{Mg} band is notably absent in GaN implanted with Mg, even for Mg concentrations above 10^{19} cm^{-3} [243–247], and also in samples co-implanted with Mg and H ions [248]. It is rarely observed in HVPE-grown GaN:Mg [62,249] and is absent in MBE-grown *p*-type GaN:Mg [169,229,230]. The specific conditions in MOCVD, particularly the abundance of hydrogen, likely facilitate the formation of the responsible deep donor. In particular, Kamiura et al. [250] reported an enhanced BL band in MOCVD-grown GaN:Mg ([Mg] $\approx 1 \times 10^{20}$ cm^{-3}) after hydrogen plasma treatment. The V_NH complex has been proposed as the associated deep donor [165,251,252]. Alternatively, Mg interstitial (Mg_i) and Mg-related donors such as $Mg_{Ga}Mg_i$ have been suggested by first-principles calculations [47,234,253]. Although earlier reports proposed the V_NMg_{Ga} complex as the deep donor associated with BL_{Mg} [227], it is now more reliably attributed to the RL_{Mg} band [36,254] (Section 4.3.5). It is important to note that distinguishing PL bands in Mg-doped GaN, particularly UVL_{Mg} and BL_{Mg}, can be challenging, as their spectral positions and shapes are sensitive to experimental conditions in SI samples (Section 4.3.4).

4.3.4. Giant Shifts in PL Bands in GaN:Mg

Large spectral shifts in PL bands can result not only from deep DAP transitions but also from screening with photogenerated carriers of potential fluctuations or local electric fields [63,242,255]. This is more typical for SI materials with nonuniformly distributed charged impurities. Diagonal tunnel transitions with reduced energies dominate in PL from a sample with potential fluctuations. The transition energy increases with increasing P_{exc} (as photogenerated carriers partly screen potential fluctuations), and it eventually becomes equal to the energy in an ideal semiconductor. An example is shown in Figure 37. The UVL_{Mg} band (labeled UVL*) redshifts by up to 0.4 eV with decreasing P_{exc}. Interestingly, the shifting UVL* band coexists with the stable UVL_{Mg} at 3.27 eV (Figure 37a). The UVL* band in this case likely originates from a near-surface layer, where band bending may remain significant even at low temperatures (despite being screened by photogenerated charge carriers), whereas stable UVL_{Mg} arises from bulk regions [62].

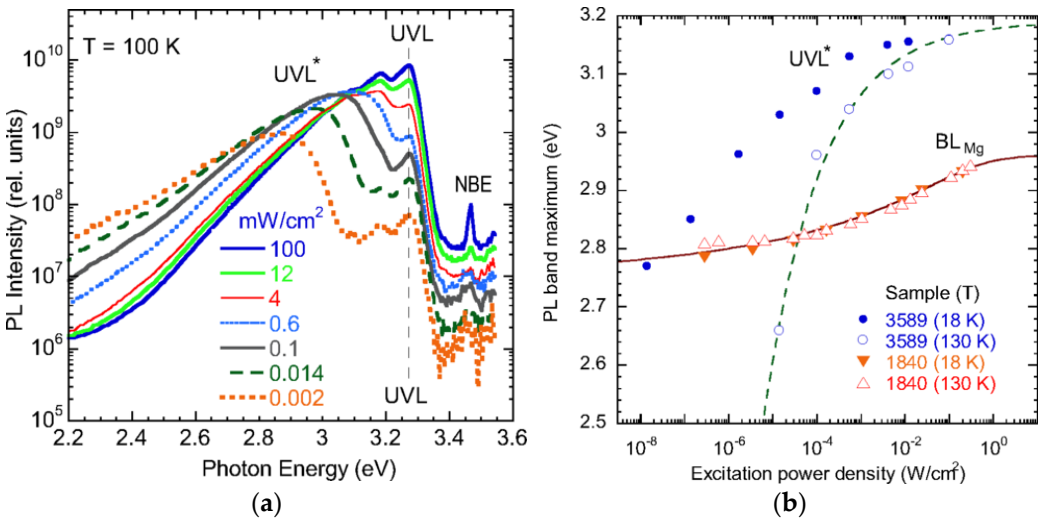

Figure 37. Excitation-induced shifts in PL bands in HVPE-grown GaN:Mg (**a**) PL spectra from SI GaN:Mg at T = 100 K and selected excitation power densities. PL intensity is normalized by P_{exc}. The UVL band does not shift, while the UVL* band shifts monotonously to lower energies with decreasing P_{exc}. (**b**) Shift in PL band maxima with excitation intensity at T = 18 and 130 K. The BL_{Mg} band in *p*-type GaN:Mg (sample 1840) and the UVL* band in SI GaN:Mg (sample 3589). Reproduced with permission from [62].

Distinguishing between energy shifts caused by deep DAP nature and those due to the electric-field mechanism is not straightforward. In both cases, a PL band blue-shifts with increasing P_{exc} and redshifts with time delay after a laser pulse. Nevertheless, there are important differences. For DAP transitions, the total shift is typically limited by the ionization energy of the shallower component [84,158,242]. Shallow DAP shifts are small (<10 meV for a variety of acceptors in *n*-type GaN [16,62,66]), whereas the BL_{Mg} shifts are large, but still limited by the Mg_{Ga} ionization energy (0.2 eV). In Figure 37b, the BL_{Mg} band shift is fitted with a DAP model [158], where the ionization energies of the deep donor and shallow Mg_{Ga} acceptor are 0.4 and 0.2 eV, respectively. The total shift in the BL_{Mg} band in a very wide range of P_{exc} does not exceed 0.2 eV. On the other hand, shifts due to potential fluctuations or local electric fields may reach magnitudes comparable to the bandgap [242]. In Figure 37b, the UVL_{Mg} band redshifts by ~0.5 eV with decreasing P_{exc}, and the trend does not show any saturation.

4.3.5. $Mg_{Ga}V_N$-Related RL_{Mg} Band

The RL_{Mg} band, peaking at 1.6–1.7 eV, is occasionally observed in Mg-doped GaN (Figure 38). It has been attributed to the $Mg_{Ga}V_N$ complex [36,254] and often appears alongside the V_N-related GL2 band. ODMR studies of MOCVD-grown Mg-doped GaN revealed a sharp and isotropic signal with a g factor of 2.003 ± 0.003 associated with the RL_{Mg} band [256].

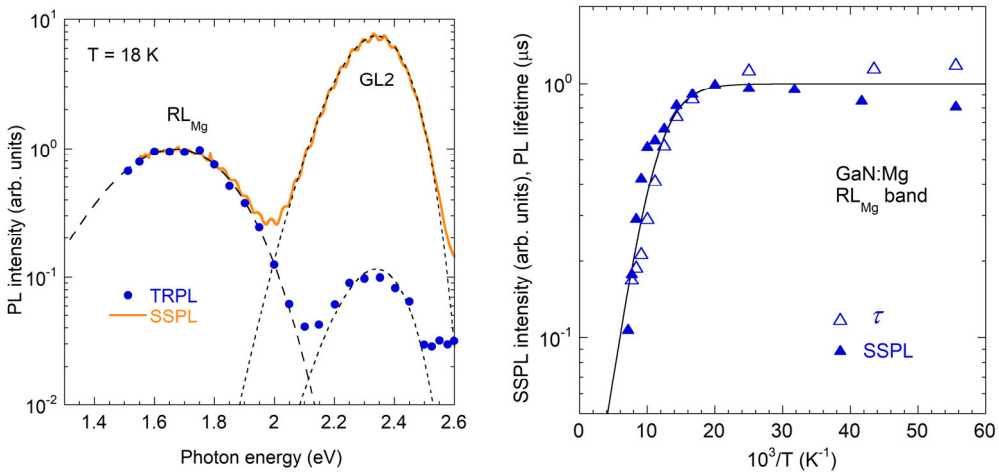

Figure 38. The RL_{Mg} band in MBE-grown GaN:Mg. (**a**) Comparison of normalized SSPL and TRPL spectra (time delay is 1 μs). Dashed lines are calculated using Equation (6) with parameters from Table 2. (**b**) Temperature dependence of SSPL intensity and PL lifetime. The line is calculated using Equation (2) with C = 100 and E_A = 35 meV.

PL studies indicate that the RL_{Mg} band, with a maximum at 1.68 eV at T = 18 K, originates from electron transitions between an excited state located near the CBM and the ground state ~0.8 eV above the VBM [36]. The PL decay is exponential at T < 50 K, with a lifetime of about 1 μs (Figure 38b). At T > 70 K, both PL intensity and PL lifetime decrease due to the thermal emission of electrons from the excited state to the conduction band. The extracted activation energy of 35 meV corresponds to the energy separation between the excited state and the CBM.

According to first-principles calculations, the $Mg_{Ga}V_N$ defect has the +/2+ and 0/+ levels ~0.8 eV above the VBM [36,234,254], with the +/2+ level possibly 50 meV higher (negative U behavior) [254]. Optical transitions from the CBM to the +/2+ and 0/+ levels are predicted to produce two red PL bands with maxima at 1.83 and 1.81 eV, respectively [254].

When the Fermi level (F) lies above ~0.8 eV, the $Mg_{Ga}V_N$ defects are predominantly neutral under dark conditions or at low P_{exc}. In this case, hole capture at the 0/+ level, followed by electron capture into the excited state, leads to an internal transition that produces a red PL band (RL_{Mg1}). In conductive n-type GaN:Mg samples (overcompensated by shallow donors), the RL_{Mg1} intensity is expected to be significantly lower than the UVL_{Mg} intensity, by a factor $N^{RL}{C_p}^{RL}/N^{UVL}{C_p}^{UVL}$, where N and C_p are the concentrations and hole-capture coefficients for defects responsible for the RL_{Mg1} and UVL_{Mg} bands.

In conductive p-type GaN:Mg samples ($F \approx 0.2$ eV), the $Mg_{Ga}V_N$ defects are in the 2+ charge state in the dark, and transitions via the +/2+ level can produce another red PL band (RL_{Mg2}). In such samples, an electron must first be captured by the excited state, after which a hole is captured at the +/2+ level; their recombination then produces RL_{Mg2}. This mechanism is similar to the one suggested for the V_N-related GL2 band (Section 3.3.2).

Although theoretical predictions suggest two distinct red PL bands associated with the 0/+ and +/2+ transition levels in Mg-doped GaN, experimental validation is still lacking. The RL_{Mg} band with $\hbar\omega_{max} = 1.68$ eV and $\tau_0 = 1$ µs (Figure 38) is likely caused by transitions via the 0/+ level (RL_{Mg1}) in SI GaN:Mg because the GL2 band is also observed. According to limited experimental reports, a weak red band is observed in conductive p-type GaN, sometimes together with the GL2 band [47,257]. Note that GaN:Mg samples may be nonuniform, with conductive p-type and SI regions [47]. In such samples, p-type conductivity can be confirmed by the Hall effect, while the PL response may predominantly arise from SI regions.

The red band reported by Nakamura et al. [225,226] in GaN:Mg may differ from RL_{Mg1} and RL_{Mg2}, as it was observed at room temperature in SI GaN:Mg and was absent in conductive p-type samples. Bayer et al. [258,259] observed a weak red band at $T = 5$ K in MOCVD-grown p-type GaN:Mg, but they did not provide its temperature dependence. In our measurements, a weak red band consistent with RL_{Mg1} was detected at $T = 18$ K in MBE-grown GaN:Mg. At room temperature, it could not be resolved (completely quenched), whereas the UVL_{Mg} band remained strong [47]. The quenching of that RL_{Mg} band with an activation energy of ~0.1 eV is attributed to electron thermal escape from the excited state to the conduction band [36].

4.4. Zinc (BL_{Zn})

The Zn_{Ga} acceptor, with the $-/0$ level at 0.40 eV above the VBM, efficiently captures photogenerated holes, producing the BL1 band in undoped GaN contaminated with Zn (Section 3.4.1). In Zn-doped GaN, this band, referred to as BL_{Zn}, is the dominant defect-related PL feature.

4.4.1. BL_{Zn} Band in Zn-Doped GaN

The BL_{Zn} band exhibits ZPL at 3.10 eV, followed by phonon replicas (Figures 18a and 39a). At $T < 50$ K, the band arises from DAP transitions involving shallow donors and Zn_{Ga} acceptors. At higher temperatures, e-A transitions dominate thanks to thermal emission of electrons from shallow donors to the conduction band. In Zn-doped GaN, BL_{Zn} is the strongest defect-related band (Figure 39a). In the NBE region, excitons bound to neutral Zn_{Ga} acceptors (ZnX_A) are resolved. Zn-doped GaN samples are typically semi-insulating, although p-type conductivity is occasionally confirmed [260].

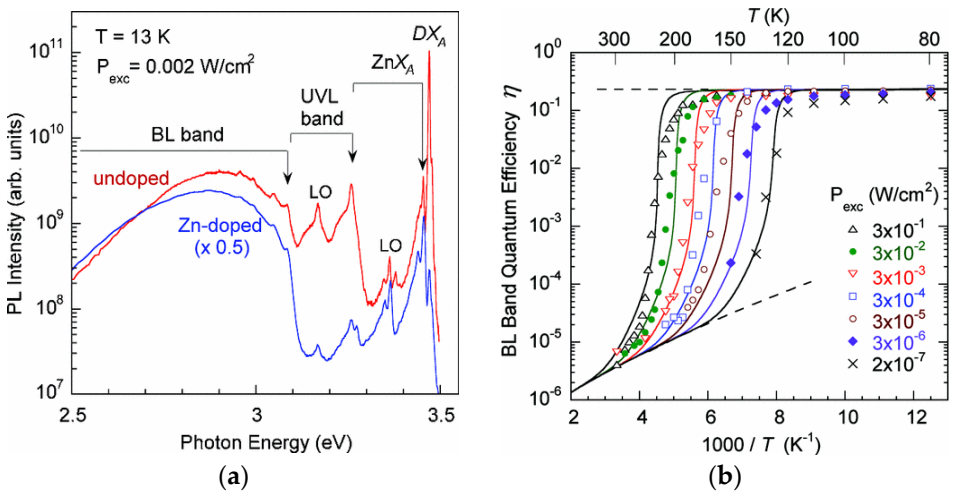

Figure 39. The BL_{Zn} band in Zn-doped GaN. (**a**) PL spectra from undoped GaN and Zn-doped GaN at T =13 K (not multiplied by λ^3). Arrows indicate the ZPLs for the BL_{Zn} and UVL_{Mg} bands, as well as the ZnX_A exciton. (**b**) Tunable and abrupt quenching of the BL_{Zn} band in high-resistivity Zn-doped GaN for excitation power densities P_{exc} between 2×10^{-7} and 0.3 W cm^{-2}. Solid curves represent numerical solutions of rate equations. Reproduced with permission from [52].

4.4.2. Tunable and Abrupt Quenching

The BL_{Zn} band in SI and *p*-type GaN:Zn displays remarkable features, such as quenching by the TAQ mechanism, two-step quenching, and strongly superlinear dependence on excitation intensity [52,261,262]. The BL_{Zn} quenching occurs at a critical temperature T_0, which increases with excitation intensity (Figure 39b). The quenching is abrupt, with a slope much larger than any reasonable activation energy. The TAQ is explained by a transition from an inverse carrier population regime at $T < T_0$ to an equilibrium population regime (*p*-type or SI) at $T > T_0$. At low temperatures, photogenerated electrons and holes rapidly populate donors and acceptors, respectively, saturating nonradiative deep donors with electrons, even at very low excitation intensities. This suppresses nonradiative recombination, enabling efficient radiative recombination. Under SSPL conditions, the concentration of electrons in the conduction band can greatly exceed the concentration of holes in the valence band (photo-induced *n*-type conductivity). With increasing temperature, holes from acceptors are thermally emitted to the valence band. At $T \approx T_0$, the excess of these thermal holes over photogenerated holes unblocks nonradiative recombination channels, causing an abrupt reduction in radiative recombination efficiency, including the BL_{Zn} and NBE emissions. Since the concentration of photogenerated holes is proportional to the excitation intensity, a higher temperature T_0 is needed at higher P_{exc} to activate nonradiative recombination channels. Figure 39b shows the $I^{PL}(T)$ dependences and their fit with numerical solutions of rate equations for a *p*-type semiconductor with three types of defects: shallow donors D, radiative acceptors A (Zn_{Ga}), and unknown nonradiative donors S.

4.4.3. Two-Step Quenching

When two acceptor species with comparable concentrations coexist, two-step quenching by the TAQ mechanism is possible [261]. An example is shown in Figure 40a for a Zn-doped GaN sample contaminated with Mg. The first quenching step at T_1 occurs due to hole emission from the Mg_{Ga} acceptor (E_A = 0.2 eV) to the valence band, partially unblocking the nonradiative channel. An abrupt drop at T_2 (the second step) is caused by thermal emission of holes from the Zn_{Ga} acceptor (E_A = 0.4 eV) to the valence band and complete activation of the nonradiative channel. Both T_1 and T_2 are tunable with P_{exc}.

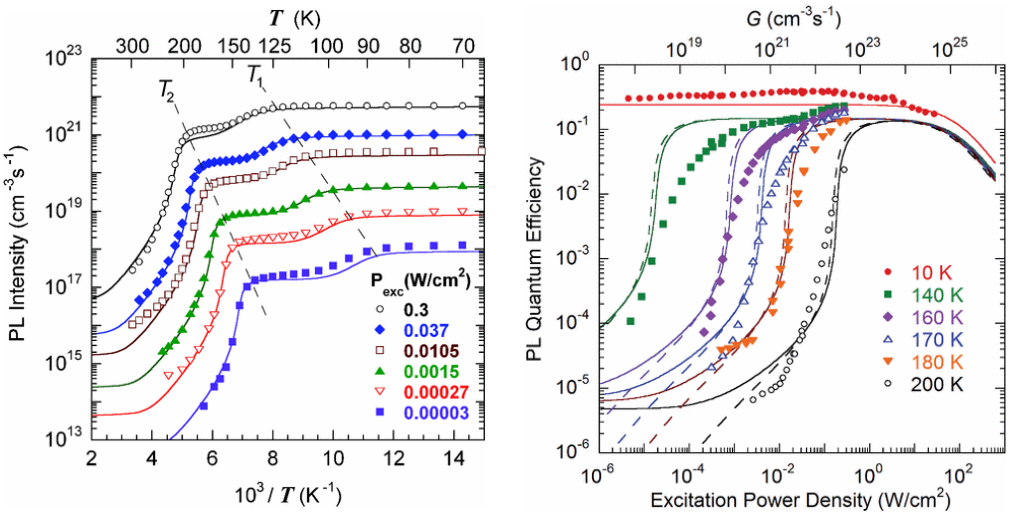

(**a**) (**b**)

Figure 40. Tunable and abrupt quenching of the BL_{Zn} band in GaN. (**a**) Temperature dependence of BL_{Zn} intensity at selected excitation intensities for Zn-doped GaN unintentionally contaminated with Mg. Solid curves represent numerical solutions of rate equations. Reproduced with permission from [261]. (**b**) Dependence of the BL_{Zn} quantum efficiency on excitation power density at selected temperatures in high-resistivity GaN:Zn. Solid and dashed curves are calculated for *p*-type and *n*-type, respectively. Reproduced with permission from [262].

4.4.4. Superlinear Excitation Intensity Dependence

The excitation intensity dependences in samples exhibiting the TAQ mechanism demonstrate strongly superlinear behavior [262]. Figure 40b shows the quantum efficiency of the BL_{Zn} band at selected temperatures. In contrast to a linear $I^{PL}(P_{exc})$ dependence in conductive *n*-type GaN samples, PL intensity sharply increases at a critical P_{exc}, which itself increases with temperature. The TAQ and superlinear rise in PL intensity represent two aspects of the same underlying mechanism: the suppression or reactivation of nonradiative recombination channels as a function of carrier population dynamics.

4.4.5. Other PL Bands in Zn-Doped GaN

Early studies of Zn-doped GaN reported, in addition to BL_{Zn} at 2.87 eV, three other PL bands (at 2.6, 2.2, and 1.8 eV), attributed to Zn-related defects [263,264]. The 2.6 eV band appeared as a shoulder on the low-energy side of the BL_{Zn} band and is likely the BL_{Zn} band red-shifted due to local electric fields (shifts by up to 0.2 eV were observed for other PL bands with increasing P_{exc} in [263]). Note that the BL_{Zn} band may red-shift by up to 0.8 eV with decreasing P_{exc} in SI GaN:Zn and could be confused with other PL bands [54]. The 2.2 eV band is most likely the YL1 band, caused by carbon contamination. The band at 1.8 eV aligns with predictions from first-principles calculations for the $Zn_{Ga}V_N$ complex [36]. A similar PL band with a maximum at 1.8 eV has also been observed in Zn-doped GaN grown by HVPE [36]. However, careful analysis of SSPL and TRPL indicated that it is the RL3 band, likely caused by contamination with Fe (Section 3.2.3). It is also probable that the $Zn_{Ga}V_N$ complex is a nonradiative defect [265]. Thus, BL_{Zn} with a maximum at ~2.9 eV is the only PL band in GaN that can be reliably attributed to Zn.

4.5. Cadmium (BL_{Cd})

The Cd_{Ga} acceptor, with the −/0 level at 0.55 eV above the VBM [48,59,266], produces the blue (BL_{Cd}) band with a maximum at 2.7 eV (Figure 41a). Lagerstedt and Monemar [59] observed a ZPL at 2.937 eV at T = 1.6 K, followed by phonon replicas. Assuming that this ZPL originates from DAP transitions involving shallow donors and Cd_{Ga} acceptors,

the Cd_{Ga} acceptor ionization energy was estimated to be E_A = 0.55 eV [48], consistent with earlier assessments [266]. In conductive *n*-type GaN:Cd (overcompensated with Si_{Ga} donors), the BL_{Cd} band quenches at T > 310 K (Figure 41b). The quenching can be fitted using Equation (2) with E_A = 0.435 eV, a value slightly lower than the low-temperature spectroscopic value of 0.55 eV [48,59,266].

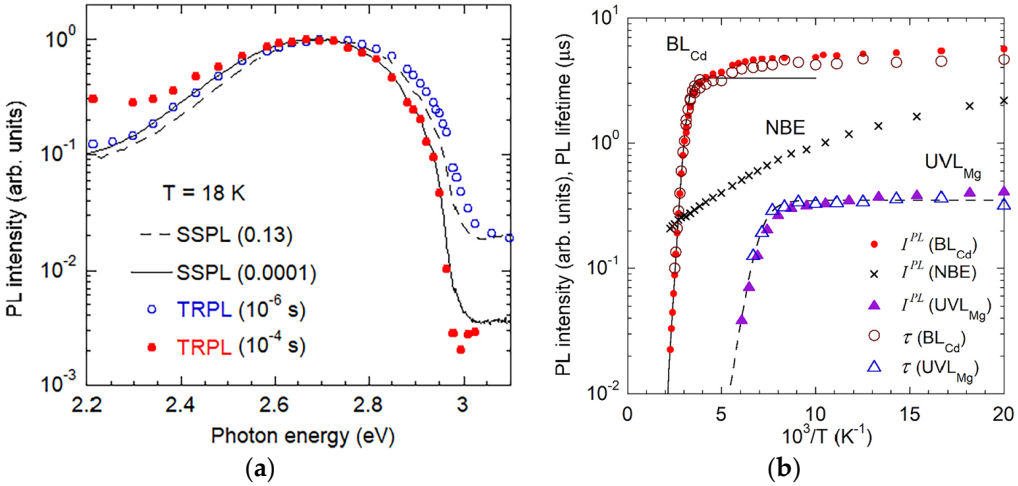

Figure 41. Cd_{Ga}-related BL_{Cd} band. (**a**) Normalized SSPL (at selected P_{exc}) and TRPL (at selected delay times) spectra for GaN:Cd at T = 18 K. Dashed and solid lines correspond to P_{exc} = 0.13 Wcm^{-2} and 10^{-4} Wcm^{-2}, respectively. (**b**) Temperature dependences of SSPL intensity and PL lifetime of the BL_{Cd}, NBE, and UVL_{Mg} bands in Cd-implanted *n*-type GaN annealed at 1100 °C. Solid lines are calculated using Equation (2) with the following parameters: $\tau_0 = 3 \times 10^{-6}$ s, $C_p = 3 \times 10^{-7}$ cm^3s^{-1}, and E_A = 435 meV (BL_{Cd}); $\tau_0 = 3.5 \times 10^{-7}$ s, $C_p = 1 \times 10^{-6}$ cm^3s^{-1}, and E_A = 170 meV (UVL_{Mg}). Reproduced from [48].

The electron- and hole-capture coefficients for the Cd_{Ga} acceptor have been estimated from TRPL and SSPL analyses to be $C_n = 2.6 \times 10^{-13}$ and $C_p = 3 \times 10^{-7}$ cm^3s^{-1}, respectively [48]. The PL properties of Cd_{Ga} resemble those of Zn_{Ga} [48,59,266]. The attribution of the BL_{Cd} band to Cd has also been confirmed via PL experiments involving radioactive isotopes [267,268]. In these experiments, the decay of the ^{111}Ag isotope to ^{111}Cd (half-life = 7.6 days) correlated with the emergence of the BL_{Cd} band at the same temporal rate.

First-principles calculations using HSE hybrid functional, parametrized to fulfill the generalized Koopmans' conditions, predict a ZPL at 3.0 eV and a band maximum at 2.57 eV, in close agreement with experimental observations [235]. Additionally, these calculations predict a yellow band at 2.12 eV, attributed to electron transitions from the CBM (or an excited state close to it) to the 0/+ level of the $Cd_{Ga}V_N$ complex. However, this band has not been observed experimentally [48].

4.6. Calcium (GL_{Ca}, RL_{Ca})

The Ca_{Ga} is a deep acceptor in GaN, with the −/0 level at 0.50 ± 0.02 eV above the VBM [49]. It causes the green luminescence band (GL_{Ca}) with a maximum at 2.5 eV [49,87,269]. In the presence of nitrogen vacancies, $Ca_{Ga}V_N$ complexes form, producing a red luminescence (RL_{Ca}) band with a maximum at 1.82 eV [36]. The properties of both bands are reviewed below.

4.6.1. Ca_{Ga}-Related GL_{Ca} Band

The GL_{Ca} band is typically observed in GaN implanted with Ca [49,87,269], although it may also appear in undoped GaN grown at low temperatures due to unintentional

contamination with Ca [49]. The PL band is broad and structureless, and its shape can be modeled using Equation (6) with parameters listed in Table 2 (Figure 42a).

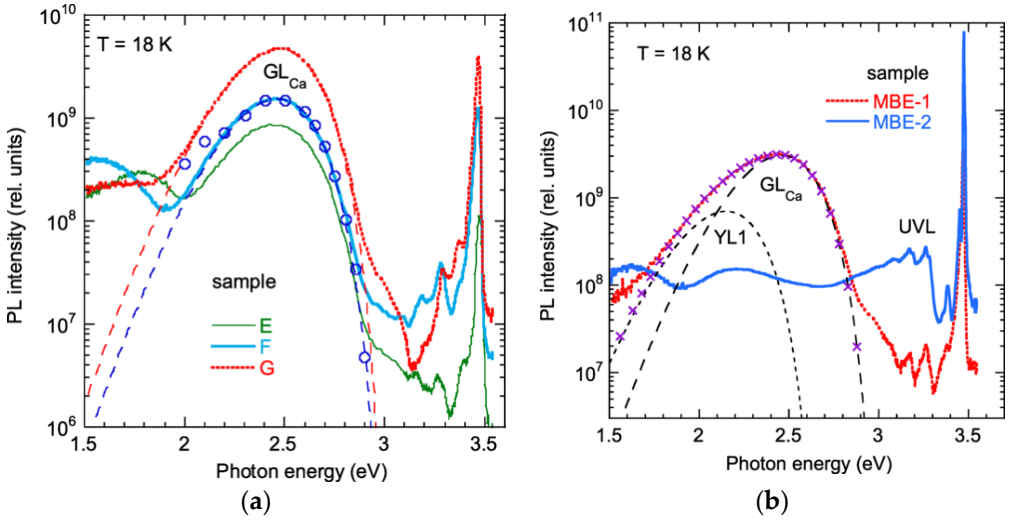

Figure 42. Ca_{Ga}-related GL_{Ca} band. (**a**) PL spectra from *n*-type GaN samples implanted with Ca. Dashed lines are calculated using Equation (6) with parameters from Table 2. Circles show the TRPL spectrum for sample F at 20 μs delay (shifted vertically to align with the SSPL). (**b**) PL spectra from undoped MBE GaN samples. Dashed lines are calculated using Equation (6) with parameters from Table 2. The × symbols show the sum of the two calculated curves. Reproduced with permission from [49].

HSE hybrid functional calculations, tuned to satisfy the generalized Koopmans' condition, accurately reproduce the GL_{Ca} band features [235]. In particular, they predict $\hbar\omega_{max}$ and ZPL at 2.53 eV and 3.08 eV, closely matching the experimental values of $\hbar\omega_{max}$ = 2.5 eV and E_0 = 3.0 eV. Note that other HSE parametrizations yield poorer agreement, predicting: $\hbar\omega_{max}$ = 2.23 eV and E_0 = 2.80 eV [49], or $\hbar\omega_{max}$ = 2.07 eV and E_0 = 2.49 eV [270,271].

In SI GaN:Ca samples, the quenching of the GL_{Ca} band by the TAQ mechanism is observed at $T > 200$ K [49]. In *n*-type GaN:Ca samples, the GL_{Ca} quenching occurs by the Schön–Klasens mechanism [74]. The following parameters of the Ca_{Ga} acceptor have been determined from SSPL and TRPL dependences: $E_A = 0.49 \pm 0.01$ eV, $C_p = (6 \pm 2) \times 10^{-7}$ cm^{3}s^{-1}, and $C_n = (9.5 \pm 2) \times 10^{-14}$ cm^{3}s^{-1} [49].

4.6.2. GL_{Ca} Band in Undoped GaN

The GL_{Ca} band was also found in undoped GaN grown by MBE on freestanding GaN substrates (Figure 42b). It was originally referred to as the aquamarine luminescence (AL) band [153]. Young et al. [155] demonstrated that undoped GaN samples grown by the MBE method may contain Ca concentrations as high as 10^{18} cm^{-3}. From the analysis of excitation intensity dependences, the concentrations of Ca_{Ga} defects in MBE GaN samples analyzed in [49,153] (Figure 42b) were estimated to be 2×10^{16} cm^{-3} (MBE-1) and 6×10^{14} cm^{-3} (MBE-2). The GL_{Ca} band is strong even for low concentrations of Ca because the Ca_{Ga} acceptors efficiently capture photogenerated holes.

4.6.3. $Ca_{Ga}V_N$-Related RL_{Ca} Band

In SI GaN samples implanted with Ca, the RL_{Ca} and GL2 bands are observed at 1.82 and 2.33 eV, respectively (Figure 43a). The GL2 band originates from isolated V_N (Section 3.3.2), while the RL_{Ca} band is attributed to the $Ca_{Ga}V_N$ complex [36,49]. The RL_{Ca} band arises from electron transitions between an excited state located 0.25 ± 0.05 eV below the CBM and the 0/+ level of the $Ca_{Ga}V_N$ donor, which lies at about 1 eV above the

VBM [36]. The PL decay after a laser pulse is exponential, with $\tau \approx 2$ ms at $T = 18$–160 K. This PL lifetime is three orders of magnitude longer than for other AV_N complexes (A = Be_{Ga} and Mg_{Ga}), suggesting a forbidden transition. At higher temperatures, the RL_{Ca} intensity and its lifetime decrease with an activation energy of about 0.25 eV (Figure 43b). The PL quenching is explained by thermal emission of electrons from the excited state to the conduction band, followed by capture by nonradiative defects.

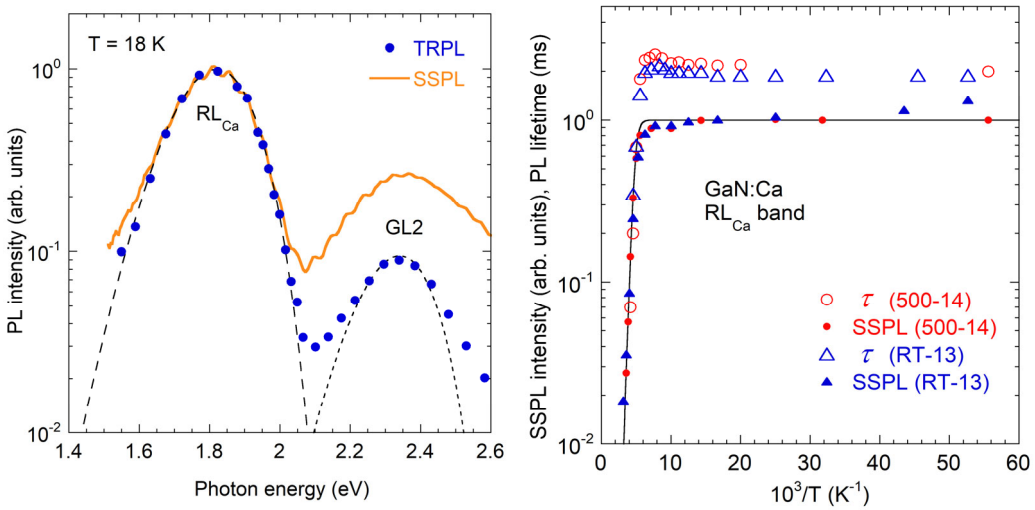

Figure 43. $Ca_{Ga}V_N$-related RL_{Ca} band in GaN implanted with Ca. (**a**) Comparison of normalized SSPL and TRPL (time delay is 1 ms) spectra. Dashed lines are calculated using Equation (6) with parameters from Table 2. (**b**) Temperature dependence of SSPL intensity and PL lifetime for the RL_{Ca} band in two GaN:Ca samples (implanted at room temperature and at 500 °C). The line is calculated using Equation (2) with $C = 10^6$ and $E_A = 250$ meV.

In contrast to other AV_N complexes (Section 3.2.2, Section 4.2.4, and Section 4.3.5), but similar to isolated V_N (Section 3.3.2), the RL_{Ca} band is relatively narrow ($W_0 = 0.25$ eV). First-principles calculations, using the HSE hybrid functional tuned to fulfill the generalized Koopmans' condition [36], disagree with the experimental results. Specifically, the $Ca_{Ga}V_N$-related PL band is predicted to be broad ($W_0 \approx 0.48$ eV), and the calculated optical transition level is expected at 1.47 eV below the CBM, whereas the experimental value (after correcting for the excited state location) is 2.07 eV.

4.7. Mercury (GL_{Hg})

The Hg_{Ga} acceptor is responsible for the green luminescence (GL_{Hg}) band with a maximum at ~2.5 eV [87,267,272] or, more precisely, at 2.44 eV (Figure 44a) [48]. A sharp intensity drop at 2.73 eV (marked by an arrow in Figure 44a) is attributed to the GL_{Hg} band ZPL [48]. Based on this assignment, the $-/0$ level of Hg_{Ga} is estimated at 0.77 eV above the VBM. From the GL_{Hg} band quenching at $T > 500$ K (Figure 44b), $E_A = 0.62$–70 eV and $C_p = (1–5) \times 10^{-7}$ cm^{3}s^{-1} have been determined for the Hg_{Ga} acceptor [48]. From TRPL experiments, the electron-capture coefficient was found as $C_n = 3 \times 10^{-13}$ cm^{3}s^{-1} [48].

The assignment of the ~2.5 eV band to Hg was also confirmed in PL experiments involving radioactive isotopes [267]. Specifically, in samples doped with ^{197}Hg, which decays to ^{197}Au with a half-life of 64 h, the GL_{Hg} band diminished at the same rate, affirming its origin from Hg_{Ga} centers.

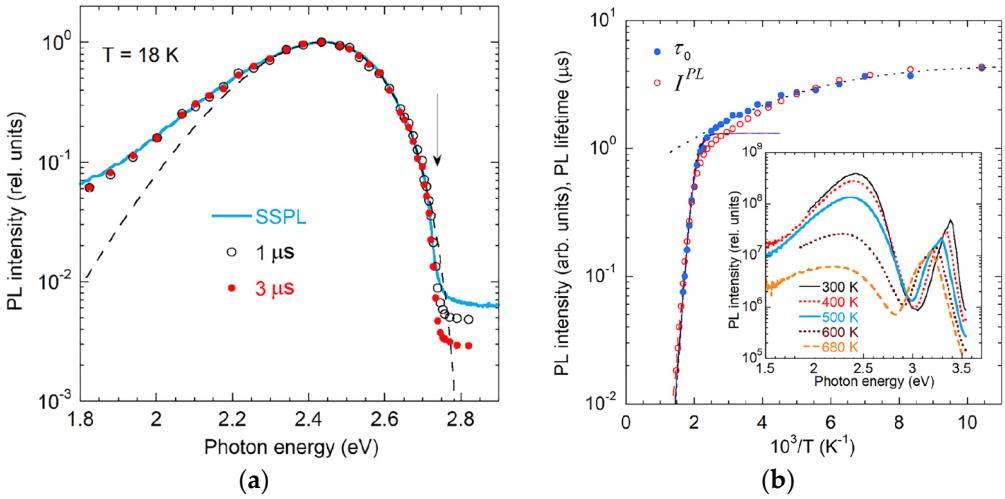

Figure 44. Hg_{Ga}-related GL_{Hg} band in GaN. (**a**) Comparison of the SSPL (at P_{exc} = 0.005 Wcm^{-2}) and TRPL (time delays of 1 and 3 μs) spectra at T = 18 K. The arrow indicates the expected position of the ZPL (2.73 eV), where the PL intensity abruptly drops. The dashed line is calculated using Equation (6) with parameters from Table 2. (**b**) Temperature dependences of PL intensity and PL lifetime of the GL_{Hg} band in Si-doped GaN implanted with Hg and annealed at 1200 °C. Solid line is calculated using Equation (2) with τ_0 = 1.3 μs and the following fitting parameters: $C_p = 1.2 \times 10^{-7}$ cm^3s^{-1}, and E_A = 630 meV. The inset shows PL spectra at selected temperatures. Reproduced from [48].

HSE hybrid functional calculations tuned to fulfill the generalized Koopman's condition, reproduce the shape and position of the Hg_{Ga}-related GL_{Hg} band relatively well [48,235]. The band maximum and ZPL are calculated at 2.45 eV and 2.83 eV, respectively, in close agreement with experimental observations (2.44 eV and 2.73 eV) [235].

4.8. PL from Other Defects

4.8.1. Isoelectronic Impurities

Isoelectronic defects, As_N and P_N, are responsible for the BL_{As} and BL_P bands with maxima at 2.6 and 2.9 eV, respectively. In high-quality GaN samples, both bands exhibit sharp ZPLs (at 2.952 eV for BL_{As} and 3.197 eV for BL_P) followed by phonon replicas [57]. These PL bands are often interpreted as excitons bound to isoelectronic defects [57]. Note that exciton binding energy cannot be directly compared to charge transition levels. For example, the $-/0$ transition level of Zn_{Ga} lies 400 meV above the VBM and is responsible for the BL_{Zn} band with a maximum at 2.9 eV and ZPL at 3.10 eV, whereas an exciton bound to Zn_{Ga}, with a binding energy of ~24 meV, produces a line at 3.455 eV in GaN [16].

According to early DFT calculations, the As_N defect is neutral in *n*-type GaN (as expected for isoelectronic impurities), and it acts as a donor with a 0/+ transition level at 0.31 eV [273] or 0.41 eV [274] above the VBM. Similar to other deep donors in GaN, after capturing a photogenerated hole, an electron can be captured at an excited state of As^+ near the CBM, followed by an internal transition that produces the BL_{As} band. Gil et al. [275] observed exponential decay of the blue band (at ~2.6 eV) in MBE-grown GaN:As, with τ_0 = 92 ns at T = 8 K. Assuming the excited state lies ~0.02 eV below the CBM [55], and using the ZPL at 2.952 eV (with $E_g \approx 3.512$ eV) [57], the 0/+ level of As_N can be estimated to lie 0.54 eV above the VBM. Thermal quenching of the BL_{As} band with an activation energy of ~50 meV at temperatures between 100 and 300 K was attributed to thermal release of electrons from As_N [276].

Similarly, the 0/+ level of P_N can be calculated at 0.29 eV above the VBM from the experimentally observed ZPL for the BL_P band, closely matching early DFT predictions

(0.22 eV) [274]. The related BL_P band is quenched with an activation energy of 0.28 eV at $T > 290$ K [58], consistent with thermal release of holes bound to P_N.

Interestingly, the intensity of the BL_{As} band in GaN:As samples varies significantly between reports. In HVPE GaN implanted with As ([As] = 10^{17} cm^{-3}), the BL_{As} band was well resolved (yet ~3000 times weaker than the NBE emission at P_{exc} = 0.26 Wcm^{-2}), and no other defect-related PL bands were observed between 2.4 and 3.4 eV [57]. In contrast, As-doped GaN samples grown by MOCVD with [As] = (0.3–5) × 10^{17} cm^{-3} (from SIMS) remained conductive *n*-type with n = (1–5) × 10^{17} cm^{-3}, and no BL_{As} band could be found [277,278]. In Ref. [277], the PL spectra were dominated by the C_N-related YL1 and Mg_{Ga}-related UVL bands (which could be recognized by their positions and shapes). The YL1 intensity decreased by a factor of ~100, while the UVL intensity increased by ~100-fold with increasing As concentration [277]. From these results, one could conclude that As either contributes to the UVL band or acts as a nonradiative defect. In fact, it is likely that the BL_{As} was too weak in that work because As_N donors in *n*-type material are expected to capture photogenerated holes very inefficiently compared to negatively charged C_N and Mg_{Ga} acceptors. The C, Mg, and possibly some nonradiative defects could be introduced due to specific growth or doping conditions. We observed relatively strong YL1 and UVL_{Mg} bands in GaN samples with concentrations of C and Mg below the SIMS detection limit [83].

4.8.2. PL from Implantation Damage

GaN, implanted with various elements, becomes non-luminescent due to the creation of numerous nonradiative defects. For example, simulations indicate that implantation of Zn ions into GaN with a fluence of 10^{16} cm^{-2} creates ~10^{22} cm^{-3} of V_{Ga} and over 10^{23} cm^{-3} of V_N defects [279]. Post-implantation annealing partially repairs this damage, though some defects remain. Pankove and Hutchby [87] implanted 35 elements into GaN and observed yellow and red PL bands in nearly all samples after annealing for one hour at 1000–1050 °C in flowing ammonia. Although the YL band at 2.15 eV was thought to be implantation-damage-related [87], it is highly likely that it was the C_N-related YL1 band due to contamination with C (except for the YL_{Be} band in Be-implanted GaN). The red band at ~1.75 eV, however, was linked to a defect forming during thermal annealing (appearing even in unimplanted GaN) [87]. Chen and Skromme [57,280] investigated GaN implanted with various elements and attributed a similar red band (at 1.73–1.78 eV) to implantation-induced damage, as the band was absent in annealed unimplanted GaN.

We observed a red band with a maximum at ~1.6 eV (Positions of the broad band maxima reported by various authors must be compared with caution. In particular, the RL5 band maximum redshifts by about 0.1 eV after applying the λ^3 correction) (denoted RL5) in GaN implanted with Cd, Ca, Hg, F, or Cl ions (Figure 45a). Due to limitations of the measurement setup, the full RL5 band shape could not be studied at $\hbar\omega < 1.5$ eV. Nevertheless, its consistent appearance in GaN implanted with various ions suggests a common origin—implantation damage.

The RL5 intensity decreases modestly (by a factor of 2–3) with increasing temperature from 18 to 300 K. At least in the cases of implantations with F, Cl, or co-implantation with Be and F, the RL5 band was observed only in conductive *n*-type GaN samples (HVPE GaN with [Si] ≈ 3 × 10^{18} cm^{-3}) [214]. TRPL measurements reveal nonexponential decay of RL5 at T = 18–100 K (as t^{-m} with m = 0.8–1.0 between 0.02 and 1000 μs), while nearly exponential decay was observed for YL1 and BL1 in the same samples, with lifetimes corresponding to n = 10^{18} cm^{-3}. The RL5 band could not be excited by the 2.805 eV line of the HeCd laser, unlike the RL_C band in C-doped GaN (Section 4.1.3). It is likely that the RL5 band is caused by deep DAP transitions involving implantation-induced defects.

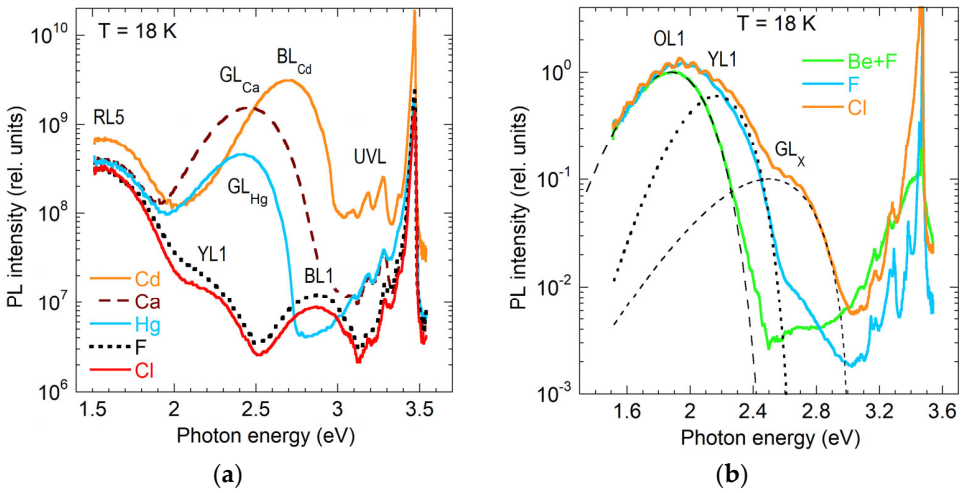

Figure 45. Low-temperature PL spectra from ion-implanted GaN. (**a**) RL5 band (~1.6 eV) in GaN samples implanted with Cd, Ca, Hg, F, and Cl. (**b**) Normalized PL spectra from SI GaN implanted with F, Cl, and co-implanted with Be and F. Dashed lines show deconvolution of the PL spectrum for GaN:Cl using Equation (6). Parameters for OL1 and YL1 bands are given in Table 2, and parameters for the GL_X component are: $S_e = 3$, $E_0^* = 3$ eV, and $\hbar\omega_{max} = 2.5$ eV.

In SI GaN implanted with F, Cl, or co-implanted with Be and F, an orange luminescence (OL1) band with a maximum at ~1.9 eV was observed [214]. The OL1 was particularly strong in PL spectra of SI GaN:Be,F with [Be] < [F] (Figure 45b). The same OL1 band also appears in GaN samples implanted with only F, and possibly the same band contributes to the PL spectrum from SI GaN implanted with Cl (Figure 45b). The defect responsible for OL1 is unlikely to include Be, as the band is absent in GaN:Be,F samples with [Be] > [F] or in Be-implanted GaN [151]). It may involve F (because the OL1 band appears only when [Be] < [F] or in F-implanted GaN). However, the OL1 band could also originate from a defect unrelated to F if the OL1 band in F- and Cl-implanted samples is identical, which is premature to conclude because the OL1 band in Cl-implanted GaN overlaps with the C_N-related YL1 band and is poorly resolved. First-principles calculations suggest that the OL1 band may originate from the $V_{Ga}F_N$ complex, with transitions via its 0/+ level at about 1.0 eV above the VBM (if the Fermi level is lower than ~2 eV above the VBM) [151]. However, in *n*-type GaN, the F_NV_{Ga} defect is predicted to be negatively charged and is not expected to contribute to visible PL. The identity of the shoulder at ~2.5 eV in Cl-implanted GaN (the GL_X band in Figure 45b) remains unresolved.

5. Advances in Defect-Related Photoluminescence in GaN Since 2005

This section reviews key developments in understanding defect-related PL in GaN since 2005, focusing on the identification of PL bands, quenching mechanisms, recombination processes, multi-charged defects, and advances in computational modeling. While significant progress has been made, persistent challenges remain in defect identification and establishing a quantitative understanding of their optical activity.

5.1. PL Bands in Undoped GaN

As of 2005, the origins of several major PL bands in undoped GaN were under debate. In particular, the YL band at 2.2 eV was commonly attributed to carbon-related defects (excluding isolated C_N) or to V_{Ga}-related complexes, such as $V_{Ga}O_N$. The UVL band at 3.28 eV was linked to a variety of candidates, including Mg_{Ga}, C_N, Si_{Ga}, and structural defects. The RL2 and GL2 bands in SI GaN were incorrectly assigned to Ga_N antisite defects, while the GL1 band observed in HVPE Ga_N was interpreted as a secondary emission from

YL-related centers. The BL2 band in high-resistivity GaN was often linked to Ga vacancies or confused with the Zn-related BL1 band.

Recent studies have clarified the assignments of most PL bands (Table 1). The YL band (YL1) is now firmly attributed to the C_N acceptor, which forms readily due to residual carbon contamination. Its -/0 and 0/+ charge transition levels give rise to the YL1 and BL_C bands, respectively, in agreement with modern theoretical predictions. The UVL band (UVL_{Mg}) at ~3.28 eV is unambiguously attributed to Mg_{Ga}; no evidence supports the presence of other shallow acceptors in undoped GaN (an exception is the shallow Be-related acceptor in Be-doped GaN). The BL2 band originates from the C_NH_i complex, which can dissociate under UV exposure, subsequently giving rise to the YL1 band. The GL2 and RL2 bands are attributed to V_N-related centers, specifically isolated V_N and AV_N complexes, respectively.

In conductive *n*-type GaN, PL bands, such as RL1, YL1, BL1, and UVL, result from electron transitions involving acceptor levels. Hole capture at these acceptors occurs without an energy barrier. At low temperatures, DAP-type recombination occurs, involving these acceptors and shallow donors. Above 50 K, transitions from the CBM become dominant. These PL bands are strong due to efficient hole capture by negatively charged acceptors. In high-resistivity or SI GaN samples, competition for photogenerated electrons enables PL from deep donors, such as RL2, GL2, BL2, via internal transitions.

5.2. Mechanisms of PL Quenching

Before ~2010, quenching of PL from defects in semiconductors was attributed to two mechanisms, both modeled with Equation (2): (i) conversion of a radiative defect to a nonradiative state (Seitz–Mott mechanism), where the activation energy E_A represents a potential barrier in adiabatic potentials, and (ii) thermal emission of bound carriers to the conduction or valence band, followed by recapture at nonradiative defects (Schön–Klasens mechanism), where E_A in Equation (2) is an ionization energy. In fact, no examples of the first mechanism can be found for defects in GaN. The quenching of the GL2 and RL2 bands, erroneously explained with the Seitz–Mott mechanism [16], is now attributed to thermal emission of electrons from an excited state ~0.1 eV below the CBM to the conduction band (Sections 3.2.2 and 3.3.2).

A significant development came in 2011 with the discovery of the TAQ mechanism, initially observed in Zn-doped GaN [52]. Although the $I^{PL}(T)$ dependences could be formally fitted with Equation (2), the extracted parameters *C* and E_A are anomalously large, lacking physical meaning. Subsequent studies demonstrated that the TAQ mechanism is a general phenomenon, applicable to GaN doped with various acceptors, including Zn, Mg, C, Be, Cd, and Hg, as well as other SI semiconductors [74]. The essence of the TAQ mechanism is a conversion from population inversion at low temperatures to near-equilibrium population above a critical temperature, which increases with excitation intensity—hence the term "tunable".

Furthermore, it is sometimes challenging to explain PL quenching and interpret associated activation energies. For example, when PL from acceptors in *n*-type GaN is quenched by the Schön–Klasens mechanism, the E_A found from fits with Equation (2) is often lower than the true ionization energy. This discrepancy can arise from inadequate experimental conditions (e.g., very high P_{exc}), nonexponential PL decay, or the presence of local electric fields [75].

An additional phenomenon, known as "negative thermal quenching", where the PL intensity increases with temperature, has been observed and explained by a competition between radiative and nonradiative recombination channels for photogenerated carriers [53,81]. A special case of two-step quenching of the YL_{Be} band in Be-doped GaN

samples is explained by a sudden reduction in light extraction efficiency from Be_{Ga} centers after temperature-activated reorientation of related defect dipoles (Section 4.2.2).

5.3. Radiative and Nonradiative Recombination

5.3.1. Internal Quantum Efficiency

While quantum efficiency is a key parameter to quantify PL, determining the EQE of PL remains technically challenging, and the IQE η cannot be measured directly. The EQE can be obtained using integrating sphere techniques, which require careful calibration and analysis [67–71]. IQE exceeds EQE by the light extraction efficiency, which depends on various sample-specific parameters, including surface morphology, crystal polarity, and refractive index contrast at interfaces.

Nevertheless, several phenomenological models have been developed to estimate the absolute IQE from temperature- or excitation-dependent PL measurements, particularly in samples exhibiting strong PL [53,81]. One such approach is based on analyzing the competition among radiative channels when an intense PL band (with a close to unity η) undergoes quenching via the Schön–Klasens mechanism. Under these conditions, the intensities of all other PL bands increase by a factor of R (the negative thermal quenching), and the absolute IQE of the quenched band can be expressed as $\eta = 1 - R^{-1}$ [53]. The method is particularly efficient in conductive n-type, where PL intensities are proportional to the product of hole-capture coefficients and defect concentrations [39]. Once absolute IQEs are found, the concentrations of defects responsible for specific PL bands can also be estimated [80]. While foundational concepts for quantifying PL in this manner were introduced earlier [16], these methods have been substantially refined and extended in recent studies [38,39,52,53,80,81,83].

5.3.2. Nonradiative Recombination

Nonradiative recombination in GaN originates from both point defects and extended structural defects, including dislocations, domain boundaries, interfaces, and surfaces. Point defects responsible for nonradiative recombination are typically deep-level centers characterized by strong electron–phonon coupling, where the recombination energy of electrons and holes is dissipated through multiphonon emission. Recent studies have also suggested that radiative defects may become nonradiative under high carrier concentrations or intense optical excitation via the TAAM recombination mechanism [185,281,282].

Structural defects, particularly threading dislocations, have long been implicated in nonradiative losses. Spatially resolved micro-CL and micro-PL studies consistently reveal reduced emission at dislocation sites, observed as “dark spots” in PL or CL maps [283–285]. The suppression of emission at these locations can be attributed to either nonradiative recombination at dislocation sites or local carrier depletion induced by electric fields from charged dislocations.

Phenomenological models of carrier recombination typically describe the recombination rate as a sum of parallel radiative and nonradiative processes, where each recombination channel is associated with a specific recombination center. Nonradiative recombination through a large number of unresolved pathways is commonly modeled by an effective deep-level defect characterized by empirical electron- and hole-capture coefficients, as well as an effective concentration [52,53].

5.3.3. Surface Effects on PL

The surface of GaN can significantly affect its PL, especially at elevated temperatures and in oxygen- or water-containing ambient. For example, the NBE intensity in undoped n-type GaN has been observed to increase by a factor of 3–14 after photoelectrochemical oxidation [286], and by 4–6 times after sulfide treatment [287]. In contrast, prolonged

exposure to HeCd laser irradiation in air can reduce the NBE intensity due to photoinduced surface oxidation [288]. Under high-vacuum conditions at T = 10 K, however, continuous HeCd laser exposure enhances the NBE intensity, which is attributed to photoinduced desorption of surface oxygen [289]. Similarly, the YL1 intensity in SI GaN:C was found to decrease by a factor of ~300 in ambient air or oxygen compared to vacuum [290]. These observations illustrate the strong influence of surface conditions on PL, which are typically attributed to nonradiative recombination at surface states and/or changes in the width of the near-surface depletion region.

In *n*-type GaN, an upward band bending (~1 eV at room temperature) is observed due to the accumulation of negative charges at the surface [291–293]. The associated depletion region in such material extends up to ~0.1 μm (for $n \approx 10^{17}$ cm^{-3}). Within this region, photogenerated electrons and holes are rapidly separated by the strong built-in electric field and subsequently recombine nonradiatively—a phenomenon described as the field-effect mechanism [294]. Modifying the surface charge changes the width of the depletion region and, consequently, the PL intensity. Although the minority hole diffusion length in GaN is short (0.2 μm or less [291,295]), accurate modeling of PL intensity variations must account for both carrier drift and diffusion within the depletion layer [296]. Nevertheless, in many GaN samples, the field-effect mechanism plays only a minor role. Instead, significant changes in PL intensity arise primarily from nonradiative recombination at surface states, the concentration of which depends on ambient atmosphere and surface treatment conditions [297]. High density of nonradiative defects near the surface can also significantly suppress PL. For example, mechanical polishing of freestanding GaN templates with diamond slurries, ending with ~1 μm particle size, reduced the PL intensity by four orders of magnitude despite minimal changes in band bending [123].

In *p*-type GaN, surface band bending is downward and can reach up to 2 eV at elevated temperatures [298,299]. However, the depletion region is narrow (<10 nm) because of the high concentration of uncompensated Mg acceptors. At low temperatures, band bending is expected to be small in conditions of PL (< 10 kT). Nevertheless, surface effects in such samples can still significantly influence the PL intensity and its temperature behavior. Notably, large shifts (up to 0.6 eV) of the UVL$_{Mg}$ band with varying excitation power have been observed in Mg-doped GaN at low temperatures (Section 4.3.4). These shifts were attributed to diagonal electron transitions occurring within the near-surface depletion region [54,62].

5.4. Electronic Structure

5.4.1. Multi-Charged Defects

Transitions via different charge transition levels of multi-charged defects in GaN are expected to produce distinct PL bands. A well-established example is the C_N defect responsible for the YL1 and BL_C bands, associated with electron transitions via the $-/0$ and $0/+$ levels, respectively [25,60] (Section 4.1.1). Preliminary results also suggest that the $-/0$ and $0/+$ levels of the Be_{Ga} defect produce the YL_{Be} and BL_{Be} bands [61] (Section 4.2.5). In another case, the BL3 band, observed in HVPE GaN at high P_{exc}, is presumably a secondary emission from the RY3 defect, occurring after the capture of two holes. The GL1 band is a secondary emission from yet unknown defects.

Distinct charge transition levels for other multi-charged defects, such as V_{Ga}, V_N, and complexes containing these vacancies, have not been clearly identified in PL experiments. Attributions of the GL2 band to transitions via the +/2+ level of V_N and RL_A bands to transitions via the $0/+$ level of AV_N complexes (with A representing cation acceptors) are also preliminary, as more than one transition level of a multi-charged defect may contribute to the observed PL bands.

5.4.2. Dual-Nature Defects

The concept of dual-nature defects, where a single charge state exhibits multiple transition levels due to different carrier localization configurations, has been theoretically proposed [206]. This phenomenon is believed to be potentially widespread in wide-bandgap semiconductors. Experimentally, however, dual-nature behavior has been unambiguously confirmed for only one defect in GaN: the Be_{Ga} acceptor [45]. In its neutral charge state, this defect exhibits two polaronic configurations, with the $-/0$ transition levels located at 0.35 and 0.39 eV above the VBM. In the higher-energy state (0.39 eV), the hole is localized on a neighboring nitrogen atom along the c-axis, whereas in the lower-energy state (0.35 eV), the hole is localized on one of the three basal-plane nitrogen atoms. Additionally, a third, shallow $-/0$ level at 0.24 eV above the VBM corresponds to a weakly localized hole. First-principles calculations also predict dual-nature behavior for other acceptors, including Mg_{Ga} [206,231,232,235], Zn_{Ga} [206,235], and $Be_{Ga}O_NBe_{Ga}$ complex [64]. To date, however, these predictions remain experimentally unverified, and PL associated with only shallow levels has been observed for these defects.

5.4.3. Excited States

Excited states associated with deep donors have recently been identified by PL for several centers in GaN, including C_NH_i (BL2), V_N (GL2), and AV_N complexes (RL_A bands with A = Be_{Ga}, Mg_{Ga}, and Ca_{Ga}). Donor-like states of multi-charged defects also exhibit excited states near the CBM, as observed for C_N (BL_C), Be_{Ga} (BL_{Be}), and RY3 center (BL3). Among acceptor-like defects, only the RY3 center exhibits an excited state near the VBM (Section 3.2.3). Excited states have also been predicted for multi-charged defects, such as $V_{Ga}O_N$ and $V_{Ga}H_i$ [118], though these states have not yet been directly confirmed experimentally.

An unusual behavior, where PL lifetime significantly increases with temperature, has been observed for the GL1 band. This effect is attributed to nonradiative capture of electrons via a ladder of excited states by the Lax mechanism and subsequent radiative recombination producing the GL1 band (Section 3.3.1). By analogy with the so-called giant traps in Ge and Si, the related defects have been termed optically generated giant traps.

5.5. Identification of Defects

5.5.1. Conventional Approaches

PL spectroscopy is an indispensable tool for identifying defect-related emission bands and probing their properties. However, it often fails to provide direct information about the chemical composition or atomic structure of the underlying defects. Historically, in undoped semiconductors and insulators, PL bands were typically attributed to native point defects (e.g., cation vacancies in crystals grown under anion-rich conditions), whereas in doped materials they were commonly linked to impurity dopants [300,301]. A widely used strategy for defect identification involves correlating PL intensities with impurity concentrations obtained from SIMS measurements. Another approach compares the positions and shapes of PL bands with theoretical databases generated from first-principles calculations to propose defect assignments.

However, extensive studies of GaN have revealed serious limitations of these approaches. In particular, the assumption that PL intensity scales linearly with defect concentration holds only under restricted conditions, such as low concentrations of radiative defects, weak excitation, and in conductive *n*-type material. As illustrated in Figure 46, the intensities of the UVL_{Mg} (UVL), BL_{Zn} (BL1), and YL1 bands are proportional, respectively, to the concentrations of Mg, Zn, and C impurities only up to ~10^{16} cm^{-3}, where the IQE of these PL bands approaches unity. Note that the SIMS detection limit for these impurities is in the 10^{15}–10^{16} cm^{-3} range. Beyond these limits, the lack of proportionality (and some-

times even anticorrelation) between PL intensity and impurity concentration often leads to erroneous defect assignments.

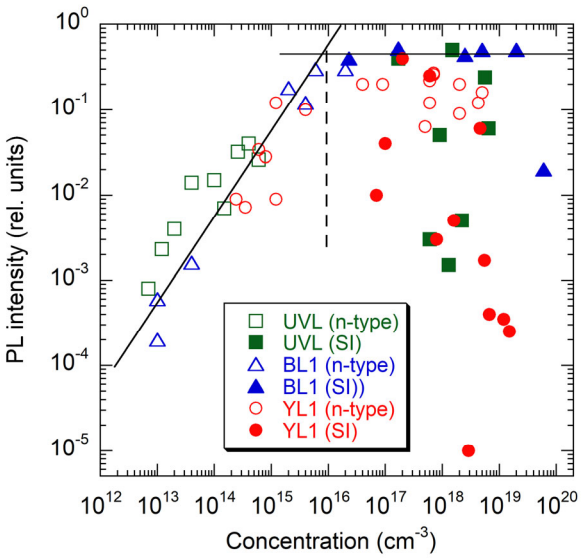

Figure 46. Dependences of PL intensity on defect concentration. The UVL, BL1, and YL1 bands are related to the Mg_{Ga}, Zn_{Ga}, and C_N acceptors, respectively. Reproduced from [34].

Modern first-principles calculations can predict the properties of point defects with relatively high accuracy (Section 5.6). When combined with reliable experimental data, they provide a powerful framework for defect identification in GaN. Although PL offers the most direct and accurate information on defects in GaN, complementary experimental techniques supply essential corroborative evidence. In particular, temperature-dependent Hall effect measurements have confirmed the spectroscopically found $-/0$ levels of the Be_{Ga}, Zn_{Ga}, and C_N acceptors in SI (*p*-type) GaN [215,260,302]. Photo-EPR studies of C-doped GaN have verified the model of the C_N acceptor (Section 3.1.2), for which an isotropic *g*-value of 1.987 ± 0.001 has been found [302–304]. It is worth noting that *g* factors for acceptors are generally expected to exceed the free-electron value ($g_e = 2.0023$) [122,216,305]; however, exceptions exist (including the case of C_N), and relying solely on the *g*-value for defect identification may lead to misassignments.

Capacitance-based techniques, such as DLTS and DLOS, have revealed numerous electrically active defects in GaN, providing key parameters, including thermal ionization energies and carrier-capture cross-sections [5,306,307]. For brevity, only a few examples, closely related to the PL data discussed in this review, are highlighted here. The presence of two charge states of the C_N defect has been conclusively verified by DLTS [26,184]. Horita et al. [308] identified the $0/+$ level of V_N at 0.13 eV below the CBM and the $-/0$ level of N_i at 0.98 eV below the CBM in *n*-type GaN irradiated with 137 keV electrons. In similarly irradiated *p*-type GaN, a DLTS peak, corresponding to a hole trap with an ionization energy of 0.52 eV above the VBM, was observed and tentatively attributed to either the $+/3+$ level of V_N or the $+/2+$ level of N_i [309]. Zajac et al. [310] investigated Mg-doped *p*-type GaN grown by the AT method. Using Laplace-transform photoinduced transient spectroscopy, they revealed hole traps at 0.43–0.45 eV above the VBM, with hole-capture coefficients $C_p \approx 3 \times 10^{-11}$–$10^{-10}$ cm^{3}s^{-1}. These traps were attributed to the $3+/+$ and $2+/+$ transition levels of V_N. An electron trap at 0.6 eV below the CBM, detected by DLTS in Si-doped *n*-type GaN grown by MOCVD, was attributed to the Fe_{Ga} acceptor [311]. A Be-related electron trap with a level at 0.24–0.39 eV below the CBM was found by thermal admittance spectroscopy and DLTS in GaN implanted with radioactive ^{7}Be isotopes [312], likely corresponding to the Be_i donor.

Despite these advances, correlating PL with DLTS (or other capacitance techniques) remains challenging [5]. In DLTS, activation energies correspond to carrier emission from a defect to the conduction band (electron traps) or to the valence band (hole traps), and are accompanied by measurements of electron or hole-capture coefficients (or capture cross-sections). This approach is conceptually similar to the extraction of E_A and C_p from PL quenching (Section 2.2.2), with the difference that DLTS detects both radiative and nonradiative defects. As with PL quenching, the uncertainties in extracted E_A and C_p may be significant. Moreover, both E_A and C_p may be temperature-dependent, and the activation energies measured by DLTS may differ from actual ionization energies if a capture barrier exists [101]. Although numerous electron and hole traps in GaN have been reported in DLTS studies [2,5,313], and databases of defect levels have been compiled [314], the large scatter in the reported parameters often makes it difficult to reliably correlate DLTS data with PL results.

5.5.2. Identification from Radioactive Isotopes

One of the most reliable methods for revealing the chemical origin of luminescence centers in GaN involves implantation of radioactive isotopes, where the parent or daughter nucleus is directly responsible for a specific PL band. As discussed in Sections 4.5 and 4.7, the BL_{Cd} and GL_{Hg} bands were conclusively attributed to Cd and Hg, respectively, through the decay of implanted ^{111}Ag isotope into ^{111}Cd, and ^{197}Hg isotope into ^{197}Au [267,268]. In the same experiments, PL bands near 1.5 eV with characteristic fine structures were assigned to Ag and Au impurities.

From decays of radioactive ^{72}Se and ^{71}As isotopes, undergoing chemical transmutation, the BL_{As} band, with the ZPL at 2.945 eV and characteristic phonon-related fine structure, was confirmed as originating from As_N. Additional PL bands at 1.49 eV and 3.398 eV were attributed to recombination centers involving Se and Ge, respectively [315]. From the decay of radioactive ^{191}Pt isotopes, sharp lines at 1.461, 1.446, and 1.273 eV, followed by phonon replicas, were attributed to Pt [316].

5.5.3. Confidence Levels

The defect attributions summarized in Table 1 represent the current state of understanding and are subject to change as new experimental and theoretical evidence emerges. Nonetheless, the following confidence levels reflect the author's assessment.

- High Confidence (90–99%): YL1 and BL_C (C_N), UVL or UVL_{Mg} (Mg_{Ga}), BL1 or BL_{Zn} (Zn_{Ga}), YL_{Be} and UVL_{Be3} (Be_{Ga}), BL2 (C_NH_i), BL_{Ca} or AL (Ca_{Ga}), BL_{Cd} (Cd_{Ga}), GL_{Hg} (Hg_{Ga}).
- Moderate Confidence (50–80%): GL2 (+/2+ level of V_N), RL_{Mg} (+/0 level of $Mg_{Ga}V_N$), RL_{Ca} (+/0 level of $Ca_{Ga}V_N$), RL_{Be} (+/0 level of $Be_{Ga}V_N$), BL_{Mg} (Deep DAP), BL_{As} (As_N), BL_P (P_N), UVL_{Be} ($Be_{Ga}O_NBe_{Ga}$). The V_{Ga}, $V_{Ga}O_N$, $V_{Ga}H_i$, $Be_{Ga}O_N$, C_NO_N, and C_NSi_{Ga} defects do not contribute to PL, at least at $\hbar\omega > 1.5$ eV.
- Low Confidence (20–40%): YL2, OL3, and RL4 ($V_{Ga}xO_NyH$ donors with x, y = 1,2), RL_C (tri-carbon complex), BL_{Be} (0/+ level of Be_{Ga}).
- Speculative (<10%): RL3, YL3, and BL3 (Fe_{Ga} or Fe_{Ga}-containing complex), RL1 and GL1 (Cl), RL2 (AV_N, with A being an acceptor other than Be, Mg, or Ca), GL_{Be} (Be-containing complex), RL5 (unknown defect from implantation damage), OL1 (F or implantation damage-related defects).

5.6. Advances in First-Principles Calculations

Early first-principles calculations of defects in semiconductors relied on local or semi-local approximations within DFT, which significantly underestimated the calcu-

lated bandgap and required corrections that introduced large uncertainties in defect levels [17,21,22,317]. As a result, inaccurate predictions of defect transition levels, combined with the limited reliability of experimental identification methods, often led to incorrect assignments of PL bands.

In recent years, major progress has been made in improving the accuracy of defect calculations in GaN and other wide-bandgap semiconductors [318]. The adoption of hybrid functionals, particularly the widely used HSE functional [319], has provided a practical compromise between computational cost and accuracy. By incorporating a portion of Hartree–Fock exchange energy, these methods yield more reliable predictions of defect formation energies and transition levels. A common tuning of the HSE functional includes adjusting the fraction of Hartree-Fock exchange to 0.31, along with a range separation parameter of 0.2 $Å^{-1}$, to reproduce the experimental GaN bandgap of 3.5 eV [24,182,234,320]. An alternative approach is to tune the HSE functional using the Koopmans' theorem, which ensures that the self-interaction energy in the defect state orbitals is canceled by wavefunction relaxation [232,235,321]. While this improves defect transition energies referenced to the VBM, it also tends to underestimate the bandgap. Since different parametrizations can yield different outcomes, careful and consistent calibration is essential [104]. Most calculations employ periodic boundary conditions in supercells, which require *a posteriori* corrections to the total energy. The most common correction is the Freysoldt-Neugebauer-Van de Walle (FNV) [322,323] scheme.

Despite these improvements, theoretical predictions of PL band maxima and their ZPLs still exhibit typical uncertainties of 0.1–0.5 eV [235]. Overconfidence in theoretical predictions and the unreliability of some experimental data continue to hinder accurate defect identification. In practice, many reported assignments are based on a superficial agreement between calculated transition energies and experimental PL maxima or DLTS peaks [96,103,324]. Given the large number of unidentified PL bands and traps in GaN and the even greater number of theoretically predicted transitions via all possible defects, the likelihood of accidental matches is high. To improve reliability, PL band identification must go beyond a formal energy comparison. Detailed spectroscopic analysis (which includes revealing ZPL and fine structure), consideration of temperature dependence, recombination dynamics, isotope effects, and corroborating evidence from complementary methods (e.g., DLTS, Hall effect, ODMR, PAS) are essential.

A case study involving the Be_{Ga} acceptor highlights both the progress and pitfalls of theory-experiment comparison [45,46]. Although first-principles theory correctly predicted the dual nature of this acceptor [206], advanced HSE hybrid functional calculations suggested that its polaronic states should produce a PL band with a maximum at 1.67–1.80 eV [207–210]. The closest match for this prediction would be the RL_{Be} band at 1.77 eV, observed in some Be-doped GaN samples (Section 4.2.4). However, comprehensive PL studies conclusively demonstrated that the polaronic states of Be_{Ga} are instead responsible for the YL_{Be} band with a maximum at 2.15 eV [45].

6. Conclusions

Substantial progress has been made in recent years toward understanding PL from defects in GaN. Most notably, the origin of the long-debated yellow band (YL1) has now been definitively resolved. In the majority of undoped GaN samples, YL1 arises from unintentional carbon contamination and is associated with electron transitions from the CBM (or from shallow donors at $T < 50$ K) to the C_N acceptor. The discovery of ZPLs for the YL1 and BL_C bands at 2.59 eV and 3.15 eV, respectively, enabled precise determination of the C_N defect's $-/0$ and $0/+$ charge transition levels: at 0.916 ± 0.003 and 0.33 ± 0.01 eV above the VBM in the low-temperature limit. Several other PL bands in undoped GaN

have also been reliably identified, including the BL2 band at 3.0 eV (attributed to C_NH_i) and the GL2 band at 2.33 eV (associated with V_N).

To facilitate consistent classification and discussion, a new nomenclature has been introduced, in which PL bands are designated and recognized according to their peak position (or color), shape, and other distinctive properties (Tables 1–3). The accurate identification of PL bands requires careful experimental characterization, since band positions and shapes may vary substantially with temperature and excitation intensity, particularly in semi-insulating samples.

The temperature dependence of PL has long been used to estimate defect ionization energies, in a manner analogous to the DLTS method. However, this approach is valid only when PL quenching follows the Schön–Klasens (multicenter) mechanism. To date, no clear cases of the Seitz–Mott (one-center) mechanism have been identified in GaN. Instead, a third mechanism—tunable and abrupt quenching—has been found for many defects in semi-insulating GaN. This abrupt quenching occurs at a critical temperature T_0, which increases with excitation intensity. The phenomenon is reminiscent of a phase transition, in which population inversion and photo-induced n-type conductivity at $T < T_0$ are replaced by near-equilibrium carrier population and p-type conductivity at $T > T_0$.

Recent PL studies have also elucidated the electronic structures of several important defects in GaN. In particular, the theoretically predicted dual nature of the Be_{Ga} acceptor has been experimentally confirmed. Three distinct $-/0$ transition levels, corresponding to different hole localizations, have been identified for the Be_{Ga} acceptor. The growing body of high-quality experimental data from PL studies now provides a critical foundation for refining first-principles calculations, ultimately aiming at reliable predictions of defect properties in GaN and other wide-bandgap semiconductors.

Funding: The research of M.A.R. leading to these results was partly supported by the National Science Foundation under grant DMR-2423874.

Data Availability Statement: Not applicable.

Acknowledgments: The author is grateful to D. O. Demchenko (VCU) for fruitful discussions.

Conflicts of Interest: The author declares no conflicts of interest.

Abbreviations

The following abbreviations are used in this manuscript (in alphabetical order):

AL	Aquamarine luminescence
AT	Ammonothermal
BL	Blue luminescence
CL	Cathodoluminescence
DAP	Donor-acceptor pair
DFT	Density functional theory
DLOS	Deep level optical spectroscopy
DLTS	Deep level transient spectroscopy
EQE	External quantum efficiency
EPR	Electron paramagnetic resonance
FTIR	Fourier transform infrared
FWHM	Full width at half maximum
GL	Green luminescence
HSE	Heyd-Scuseria-Ernzerhof
HNPS	High nitrogen pressure solution
HVPE	Hydride vapor phase epitaxy
IQE	Internal quantum efficiency

LED	Light-emitting diode
LEEBI	Low energy electron beam irradiation
LO	Longitudinal optical
MBE	Molecular beam epitaxy
MOCVD	Metalorganic chemical vapor deposition
NBE	Near-band-edge
NDF	Neutral density filter
ODMR	Optically detected magnetic resonance
OL	Orange luminescence
PAS	Positron annihilation spectroscopy
PL	Photoluminescence
PLE	Photoluminescence excitation
PMT	Photomultiplier tube
RL	Red luminescence
SD-SA	Shallow donor-shallow acceptor
SI	Semi-insulating
SIMS	Secondary ion mass spectrometry
SSPL	Steady-state photoluminescence
TAAM	Trap-assisted Auger-Meitner
TAQ	Tunable and abrupt quenching
TRPL	Time-resolved photoluminescence
UV	Ultraviolet
UVL	Ultraviolet luminescence
VBM	Valence band maximum
YL	Yellow luminescence
ZPL	Zero-phonon line

References

1. Nakamura, S.; Fosol, G. *The Blue Laser Diode*; Springer: Berlin/Heidelberg, Germany, 1998.
2. Morkoç, H. *Handbook of Nitride Semiconductors and Devices*; Wiley: New York, NY, USA, 2008.
3. Mishra, U.K.; Shen, L.; Kazior, T.E.; Wu, Y. GaN-Based RF Power Devices and Amplifiers. *Proc. IEEE* **2008**, *96*, 287–305. [CrossRef]
4. Nakamura, S.; Krames, M.R. History of Gallium–Nitride-Based Light-Emitting Diodes for Illumination. *Proc. IEEE* **2013**, *101*, 2211–2220. [CrossRef]
5. Reshchikov, M.A. Point defects in GaN. In *Semiconductors and Semimetals: Defects in Semiconductors*; Jagadish, C., Privitera, V., Romano, L., Eds.; Academic Press: Burlington, UK, 2015; Volume 91, pp. 315–367.
6. Monemar, B.; Paskov, P.P.; Bergman, J.P.; Toropov, A.A.; Shubina, T.V. Recent developments in the III-nitride materials. *Phys. Status Sol. B* **2007**, *244*, 1759–1768. [CrossRef]
7. Kornitzer, K.; Ebner, T.; Thonke, K.; Sauer, R.; Kirchner, C.; Schwegler, V.; Kamp, M.; Leszczynski, M.; Grzegory, I.; Porowski, S. Photoluminescence and reflectance spectroscopy of excitonic transitions in high-quality homoepitaxial GaN films. *Phys. Rev. B* **1999**, *60*, 1471–1473. [CrossRef]
8. Monemar, B.; Paskov, P.P.; Bergman, J.P.; Toropov, A.A.; Shubina, T.V.; Malinauskas, T.; Usui, A. Recombination of free and bound excitons in GaN. *Phys. Stat. Sol. B* **2008**, *245*, 1723–1740. [CrossRef]
9. Freitas, J.A., Jr.; Culbertson, J.C.; Glaser, E.R. Characterization of Defects in GaN: Optical and Magnetic Resonance Techniques. *Crystals* **2022**, *12*, 1294. [CrossRef]
10. Callsen, G.; Kure, T.; Wagner, M.R.; Butte, R.; Grandjean, N. Excited states of neutral donor bound excitons in GaN. *J. Appl. Phys.* **2018**, *123*, 215702. [CrossRef]
11. Freitas, J.A., Jr.; Moore, W.J.; Shanabrook, B.V.; Braga, G.C.B.; Koleske, D.D.; Lee, S.K.; Park, S.S.; Han, J.Y. Shallow donors in GaN. *Phys. Stat. Sol. B* **2003**, *240*, 330–336. [CrossRef]
12. Wysmolek, A.; Stepniewski, R.; Potemski, M. Magneto-spectroscopy of donor-bound excitons in GaN. *Phys. B* **2007**, *401–402*, 441–446. [CrossRef]
13. Ishitani, Y.; Takeuchi, K.; Oizumi, N.; Sakamoto, H.; Ma, B.; Morita, K.; Miyake, H.; Hiramatsu, K. Excitation and deexcitation dynamics of excitons in a GaN film based on the analysis of radiation from high-order states. *J. Phys. D Appl. Phys.* **2016**, *49*, 245102. [CrossRef]

14. Chichibu, S.F.; Uedono, A.; Kojima, K.; Ikeda, H.; Fujito, K.; Takashima, S.; Edo, M.; Ueno, K.; Ishibashi, S. The origins and properties of intrinsic nonradiative recombination centers in wide bandgap GaN and AlGaN. *J. Appl. Phys.* **2018**, *123*, 161413. [CrossRef]
15. Rodina, A.V.; Dietrich, M.; Göldner, A.; Eckey, L.; Hoffmann, A.; Efros, A.L.; Rosen, M.; Meyer, B.K. Free excitons in wurtzite GaN. *Phys. Rev. B* **2001**, *64*, 115204. [CrossRef]
16. Reshchikov, M.A.; Morkoç, H. Luminescence properties of defects in GaN. *J. Appl. Phys.* **2005**, *97*, 061301. [CrossRef]
17. Van de Walle, C.G.; Neugebauer, J. First-principles calculations for defects and impurities: Applications to III-nitrides. *J. Appl. Phys.* **2004**, *95*, 3851–3879. [CrossRef]
18. Boguslawski, P.; Bernholc, J. Doping properties of C, Si, and Ge impurities in GaN and AlN. *Phys. Rev. B* **1997**, *56*, 9496–9505. [CrossRef]
19. Ramos, L.E.; Furthmüller, J.; Leite, J.R.; Scolfaro, L.M.; Bechstedt, F. Carbon-Based Defects in GaN: Doping Behavior. *Phys. Stat. Sol. B* **2002**, *234*, 864–867. [CrossRef]
20. Eberlein, T.A.G.; Jones, R.; Öberg, S.; Briddon, P.R. Shallow acceptors in GaN. *Appl. Phys. Lett.* **2007**, *91*, 132105. [CrossRef]
21. Wright, A.F. Substitutional and interstitial carbon in wurtzite GaN. *J. Appl. Phys.* **2002**, *92*, 2575–2585. [CrossRef]
22. Neugebauer, J.; Van de Walle, C.G. Gallium vacancies and the yellow luminescence in GaN. *Appl. Phys. Lett.* **1996**, *69*, 503–505. [CrossRef]
23. Fischer, S.; Wetzel, C.; Haller, E.E.; Meyer, B.K. On *p*-type doping in GaN-acceptor binding energies. *Appl. Phys. Lett.* **1995**, *67*, 1298–1300. [CrossRef]
24. Lyons, J.L.; Janotti, A.; Van de Walle, C.G. Carbon impurities and the yellow luminescence in GaN. *Appl. Phys. Lett.* **2010**, *97*, 152108. [CrossRef]
25. Reshchikov, M.A.; Vorobiov, M.; Demchenko, D.O.; Özgür, Ü.; Morkoç, H.; Lesnik, A.; Hoffmann, M.P.; Hörich, F.; Dadgar, A.; Strittmatter, A. Two charge states of the C_N acceptor in GaN: Evidence from photoluminescence. *Phys. Rev. B* **2018**, *98*, 125207. [CrossRef]
26. Narita, T.; Tomita, K.; Tokuda, Y.; Kogiso, T.; Horita, M.; Kachi, T. The origin of carbon-related carrier compensation in *p*-type GaN layers grown by MOVPE. *J. Appl. Phys.* **2018**, *124*, 215701. [CrossRef]
27. Zimmermann, F.; Beyer, J.; Röder, C.; Beyer, F.C.; Richter, E.; Irmscher, K.; Heitmann, J. Current Status of Carbon-Related Luminescence in GaN. *Phys. Stat. Sol. A* **2021**, *218*, 2100235. [CrossRef]
28. Saarinen, K.; Laine, T.; Kuisma, S.; Nissilä, J.; Hautojärvi, P.; Dobrzynski, L.; Baranowski, J.M.; Pakula, K.; Stepniewski, R.; Wojdak, M.; et al. Observation of Native Ga Vacancies in GaN by Positron Annihilation. *Phys. Rev. Lett.* **1997**, *79*, 3030–3033. [CrossRef]
29. Lyons, J.L.; Alkauskas, A.; Janotti, A.; Van de Walle, C.G. First-principles theory of acceptors in nitride semiconductors. *Phys. Stat. Sol. B* **2015**, *252*, 900–908. [CrossRef]
30. Diallo, I.C.; Demchenko, D.O. Native Point Defects in GaN: A Hybrid-Functional Study. *Phys. Rev. Appl.* **2016**, *6*, 064002. [CrossRef]
31. Edwards, A.H.; Schultz, P.A.; Dobzynski, R.M. Electronic structure of intrinsic defects in c-gallium nitride: Density functional theory study without the jellium approximation. *Phys. Rev. B* **2022**, *105*, 235110. [CrossRef]
32. Miceli, G.; Pasquerello, A. Energetics of native point defects in GaN: A density-functional study. *Microelectron. Eng.* **2015**, *147*, 51–54. [CrossRef]
33. Zimmermann, F.; Beyer, J.; Beyer, F.C.; Gärtner, G.; Gamov, I.; Irmscher, K.; Richter, E.; Weyers, M.; Heitmann, J. A carbon-doping related luminescence band in GaN revealed by below bandgap excitation. *J. Appl. Phys.* **2021**, *130*, 055703. [CrossRef]
34. Reshchikov, M.A. Photoluminescence from defects in GaN. In *Gallium Nitride Materials and Devices XVIII*; Fujioka, H., Morkoç, H., Schwarz, U., Eds.; Proceedings SPIE: San Francisco, CA, USA, 2023; Volume 12421, p. 1242109.
35. Reshchikov, M.A. Photoluminescence from Vacancy-Containing Defects in GaN. *Phys. Stat. Sol. A* **2023**, *220*, 2200402. [CrossRef]
36. Vorobiov, M.; Andrieiev, O.; Demchenko, D.O.; Reshchikov, M.A. Nitrogen vacancy-acceptor complexes in GaN. *J. Appl. Phys.* **2024**, *135*, 155701. [CrossRef]
37. Reshchikov, M.A. Red luminescence band in undoped GaN. *J. Lumin.* **2025**, *286*, 121370. [CrossRef]
38. Reshchikov, M.A.; Sayeed, R.M.; Özgür, Ü.; Demchenko, D.O.; McNamara, J.D.; Prozheeva, V.; Tuomisto, F.; Helava, H.; Usikov, A.; Makarov, Y. Unusual properties of the RY3 center in GaN. *Phys. Rev. B* **2019**, *100*, 045204. [CrossRef]
39. Reshchikov, M.A.; Demchenko, D.O.; Ye, D.; Andrieiev, O.; Vorobiov, M.; Grabianska, K.; Zajac, M.; Nita, P.; Iwinska, M.; Bockowski, M.; et al. The effect of annealing on photoluminescence from defects in ammonothermal GaN. *J. Appl. Phys.* **2022**, *131*, 035704. [CrossRef]
40. Reshchikov, M.A.; McNamara, J.D.; Zhang, F.; Monavarian, M.; Usikov, A.; Helava, H.; Makarov, Y.; Morkoç, H. Zero-phonon line and fine structure of the yellow luminescence band in GaN. *Phys. Rev. B* **2016**, *94*, 035201. [CrossRef]
41. Reshchikov, M.A. On the Origin of the Yellow Luminescence Band in GaN. *Phys. Stat. Sol. B* **2023**, *260*, 2200488. [CrossRef]
42. Reshchikov, M.A.; Vorobiov, M.; Grabianska, K.; Zajac, M.; Iwinska, M.; Bockowski, M. Defect-related photoluminescence from ammono GaN. *J. Appl. Phys.* **2021**, *129*, 095703. [CrossRef]

43. Reshchikov, M.A.; Usikov, A.; Helava, H.; Makarov, Y. Fine structure of the red luminescence band in GaN. *Appl. Phys. Lett.* **2014**, *104*, 032103. [CrossRef]
44. Reshchikov, M.A.; McNamara, J.D.; Helava, H.; Usikov, A.; Makarov, Y. Two yellow luminescence bands in GaN. *Sci. Rep.* **2018**, *8*, 8091. [CrossRef]
45. Reshchikov, M.A.; Vorobiov, M.; Andrieiev, O.; Demchenko, D.O.; McEwen, B.; Shahedipour-Sandvik, F. Dual Nature of the Be_{Ga} Acceptor in GaN: Evidence from Photoluminescence. *Phys. Rev. B* **2023**, *108*, 075202. [CrossRef]
46. Reshchikov, M.A.; Bockowski, M. The Origin of the Yellow Luminescence Band in Bulk Be-doped GaN. *Solids* **2024**, *5*, 29–44. [CrossRef]
47. Reshchikov, M.A.; Demchenko, D.O.; McNamara, J.D.; Fernández-Garrido, S.; Calarco, R. Green luminescence in Mg-doped GaN. *Phys. Rev. B* **2014**, *90*, 035207. [CrossRef]
48. Reshchikov, M.A.; Andrieiev, O.; Vorobiov, M.; Demchenko, D.O.; McEwen, B.; Shahedipour-Sandvik, F. Photoluminescence from Cd_{Ga} and Hg_{Ga} acceptors in GaN. *J. Appl. Phys.* **2024**, *135*, 155706. [CrossRef]
49. Reshchikov, M.A.; Demchenko, D.O.; Vorobiov, M.; Andrieiev, O.; McEwen, B.; Shahedipour-Sandvik, F.; Sierakowski, K.; Jaroszynski, P.; Bockowski, M. Photoluminescence related to Ca in GaN. *Phys. Rev. B* **2022**, *106*, 035206. [CrossRef]
50. Reshchikov, M.A.; Shahedipour, F.; Korotkov, R.Y.; Ulmer, M.P.; Wessels, B.W. Photoluminescence band near 2.9 eV in undoped GaN epitaxial layers. *J. Appl. Phys.* **2000**, *87*, 3351–3354. [CrossRef]
51. Demchenko, D.O.; Reshchikov, M.A. Blue luminescence and Zn acceptor in GaN. *Phys. Rev. B* **2013**, *88*, 115204. [CrossRef]
52. Reshchikov, M.A.; Kvasov, A.A.; Bishop, M.F.; McMullen, T.; Usikov, A.; Soukhoveev, V.; Dmitriev, V.A. Tunable and abrupt thermal quenching of photoluminescence in high-resistivity Zn-doped GaN. *Phys. Rev. B* **2011**, *84*, 075212. [CrossRef]
53. Reshchikov, M.A.; Foussekis, M.A.; McNamara, J.D.; Behrends, A.; Bakin, A.; Waag, A. Determination of the absolute internal quantum efficiency of photoluminescence in GaN co-doped with Zn and Si. *J. Appl. Phys.* **2012**, *111*, 073106. [CrossRef]
54. Reshchikov, M.A. Giant shifts of photoluminescence bands in GaN. *J. Appl. Phys.* **2020**, *127*, 055701. [CrossRef]
55. Reshchikov, M.A.; Andrieiev, O.; Vorobiov, M.; McEwen, B.; Shahedipour-Sandvik, F.; Ye, D.; Demchenko, D.O. Stability of the C_NH_i complex and the blue luminescence band in GaN. *Phys. Stat. Sol. B* **2021**, *258*, 2100392. [CrossRef]
56. Reshchikov, M.A. Fine structure of another blue luminescence band in undoped GaN. *Appl. Phys. Lett.* **2019**, *115*, 262102. [CrossRef]
57. Chen, L.; Skromme, B.J. Spectroscopic Characterization of Ion Implanted GaN. *MRS Online Proc. Libr. (OPL)* **2003**, *743*, L11.35. [CrossRef]
58. Ogino, T.; Aoki, M. Photoluminescence in P-doped GaN. *Jpn. J. Appl. Phys.* **1979**, *18*, 1049–1052. [CrossRef]
59. Lagerstedt, O.; Monemar, B. Luminescence in epitaxial GaN:Cd. *J. Appl. Phys.* **1974**, *45*, 2266–2271. [CrossRef]
60. Reshchikov, M.A. Fine Structure of the Carbon-Related Blue Luminescence Band in GaN. *Solids* **2022**, *3*, 231–236. [CrossRef]
61. Reshchikov, M.A.; McEwen, B.; Shahedipour-Sandvik, F. Photoluminescence from Defects in Be-Doped GaN. *Phys. Stat. Sol. B* **2025**, 202400656, *Early View*. [CrossRef]
62. Reshchikov, M.A.; Ghimire, P.; Demchenko, D.O. Magnesium acceptor in gallium nitride: I. Photoluminescence from Mg-doped GaN. *Phys. Rev. B* **2018**, *97*, 20520. [CrossRef]
63. Reshchikov, M.A.; Yi, G.-C.; Wessels, B.W. Behavior of 2.8-and 3.2-eV photoluminescence bands in Mg-doped GaN at different temperatures and excitation densities. *Phys. Rev. B* **1999**, *59*, 13176–13183. [CrossRef]
64. Reshchikov, M.A.; Demchenko, D.O.; McEwen, B.; Shahedipour-Sandvik, F. Identity of the shallowest acceptor in GaN. *Phys. Rev. B* **2025**, *111*, 045202. [CrossRef]
65. Reshchikov, M.A.; McNamara, J.D.; Toporkov, M.; Avrutin, V.; Morkoç, H.; Usikov, A.; Helava, H.; Makarov, Y. Determination of the electron-capture coefficients and the concentration of free electrons in GaN from photoluminescence. *Sci. Rep.* **2016**, *6*, 37511. [CrossRef] [PubMed]
66. Reshchikov, M.A. Measurement and analysis of photoluminescence in GaN. *J. Appl. Phys.* **2021**, *129*, 121101. [CrossRef]
67. Kojima, K.; Ohtomo, T.; Ikemura, K.-I.; Yamazaki, Y.; Saito, M.; Ikeda, H.; Fujito, K.; Chichibu, S.F. Determination of absolute value of quantum efficiency of radiation in high quality GaN single crystals using an integrating sphere. *J. Appl. Phys.* **2016**, *120*, 015704. [CrossRef]
68. Kojima, K.; Ikeda, H.; Fujito, K.; Chichibu, S.F. Demonstration of omnidirectional photoluminescence (ODPL) spectroscopy for precise determination of internal quantum efficiency of radiation in GaN single crystals. *Appl. Phys. Lett.* **2017**, *111*, 032111. [CrossRef]
69. Kojima, K.; Ikemura, K.; Chichibu, S.F. Quantification of the quantum efficiency of radiation of a freestanding GaN crystal placed outside an integrating sphere. *Appl. Phys. Express* **2019**, *12*, 062010. [CrossRef]
70. Kojima, K.; Ikemura, K.; Chichibu, S.F. Temperature dependence of quantum efficiency of radiation for the near-band-edge emission of GaN crystals quantified by omnidirectional photoluminescence spectroscopy. *Appl. Phys. Express* **2020**, *13*, 105504. [CrossRef]

71. Kojima, K.; Chichibu, S.F. Correlation between the internal quantum efficiency and photoluminescence lifetime of the near-band-edge emission in a ZnO single crystal grown by the hydrothermal method. *Appl. Phys. Express* **2020**, *13*, 121005. [CrossRef]
72. Shockley, W.; Read, J.W.T. Statistics of the recombinations of holes and electrons. *Phys. Rev.* **1952**, *87*, 835–842. [CrossRef]
73. Hall, R.N. Germanium rectifier characteristics. *Phys. Rev.* **1951**, *83*, 228.
74. Reshchikov, M.A. Temperature dependence of defect-related photoluminescence in III-V and II-VI semiconductors. *J. Appl. Phys.* **2014**, *115*, 012010. [CrossRef]
75. Reshchikov, M.A. Mechanisms of Thermal Quenching of Defect-Related Luminescence in Semiconductors. *Phys. Stat. Sol. A* **2020**, *218*, 2000101. [CrossRef]
76. Reshchikov, M.A.; Korotkov, R.Y. Analysis of the temperature and excitation intensity dependencies of photoluminescence in undoped GaN films. *Phys. Rev. B* **2001**, *64*, 115205. [CrossRef]
77. Reshchikov, M.A. Time-resolved photoluminescence from defects in GaN. *J. Appl. Phys.* **2014**, *115*, 103503. [CrossRef]
78. Korotkov, R.Y.; Reshchikov, M.A.; Wessels, B.W. Acceptors in undoped GaN studied by transient photoluminescence. *Phys. B* **2003**, *325*, 1–7. [CrossRef]
79. Klasens, H.A. The temperature-dependence of the fluorescence of photoconductors. *J. Phys. Chem. Solids* **1959**, *9*, 185–197. [CrossRef]
80. Reshchikov, M.A. Determination of acceptor concentration in GaN from photoluminescence. *Appl. Phys. Lett.* **2006**, *88*, 202104.
81. Reshchikov, M.A. Internal Quantum Efficiency of Photoluminescence in Wide-Bandgap Semiconductors. In *Photoluminescence: Applications, Types and Efficacy*; Case, M.A., Stout, B.C., Eds.; Nova Science Publishers Inc.: Hauppauge, NY, USA, 2012; pp. 53–120, ISBN 978-1-61942-426-5.
82. Muth, J.F.; Lee, J.H.; Shmagin, I.K.; Kolbas, R.M.; Casey, H.C., Jr.; Keller, B.P.; Mishra, U.K.; DenBaars, S.P. Absorption coefficient, energy gap, exciton binding energy, and recombination lifetime of GaN obtained from transmission measurement. *Appl. Phys. Lett.* **1997**, *71*, 2572–2574. [CrossRef]
83. Reshchikov, M.A.; Usikov, A.; Helava, H.; Makarov, Y.; Prozheeva, V.; Makkonen, I.; Tuomisto, F.; Leach, J.H.; Udwary, K. Evaluation of the concentration of point defects in GaN. *Sci. Rep.* **2017**, *7*, 9297. [CrossRef] [PubMed]
84. Williams, F. Donor-acceptor pairs in semiconductors. *Phys. Stat. Sol.* **1968**, *25*, 493–512. [CrossRef]
85. Thomas, D.G.; Hopfield, J.J.; Augustyniak, W.M. Kinetics of radiative recombination at randomly distributed donors and acceptors. *Phys. Rev.* **1965**, *140*, A202–A220. [CrossRef]
86. Ogino, T.; Aoki, M. Mechanism of Yellow Luminescence in GaN. *Jpn. J. Appl. Phys.* **1980**, *19*, 2395–2405. [CrossRef]
87. Pankove, J.I.; Hutchby, J.A. Photoluminescence of ion-implanted GaN. *J. Appl. Phys.* **1976**, *47*, 5387–5390. [CrossRef]
88. Kucheyev, S.O.; Toth, M.; Phillips, M.R.; Williams, J.S.; Jagadish, C.; Li, G. Chemical origin of the yellow luminescence in GaN. *J. Appl. Phys.* **2002**, *91*, 5867–5874. [CrossRef]
89. Armitage, R.; Hong, W.; Yang, Q.; Feick, H.; Gebauer, J.; Weber, E.R.; Hautakangas, S.; Saarinen, K. Contributions from gallium vacancies and carbon-related defects to the "yellow luminescence" in GaN. *Appl. Phys. Lett.* **2003**, *82*, 3457–3459. [CrossRef]
90. You, W.; Zhang, X.D.; Zhang, L.M.; Yang, Z.; Bian, H.; Ge, Q.; Guo, W.X.; Wang, W.X.; Liu, Z.M. Effects of different ions implantation on yellow luminescence from GaN. *Phys. B* **2008**, *403*, 2666–2670. [CrossRef]
91. Xu, F.J.; Shen, B.; Lu, L.; Miao, Z.L.; Song, J.; Yang, Z.J.; Zhang, G.Y.; Hao, X.P.; Wang, B.Y.; Shen, X.Q.; et al. Different origins of the yellow luminescence in as-grown high-resistance GaN and unintentional-doped GaN films. *J. Appl. Phys.* **2010**, *107*, 023528. [CrossRef]
92. Reurings, F.; Tuomisto, F. Interplay of Ga vacancies, C Impurities and Yellow Luminescence in GaN. In *Gallium Nitride Materials and Devices II*; Morkoç, H., Litton, C.W., Eds.; Proceedings SPIE: San Francisco, CA, USA, 2007; Volume 6473, p. 64730M.
93. Reshchikov, M.A.; Morkoç, H.; Park, S.S.; Lee, K.Y. Photoluminescence study of deep-level defects in undoped GaN. *Mat. Res. Soc. Symp. Proc.* **2002**, *693*, 596–601. [CrossRef]
94. Alkauskas, A.; McCluskey, M.; Van de Walle, C.G. Tutorial: Defects in semiconductors–Combining experiment and theory. *J. Appl. Phys.* **2016**, *119*, 181101. [CrossRef]
95. Reshchikov, M.A.; Albarakati, N.M.; Monavarian, M.; Avrutin, V.; Morkoç, H. Thermal quenching of the yellow luminescence in GaN. *J. Appl. Phys.* **2018**, *123*, 161520. [CrossRef]
96. Matsubara, M.; Bellotti, E. A first-principles study of carbon-related energy levels in GaN. I. Complexes formed by substitutional/imterstitial carbons and gallium/nitrogen vacancies. *J. Appl. Phys.* **2017**, *121*, 195701. [CrossRef]
97. Deak, P.; Lorke, M.; Aradi, B.; Frauenheim, T. Carbon in GaN: Calculations with an optimized hybrid functional. *Phys. Rev. B* **2019**, *99*, 085206. [CrossRef]
98. Christenson, S.G.; Xie, W.; Sun, Y.Y.; Zhang, S.B. Carbon as a source for yellow luminescence in GaN: Isolated C_N defect or its complexes. *J. Appl. Phys.* **2015**, *118*, 135708. [CrossRef]
99. Dreyer, C.E.; Alkauskas, A.; Lyons, J.L.; Van de Walle, C.G. Radiative capture rates at deep defects from electronic structure calculations. *Phys. Rev. B* **2020**, *102*, 085305. [CrossRef]

100. Alkauskas, A.; Yan, Q.; Van de Walle, C.G. First-principles theory of nonradiative carrier capture via multiphonon emission. *Phys. Rev. B* **2014**, *90*, 075202. [CrossRef]
101. Wickramaratne, D.; Dreyer, C.E.; Monserrat, B.; Shen, J.-X.; Lyons, J.L.; Alkauskas, A.; Van de Walle, C.G. Defect identification based on first-principles calculations for deep level transient spectroscopy. *Appl. Phys. Lett.* **2018**, *113*, 192106. [CrossRef]
102. Alkauskas, A.; Lyons, J.L.; Steiauf, D.; Van de Walle, C.G. First-Principles Calculations of Luminescence Spectrum Line Shapes for Defects in Semiconductors: The Example of GaN and ZnO. *Phys. Rev. Lett.* **2012**, *109*, 267401. [CrossRef]
103. Matsubara, M.; Bellotti, E. A first-principles study of carbon-related energy levels in GaN. II. Complexes formed by carbon and hydrogen, silicon or oxygen. *J. Appl. Phys.* **2017**, *121*, 195702. [CrossRef]
104. Reshchikov, M.A.; Demchenko, D.O. Roadmap for Point Defects in GaN. In *Semiconductors and Semimetals*; Mi, Z., Tan, H.H., Eds.; Elsevier: Amsterdam, The Netherlands, 2022; Volume 111, pp. 133–152.
105. Demchenko, D.O.; Diallo, I.C.; Reshchikov, M.A. Yellow luminescence of gallium nitride generated by carbon defect complexes. *Phys. Rev. Lett.* **2013**, *110*, 087404. [CrossRef]
106. Zhang, H.-S.; Shi, L.; Yang, X.-B.; Zhao, Y.-J.; Xu, K.; Wang, L.-W. First-Principles Calculations of Quantum Efficiency for Point Defects in Semiconductors: The Example of Yellow Luminance by GaN: C_N+ O_N and GaN: C_N. *Adv. Opt. Mater.* **2017**, *5*, 1700404. [CrossRef]
107. Lyons, J.L.; Janotti, A.; Van de Walle, C.G. Effects of carbon on the electrical and optical properties of InN, GaN, and AlN. *Phys. Rev. B* **2014**, *89*, 035204. [CrossRef]
108. Tuomisto, F.; Mäki, J.-M.; Zając, M. Vacancy defects in bulk ammonothermal GaN crystals. *J. Cryst. Growth* **2010**, *312*, 2620–2623. [CrossRef]
109. Uedono, A.; Tsukada, Y.; Mikawa, Y.; Mochizuki, T.; Fujisawa, H.; Ikeda, H.; Kurihara, K.; Fujito, K.; Terada, S.; Ishibashi, S.; et al. Vacancies and electron trapping centers in acidic ammonothermal GaN probed by a monoenergetic positron beam. *J. Cryst. Growth* **2016**, *448*, 117–121. [CrossRef]
110. Suihkonen, S.; Pimputkar, S.; Speck, J.S.; Nakamura, S. Infrared absorption of hydrogen-related defects in ammonothermal GaN. *Appl. Phys. Lett.* **2016**, *108*, 202105. [CrossRef]
111. Zajac, M.; Kucharski, R.; Grabianska, K.; Gwardys-Bak, A.; Puchalski, A.; Wasik, D.; Litwin-Staszewska, E.; Piotrzkowski, R.; Domagala, J.Z.; Bockowski, M. Basic ammonothermal growth of Gallium Nitride—State of the art, challenges, perspectives. *Prog. Cryst. Growth Charact. Mater.* **2018**, *64*, 63–74. [CrossRef]
112. Malguth, E.; Hoffmann, A.; Gehloff, W.; Gelhausen, O.; Phillips, M.R.; Xu, X. Structural and electronic properties of Fe^{3+} and Fe^{2+} centers in GaN from optical and EPR experiments. *Phys. Rev. B* **2006**, *74*, 165202. [CrossRef]
113. Tanaka, D.; Iso, K.; Suda, J. Comparative study of electrical properties of semi-insulating GaN substrates grown by hydride vapor phase epitaxy and doped with Fe, C, or Mn. *J. Appl. Phys.* **2023**, *133*, 055701. [CrossRef]
114. Richter, E.; Gridneva, E.; Weyers, M.; Tränkle, G. Fe-doping in hydride vapor-phase epitaxy for semi-insulating gallium nitride. *J. Cryst. Growth* **2016**, *456*, 97–100. [CrossRef]
115. Laaksonen, K.; Ganchenkova, M.G.; Nieminen, R.M. Vacancies in wurtzite GaN and AlN. *J. Phys. Condens. Matter* **2009**, *21*, 015803. [CrossRef]
116. Gao, Y.; Sun, D.; Jiang, X.; Zhao, J. Point defects in group III nitrides: A comparative first-principles study. *J. Appl. Phys.* **2019**, *125*, 215705. [CrossRef]
117. Wang, Q.-J.; Zhang, H.-S.; Shi, L.; Gong, J. Origin of Ga vacancy-related YL center in n-type GaN: A first-principles study. *J. Lumin.* **2023**, *255*, 119561. [CrossRef]
118. Alkauskas, A.; Dreyer, C.E.; Lyons, J.L.; Van de Walle, C.G. Role of excited states in Schockley-Read-Hall recombination in wide-band-gap semiconductors. *Phys. Rev. B* **2016**, *93*, 201304. [CrossRef]
119. Dreyer, C.E.; Alkauskas, A.; Lyons, J.L.; Speck, J.S.; Van de Walle, C.G. Gallium vacancy complexes as a cause of Schockley-Read-Hall recombination in III-nitride light emitters. *Appl. Phys. Lett.* **2016**, *108*, 141101. [CrossRef]
120. Suihkonen, S.; Nykänen, H.; Tanikawa, T.; Yamaguchi, M.; Honda, Y.; Amano, H. Effects of low energy e-beam irradiation on cathodoluminescence from GaN. *Phys. Stat. Sol. A* **2013**, *210*, 383–385. [CrossRef]
121. Huber, M.; Silvestri, M.; Knuuttila, L.; Pozzovivo, G.; Andreev, A.; Kadashchuk, A.; Bonanni, A.; Lundskog, A. Impact of residual carbon impurities and gallium vacancies on trapping effects in AlGaN/GaN metal insulator semiconductor high electron mobility transistors. *Appl. Phys. Lett.* **2015**, *107*, 032106. [CrossRef]
122. Glaser, E.R.; Freitas, J.A., Jr.; Braga, G.C.; Carlos, W.E.; Twigg, M.E.; Wickenden, A.E.; Koleske, D.D.; Henry, R.L.; Leszczynski, M.; Grzegory, I.; et al. Magnetic resonance studies of defects in GaN with reduced dislocation densities. *Phys. B* **2001**, *310*, 51–57. [CrossRef]
123. McNamara, J.D.; Foussekis, M.A.; Baski, A.A.; Li, X.; Avrutin, V.; Morkoç, H.; Leach, J.H.; Paskova, T.; Udwary, K.; Preble, E.; et al. Electrical and optical properties of bulk GaN substrates studied by Kelvin probe and photoluminescence. *Phys. Stat. Sol. C* **2013**, *10*, 536–539.

124. Reshchikov, M.A.; Zhang, M.H.; Cui, J.; Visconti, P.; Yun, F.; Morkoç, H. Photoluminescence study of defects in GaN grown by molecular beam epitaxy. *Mat. Res. Soc. Symp. Proc.* **2001**, *639*, 67. [CrossRef]
125. Reshchikov, M.A.; Molnar, R.; Morkoç, H. Photoluminescence and excitation spectra of deep defects in GaN. *Mat. Res. Soc. Symp. Proc.* **2001**, *680*, E5.6. [CrossRef]
126. Goldys, E.M.; Godlewski, M.; Paskova, T.; Pozina, G.; Monemar, B. Characterization of Red Emission in Nominally Undoped Hydride Vapor Phase Epitaxy. *MRS Internet J. Nitride Semicond. Res.* **2001**, *6*, 1. [CrossRef]
127. Uehara, D.; Kikuchi, M.; Ma, B.; Miyake, H.; Ishitani, Y. Charge transfer processes related to deep levels in free standing n-GaN layer analyzed by above and sub-bandgap energy excitation. *Appl. Phys. Express* **2020**, *13*, 061003. [CrossRef]
128. Wang, L.; Zeimer, U.; Richter, E.; Herms, M.; Weyers, M. Characterisation of free standing GaN grown by HVPE on a $LiAlO_2$ substrate. *Phys. Stat. Sol. A* **2006**, *203*, 1663–1666.
129. Wang, L.; Richter, E.; Weyers, M. Red luminescence from freestanding GaN grown on $LiAlO_2$ substrate by hydride vapor phase epitaxy. *Phys. Stat. Sol. A* **2007**, *204*, 846–849. [CrossRef]
130. Dingle, R. Luminescent transitions associated with divalent copper impurities and the green emission from semiconducting zinc oxide. *Phys. Rev. Lett.* **1969**, *23*, 579–581. [CrossRef]
131. Dahan, P.; Fleurov, V.; Thurian, P.; Heitz, R.; Hoffmann, A.; Broser, I. Properties of the intermediately bound α-, β-, and γ-excitons in ZnO:Cu. *J. Phys. Condens. Matter.* **1998**, *10*, 2007–2019. [CrossRef]
132. Garces, N.Y.; Wang, L.; Bai, L.; Giles, N.C.; Halliburton, L.E. Role of copper in the green luminescence from ZnO crystals. *Appl. Phys. Lett.* **2002**, *81*, 622–624. [CrossRef]
133. Reshchikov, M.A.; Avrutin, V.; Izyumskaya, N.; Shimada, R.; Morkoç, H.; Novak, S.W. About the Cu-related green luminescence band in ZnO. *J. Vac. Sci. Tech. B* **2009**, *27*, 1749–1754. [CrossRef]
134. Kuhnert, R.; Helbig, R. Vibronic structure of the green photoluminescence due to copper impurities in ZnO. *J. Lumin.* **1981**, *26*, 203–206. [CrossRef]
135. Malguth, E.; Hoffmann, A.; Phillips, M.R. Fe in III-V and II-VI semiconductors. *Phys. Stat. Sol. B* **2008**, *245*, 455–480. [CrossRef]
136. Wegscheider, M.; Simbrunner, C.; Przybylinska, H.; Kiecana, M.; Sawicki, M.; Navarro-Quezada, A.; Sitter, H.; Jantsch, W.; Dietl, T.; Bonanni, A. Photoluminescence and Hall studies of GaN:Fe and (Ga,Fe)N:Mg layers. *Phys. Stat. Sol. A* **2007**, *204*, 86–91. [CrossRef]
137. Freitas, J.A., Jr.; Culbertson, J.C.; Glaser, E.R.; Richter, E.; Weyers, M.; Oliveira, A.C.; Garg, V.K. Efficient iron doping of HVPE GaN. *J. Cryst. Growth* **2018**, *500*, 111–116. [CrossRef]
138. Jiang, W.; Nolan, M.; Ehrentraut, D.; D'Evelyn, M.P. Electrical and optical properties of gallium vacancy complexes in ammonothermal GaN. *Appl. Phys. Express* **2017**, *10*, 075506. [CrossRef]
139. Suihkonen, S.; Pimputkar, S.; Sintonen, S.; Tuomisto, F. Defects in single crystalline ammonothermal gallium nitride. *Adv. Electron. Mater.* **2017**, *3*, 1600496. [CrossRef]
140. Reshchikov, M.A.; Morkoç, H.; Park, S.S.; Lee, K.Y. Two charge states of dominant acceptor in unintentionally doped GaN: Evidence from photoluminescence study. *Appl. Phys. Lett.* **2002**, *81*, 4970–4972. [CrossRef]
141. Reshchikov, M.A.; Morkoç, H.; Park, S.S.; Lee, K.Y. Unusual properties of the dominant acceptor in freestanding GaN. *Phys. B* **2003**, *340–342*, 448–451. [CrossRef]
142. Reshchikov, M.A.; Demchenko, D.O.; Usikov, A.; Helava, H.; Makarov, Y. Carbon defects as sources of the yellow and green luminescence bands in undoped GaN. *Phys. Rev. B* **2014**, *90*, 235203. [CrossRef]
143. Reshchikov, M.A.; Usikov, A.; Helava, H.; Makarov, Y. Defect-related luminescence in undoped GaN grown by HVPE. *J. Electron. Mater.* **2015**, *44*, 1281–1286. [CrossRef]
144. Reshchikov, M.A.; McNamara, J.D.; Usikov, A.; Helava, H.; Makarov, Y. Optically-generated giant traps in high-purity GaN. *Phys. Rev. B* **2016**, *93*, 081202. [CrossRef]
145. Lax, M. Cascade Capture of Electrons in Solids. *Phys. Rev.* **1960**, *119*, 1502–1523. [CrossRef]
146. Reshchikov, M.A.; Vorobiov, M.; Andrieiev, A.; Ding, K.; Avrutin, V.; Usikov, A.; Helava, H.; Makarov, Y. Determination of the concentration of impurities in GaN from photoluminescence and secondary-ion mass spectrometry. *Sci. Rep.* **2020**, *10*, 2223. [CrossRef] [PubMed]
147. Takahashi, M.; Tanaka, A.; Ando, Y.; Watanabe, H.; Deki, M.; Kushimoto, M.; Nitta, S.; Honda, Y.; Shima, K.; Kojima, K.; et al. Suppression of Green Luminescence of Mg-Ion-Implanted GaN by Subsequent Implantation of Fluorine Ions at High Temperature. *Phys. Stat. Sol. B* **2020**, *257*, 1900554. [CrossRef]
148. Meyers, V.; Rocco, E.; Hogan, K.; McEwen, B.; Shevelev, M.; Sklyar, V.; Jones, K.; Derenge, M.; Shahedipour-Sandvik, F. P-type conductivity and suppression of green luminescence in Mg/N co-implanted GaN by gyrotron microwave annealing. *J. Appl. Phys.* **2021**, *130*, 085704. [CrossRef]
149. Kojima, K.; Takashima, S.; Edo, M.; Ueno, K.; Shimizu, M.; Takahashi, T.; Ishibashi, S.; Uedono, A.; Chichibu, S.F. Nitrogen vacancies as a common element of the green luminescence and nonradiative recombination centers in Mg-implanted GaN layers formed on a GaN substrate. *Appl. Phys. Express* **2017**, *10*, 061002. [CrossRef]

150. Vorobiov, M.; Andrieiev, O.; Demchenko, D.O.; Reshchikov, M.A. Point Defects in Beryllium Doped GaN. *Phys. Rev. B* **2021**, *104*, 245203. [CrossRef]
151. Reshchikov, M.A.; Andrieiev, O.; Vorobiov, M.; Ye, D.; Demchenko, D.O.; Sierakowski, K.; Bockowski, M.; McEwen, B.; Meyers, V.; Shahedipour-Sandvik, F. Thermal annealing of GaN implanted with Be. *J. Appl. Phys.* **2022**, *131*, 125704. [CrossRef]
152. Reshchikov, M.A.; Morkoç, H. Unusual Properties of the Red and Green Luminescence Bands in Ga-rich GaN. *MRS Online Proc. Libr. (OPL)* **2005**, *831*, E3.7. [CrossRef]
153. Reshchikov, M.A.; He, L.; Molnar, R.J.; Park, S.S.; Lee, K.Y.; Morkoç, H. Aquamarine luminescence band in undoped GaN. *MRS Online Proc. Libr.* **2005**, *831*, 537–542. [CrossRef]
154. Reshchikov, M.A.; Yun, F.; Huang, D.; He, L.; Morkoç, H.; Park, S.S.; Lee, K.Y. Photoluminescence of GaN grown by molecular beam epitaxy on freestanding GaN template. *MRS Online Proc. Libr.* **2002**, *722*, 14. [CrossRef]
155. Young, E.C.; Grandjean, N.; Mates, T.E.; Speck, J.S. Calcium impurity as a source of non-radiative recombination in (In,Ga)N layers grown by molecular beam epitaxy. *Appl. Phys. Lett.* **2016**, *109*, 212103. [CrossRef]
156. Chèze, C.; Feix, F.; Lahnemann, J.; Flissikowski, T.; Krysko, M.; Wolny, P.; Turski, H.; Skierbiszewski, C.; Brandt, O. Luminescent N-polar (In,Ga)N/GaN quantum wells achieved by plasma-assisted molecular beam epitaxy at temperatures exceeding 700 °C. *Appl. Phys. Lett.* **2018**, *112*, 022102. [CrossRef]
157. Auzelle, T.; Sinito, C.; Lähnemann, J.; Gao, G.; Flissikowski, T.; Trampert, A.; Brandt, O.; Fernández-Garrido, S. Interface Recombination in Ga- and N-Polar GaN/(Al,Ga)N Quantum Wells Grown by Molecular Beam Epitaxy. *Phys. Rev. Appl.* **2022**, *17*, 044030. [CrossRef]
158. Zacks, E.; Halperin, A. Dependence of the Peak Energy of the Pair-Photoluminescence Band on Excitation Intensity. *Phys. Rev. B* **1972**, *6*, 3072–3075. [CrossRef]
159. Xu, S.J.; Li, G.; Chua, S.J.; Wang, X.C.; Wang, W. Observation of optically-active metastable defects in undoped GaN epilayers. *Appl. Phys. Lett.* **1998**, *72*, 2451–2453. [CrossRef]
160. Brown, S.A.; Reeves, R.J.; Haase, C.S.; Cheung, R.; Kirchner, C.; Kamp, M. Reactive-ion-etched gallium nitride: Metastable defects and yellow luminescence. *Appl. Phys. Lett.* **1999**, *75*, 3285–3287. [CrossRef]
161. Kim, B.; Kuskovsky, I.; Herman, I.P.; Li, D.; Neumark, G.F. Reversible ultraviolet-induced photoluminescence degradation and enhancement in GaN films. *J. Appl. Phys.* **1999**, *86*, 2034–2037. [CrossRef]
162. Dhar, S.; Ghosh, S. Optical metastability in undoped GaN grown on Ga-rich GaN buffer layers. *Appl. Phys. Lett.* **2002**, *80*, 4519–4521. [CrossRef]
163. Ryan, B.J.; Henry, M.O.; McGlynn, E.; Fryar, J. Investigation of optical metastability in GaN using photoluminescence spectroscopy. *Phys. B Condens. Matt.* **2003**, *340–342*, 452–456. [CrossRef]
164. Reshchikov, M.A.; Moon, Y.T.; Morkoç, H. Origin of unstable photoluminescence in GaN: Metastable defects or surface states? *Phys. Stat. Sol. C* **2005**, *2*, 2716–2719. [CrossRef]
165. Monemar, B.; Paskov, P.P.; Pozina, G.; Hemmingsson, C.; Bergman, J.P.; Khromov, S.; Izyumskaya, V.N.; Avrutin, V.; Li, X.; Morkoç, H.; et al. Properties of the main Mg-related acceptors in GaN from optical and structural studies. *J. Appl. Phys.* **2014**, *115*, 053507. [CrossRef]
166. Glaser, E.R.; Freitas, J.A., Jr.; Shanabrook, B.V.; Koleske, D.D.; Lee, S.K.; Park, S.S.; Han, J.Y. Optically detected magnetic resonance of (effective-mass) shallow acceptors in Si-doped GaN homoepitaxial layers. *Phys. Rev. B* **2003**, *68*, 195201. [CrossRef]
167. Murthy, M.; Freitas, J.A., Jr.; Kim, J.; Glaser, E.R.; Storm, D. Residual impurities in GaN substrates and epitaxial layers grown by various techniques. *J. Cryst. Growth* **2007**, *305*, 393–398. [CrossRef]
168. Kamiura, Y.; Ogasawara, M.; Fukutani, K.; Ishiyama, T.; Yamashita, Y.; Mitani, T.; Mukai, T. Enhancement of blue emission from GaN films and diodes by water vapor remote plasma treatment. *Phys. B* **2007**, *401–402*, 331–334. [CrossRef]
169. Glaser, E.R.; Murthy, M.; Freitas, J.A., Jr.; Storm, D.F.; Zhou, L.; Smith, D.J. Optical and magnetic resonance studies of Mg-doped GaN homoepitaxial layers grown by molecular beam epitaxy. *Phys. B* **2007**, *401–402*, 327–330. [CrossRef]
170. Lyons, J.L.; Janotti, A.; Van de Walle, C.G. Effects of hole localization on limiting *p*-type conductivity in oxide and nitride semiconductors. *J. Appl. Phys.* **2014**, *115*, 012014. [CrossRef]
171. Saarinen, K.; Suski, T.; Grzegory, I.; Look, D.C. Thermal stability of isolated and complexed Ga vacancies in GaN bulk crystals. *Phys. Rev. B* **2001**, *64*, 233201. [CrossRef]
172. Tuomisto, F.; Mäki, J.-M.; Rauch, C.; Makkonen, I. On the formation of vacancy defects in III-nitride semiconductors. *J. Cryst. Growth* **2012**, *350*, 93–97. [CrossRef]
173. Oila, J.; Kivioja, J.; Ranki, V.; Saarinen, K.; Look, D.C.; Molnar, R.J.; Park, S.S.; Lee, S.K.; Han, J.Y. Ga vacancies as dominant intrinsic acceptors in GaN grown by hydride vapor phase epitaxy. *App. Phys. Lett.* **2003**, *82*, 3433–3435. [CrossRef]
174. Tuomisto, F.; Hautakangas, S.; Makkonen, I.; Ranki, V.; Puska, M.J.; Saarinen, K.; Bockowski, M.; Suski, T.; Paskova, T.; Monemar, B.; et al. Dissociation of V_{Ga}-O_N complexes in HVPE GaN by high pressure and high temperature annealing. *Phys. Stat. Sol. B* **2006**, *243*, 1436–1440. [CrossRef]

175. Tuomisto, F.; Saarinen, K.; Paskova, T.; Monemar, B.; Bockowski, M.; Suski, T. Thermal stability of in-grown vacancy defects in GaN grown by hydride vapor phase epitaxy. *J. Appl. Phys.* **2006**, *99*, 066105. [CrossRef]
176. Prozheev, I.; Iwinska, M.; Sochacki, T.; Bockowski, M.; Bes, R.; Tuomisto, F. Origins of Electrical Compensation in Si-doped HVPE GaN. *Phys. Stat. Sol. B* **2023**, *260*, 2200568. [CrossRef]
177. Hautakangas, S.; Makkonen, I.; Ranki, V.; Puska, M.J.; Saarinen, K.; Xu, X.; Look, D.C. Direct evidence of impurity decoration of Ga vacancies in GaN from positron annihilation spectroscopy. *Phys. Rev. B* **2006**, *73*, 193301. [CrossRef]
178. Nykänen, H.; Suihkonen, S.; Kilanski, L.; Sopanen, M.; Tuomisto, F. Low energy beam induced vacancy activation in GaN. *Appl. Phys. Lett.* **2012**, *100*, 122105. [CrossRef]
179. Chichibu, S.F.; Shima, K.; Uedono, A.; Ishibashi, S.; Iguchi, H.; Narita, T.; Kataoka, K.; Tanaka, R.; Takashima, S.; Ueno, K.; et al. Impacts of vacancy complexes on the room-temperature photoluminescence lifetimes of state-of-the-art GaN substrates, epitaxial layers, and Mg-implanted layers. *J. Appl. Phys.* **2024**, *135*, 185701. [CrossRef]
180. Uedono, A.; Takino, J.; Sumi, T.; Okayama, Y.; Imanishi, M.; Ishibashi, S.; Mori, Y. Vacancy-type defects in bulk GaN grown by oxide vapor phase epitaxy probed using positron annihilation. *J. Cryst. Growth* **2021**, *570*, 126219. [CrossRef]
181. Li, H.; Huang, M.; Chen, S. First-principles exploration of defect-pairs in GaN. *J. Semicond.* **2020**, *41*, 032104. [CrossRef]
182. Jiang, H.; Wan, P.; Yang, J.; Xu, X.; Li, W.; Li, X. Analysis of radiation defects in gallium nitride using deep level transient spectra and first principles methods. *Nuclar Instr. Meth. Phys. Res. B* **2023**, *545*, 105120. [CrossRef]
183. Linde, M.; Uftring, S.J.; Watkins, G.D.; Härle, V.; Scholz, F. Optical detection of magnetic resonance in electron-irradiated GaN. *Phys. Rev. B* **1997**, *55*, 10177–10180. [CrossRef]
184. Kogiso, T.; Narita, T.; Yoshida, H.; Tokuda, Y.; Tomita, K.; Kachi, T. Characterization of hole traps in MOVPE-grown p-GaN layers using low-frequency capacitance deep-level transient spectroscopy. *Jap. J. Appl. Phys.* **2019**, *58*, SCCB36. [CrossRef]
185. Zhao, F.; Guan, H.; Turiansky, M.E.; Van de Walle, C.G. Carbon in GaN as a nonradiative recombination center. *Appl. Phys. Lett.* **2025**, *126*, 201106. [CrossRef]
186. Neugebauer, J.; Van de Walle, C.G. Hydrogen in GaN: Novel Aspects of a Common Impurity. *Phys. Rev. Lett.* **1995**, *75*, 4452–4455. [CrossRef] [PubMed]
187. Limpijumnong, S.; Van de Walle, C.G. Stability, diffusivity, and vibrational properties of monoatomic and molecular hydrogen in wurtzite GaN. *Phys. Rev. B* **2003**, *68*, 235203. [CrossRef]
188. Reshchikov, M.A.; Andrieiev, O.; Vorobiov, M.; Ye, D.; Demchenko, D.O.; McEwen, B.; Shahedipour-Sandvik, F. Passivation of defects in GaN by hydrogen and their activation by annealing. *Nanotechnology* **2025**, *36*, 105704. [CrossRef]
189. Demchenko, D.O.; Diallo, I.C.; Reshchikov, M.A. Hydrogen-carbon complexes and the blue luminescence band in GaN. *J. Appl. Phys.* **2016**, *119*, 035702. [CrossRef]
190. Wu, S.; Yang, X.; Zhang, Q.; Shang, Q.; Huang, H.; Shen, J.; He, X.; Xu, F.; Wang, X.; Ge, W.; et al. Direct evidence of hydrogen interaction with carbon: C-H complex in semi-insulating GaN. *Appl. Phys. Lett.* **2020**, *116*, 262101. [CrossRef]
191. Richter, E.; Beyer, F.C.; Zimmermann, F.; Gärtner, G.; Irmscher, K.; Gamov, I.; Heitmann, J.; Weyers, M.; Tränkle, G. Growth and Properties of Intentionally Carbon-Doped GaN Layers. *Cryst. Res. Technol.* **2020**, *55*, 1900129. [CrossRef]
192. Gamov, I.; Richter, E.; Weyers, M.; Gärtner, G.; Irmscher, K. Carbon doping of GaN: Proof of the formation of electrically active tri-carbon defects. *J. Appl. Phys.* **2020**, *127*, 205701. [CrossRef]
193. Reuter, E.E.; Zhang, R.; Kuech, T.F.; Bishop, S.G. Photoluminescence excitation spectroscopy of carbon-doped gallium nitride. *MRS Internet J. Nitride Semicond. Res.* **1999**, *4S1*, G3.67. [CrossRef]
194. Stoneham, A.M. *Theory of Defects in Solids*; Oxford University Press: New York, NY, USA, 1975; 955p.
195. Baldacchini, G. Radiative and nonradiative processes in color centers. In *Advances in Nonradiative Processes in Solids*; Di Bartolo, B., Ed.; Plenum Press: New York, NY, USA, 1991; pp. 219–259.
196. Asami, K.; Naka, T.; Ishiguro, M. Luminescence quenching in F centers under pressure. *Phys. Rev. B* **1986**, *34*, 5658–5664. [CrossRef] [PubMed]
197. Swank, R.K.; Brown, F.C. Lifetime of the Excited F Center. *Phys. Rev.* **1963**, *130*, 34–41. [CrossRef]
198. Timusk, T.; Martienssen, W. Recombination Luminescence in Alkali Halides. *Phys. Rev.* **1962**, *128*, 1656–1663. [CrossRef]
199. Sánchez, F.J.; Calle, F.; Sánchez-Garcia, M.A.; Calleja, E.; Munoz, E.; Molloy, C.H.; Somerford, D.J.; Serrano, J.J.; Blanco, J.M. Experimental evidence for a Be shallow acceptor in GaN grown on Si(111) by molecular beam epitaxy. *Semicond. Sci. Technol.* **1998**, *13*, 1130–1133. [CrossRef]
200. Jaworek, M.; Wysmolek, A.; Kaminska, M.; Twardowski, A.; Bockowski, M.; Grzegory, I. Photoluminescence study of bulk GaN doped with beryllium. *Acta Phys. Pol.* **2005**, *108*, 705–710. [CrossRef]
201. Kawaharazuka, A.; Tanimoto, T.; Nagai, K.; Tanaka, Y.; Horikoshi, Y. Be and Mg co-doping in GaN. *J. Cryst. Growth* **2007**, *301–302*, 414. [CrossRef]
202. Teisseyre, H.; Gorczyca, I.; Christensen, N.E.; Svane, A.; Naranjo, F.B.; Calleja, E. Pressure behavior of beryllium-acceptor level in gallium nitride. *J. Appl. Phys.* **2005**, *97*, 043704. [CrossRef]

203. Al Tahtamouni, T.M.; Sedhain, A.; Lin, J.Y.; Jiang, H.X. Beryllium Doped *p*-type GaN Grown by Metal-Organic Chemical Vapor Deposition. *Jordan. J. Phys.* **2010**, *3*, 77–81.
204. Van de Walle, C.G.; Limpijumnong, S. First-Principles studies of beryllium doping of GaN. *Phys. Rev. B* **2001**, *63*, 245205. [CrossRef]
205. Wang, H.; Chen, A.-B. Calculations of acceptor ionization energies in GaN. *Phys. Rev. B* **2001**, *63*, 125212. [CrossRef]
206. Lany, S.; Zunger, A. Dual nature of acceptors in GaN and ZnO: The curious case of the shallow Mg_{Ga} deep state. *Appl. Phys. Lett.* **2010**, *96*, 142114. [CrossRef]
207. Lyons, J.L.; Janotti, A.; Van de Walle, C.G. Impact of group-II acceptors on the electrical and optical properties of GaN. *Jap. J. Appl. Phys.* **2013**, *52*, 08JJ04. [CrossRef]
208. Cai, X.; Yang, J.; Zhang, P.; Wei, S.-H. Origin of Deep Be Acceptor Levels in Nitride Semiconductors: The Roles of Chemical and Strain Effects. *Phys. Rev. Appl.* **2019**, *11*, 034019. [CrossRef]
209. Jin, S.; Li, X.; Yang, W.; Zhao, Y.; Bian, L.; Lu, S. Electrical and optical properties of Beryllium Deep Acceptors in GaN. *J. Electron. Mater.* **2020**, *49*, 7472–7478. [CrossRef]
210. Demchenko, D.O.; Vorobiov, M.; Andrieiev, O.; Myers, T.H.; Reshchikov, M.A. Shallow and deep states of beryllium acceptor in GaN: Why photoluminescence experiments do not reveal small polarons for defects in semiconductors. *Phys. Rev. Lett.* **2021**, *126*, 027401. [CrossRef]
211. Teisseyre, H.; Lyons, J.L.; Kaminska, A.; Jankowski, D.; Jarosz, D.; Bockowski, M.; Suchocki, A.; Van de Walle, C.G. Identification of yellow luminescence centers in Be-doped GaN through pressure-dependent studies. *J. Phys. D: Appl. Phys.* **2017**, *50*, 22LT03. [CrossRef]
212. Naranjo, F.B.; Sánchez-García, M.A.; Pau, J.L.; Jiménez, A.; Calleja, E.; Muñoz, E.; Oila, J.; Saarinen, K.; Hautojärvi, P. Study of the Effects of Mg and Be Co-doping in GaN Layers. *Phys. Stat. Sol. A* **2000**, *180*, 97–102. [CrossRef]
213. Reshchikov, M.A.; Vorobiov, M.; Andrieiev, O.; McEwen, B.; Rocco, E.; Meyers, V.; Demchenko, D.O.; Shahedipour-Sandvik, F. Photoluminescence from Be-Doped GaN Grown by Metal-Organic Chemical Vapor Deposition. *Phys. Stat. Sol. B* **2023**, *260*, 2200487. [CrossRef]
214. Reshchikov, M.A.; Andrieiev, O.; Vorobiov, M.; Demchenko, D.O.; McEwen, B.; Shahedipour-Sandvik, F. Photoluminescence from GaN implanted with Be and F. *Phys. Stat. Sol. B* **2023**, *260*, 2300131. [CrossRef]
215. Zajac, M.; Reshchikov, M.A.; McEwen, B.; Shahendipour-Sandvik, F. P-type conductivity in GaN:Be epitaxial layers. *J. Appl. Phys.* **2025**, *138*, 095705. [CrossRef]
216. Glaser, E.R.; Carlos, W.; Braga, G.; Freitas, J.; Moore, W.; Shanabrook, B.; Wickenden, A.; Koleske, D.; Henry, R.; Bayerl, M.; et al. Characterization of nitrides by electron paramagnetic resonance (EPR) and optically detected magnetic resonance (ODMR). *Mater. Sci. Eng. B* **2002**, *93*, 39–48. [CrossRef]
217. Reshchikov, M.A.; Sierakowski, K.; Jakiela, R.; Fijalkowski, M.; Sochacki, T.; Demchenko, D.O.; Bockowski, M. Photoluminescence from a- and m-plane GaN:Be,O. In Proceedings of the International Conference on Nitride Semiconductors (ICNS-15), Malmö, Sweden, 6–11 July 2025.
218. Takeya, M.; Ikeda, M. Novel Methods of p-type Activation in Mg-doped GaN. *Jpn. J. Appl. Phys.* **2001**, *40*, 6260–6262. [CrossRef]
219. Demchenko, D.O.; Reshchikov, M.A. Passivation of the beryllium acceptor in GaN and a possible route for p-type doping. *Appl. Phys. Lett.* **2021**, *118*, 142103. [CrossRef]
220. Maruska, H.P.; Stevenson, D.A.; Pankove, J.I. Violet luminescence of Mg-doped GaN. *Appl. Phys. Lett.* **1973**, *22*, 303–305. [CrossRef]
221. Amano, H.; Kito, M.; Hiramatsu, K.; Akasaki, I. P-Type Conduction in Mg-Doped GaN Treated with Low-Energy Electron Beam Irradiation (LEEBI). *Jap. J. Appl. Phys.* **1989**, *28*, L2112–L2114. [CrossRef]
222. Nakamura, S.; Mukai, T.; Senoh, M. Candela-class high-brightness InGaN/AIGaN double-heterostructure blue-light-emitting diodes. *Appl. Phys. Lett.* **1994**, *64*, 1687–1689. [CrossRef]
223. Akasaki, I.; Amano, H.; Kito, M.; Hiramatsu, K. Photoluminescence of Mg-doped p-type GaN and electroluminescence of GaN p-n junction LED. *J. Lumin.* **1991**, *48–49*, 666–670. [CrossRef]
224. Amano, H.; Kito, M.; Hiramatsu, K.; Akasaki, I. Growth and Luminescence Properties of Mg- Doped GaN Prepared by MOVPE. *J. Electrochem. Soc.* **1990**, *137*, 1639–1641. [CrossRef]
225. Nakamura, S.; Mukai, T.; Senoh, M.; Iwasa, N. Thermal annealing effects on p-type Mg-doped GaN films. *Jpn. J. Appl. Phys.* **1992**, *31 Pt 2*, L139–L142. [CrossRef]
226. Nakamura, S.; Iwasa, N.; Senoh, M.; Mukai, T. Hole compensation mechanism of p-type GaN films. *Jpn. J. Appl. Phys.* **1992**, *31 Pt 2*, 1258–1266. [CrossRef]
227. Kaufmann, U.; Kunzer, M.; Maier, M.; Obloh, H.; Ramakrishnan, A.; Santic, B. Nature of the 2.8 eV photoluminescence band in Mg doped GaN. *Appl. Phys. Lett.* **1998**, *72*, 1326–1328. [CrossRef]

228. Eckey, L.; Von Gfug, U.; Holst, J.; Hoffmann, A.; Kaschner, A.; Siegle, H.; Thomsen, C.; Schineller, B.; Heime, K.; Heuken, M.; et al. Photoluminescence and Raman study of compensation effects in Mg-doped GaN epilayers. *J. Appl. Phys.* **1998**, *84*, 5828–5830. [CrossRef]
229. Bhattacharyya, A.; Li, W.; Cabalu, J.; Moustakas, T.D.; Smith, D.J.; Hervig, R.L. Efficient p-type doping of GaN films by plasma-assisted molecular beam epitaxy. *Appl. Phys. Lett.* **2004**, *85*, 4956–4958. [CrossRef]
230. Fischer, A.M.; Wang, S.; Ponce, F.A.; Gunning, B.P.; Fabien, C.A.; Doolittle, W.A. Origin of high hole concentrations in Mg-doped GaN films. *Phys. Stat. Sol. B* **2017**, *254*, 1600668. [CrossRef]
231. Sun, Y.Y.; Abtew, A.; Zhang, P.; Zhang, S.B. Anisotropic polaron localization and spontaneous symmetry breaking: Comparison of cation-site acceptors in GaN and ZnO. *Phys. Rev. B.* **2014**, *90*, 165301. [CrossRef]
232. Demchenko, D.O.; Diallo, I.; Reshchikov, M.A. Magnesium acceptor in gallium nitride: II. Koopmans tuned HSE hybrid functional calculations of dual nature and optical properties. *Phys. Rev. B* **2018**, *97*, 205205. [CrossRef]
233. Lyons, J.L.; Janotti, A.; Van de Walle, C.G. Shallow versus Deep Nature of Mg Acceptors in Nitride Semiconductors. *Phys. Rev. Lett.* **2012**, *108*, 156403. [CrossRef] [PubMed]
234. Miceli, G.; Pasquarello, A. Self-compensation due to point defects in Mg-doped GaN. *Phys. Rev. B* **2016**, *93*, 165207. [CrossRef]
235. Demchenko, D.O.; Vorobiov, M.; Andrieiev, O.; Reshchikov, M.A.; McEwen, B.; Shahedipour-Sandvik, F. Koopmans-tuned Heyd-Scuseria-Ernzerhof hybrid functional calculations of acceptors in GaN. *Phys. Rev. B* **2024**, *110*, 035203. [CrossRef]
236. Monemar, B.; Paskov, P.P.; Pozina, G.; Hemmingsson, C.; Bergman, J.P.; Kawashima, T.; Amano, H.; Akasaki, I.; Paskova, T.; Figge, S.; et al. Evidence for Two Mg Related Acceptors in GaN. *Phys. Rev. Lett.* **2009**, *102*, 235501. [CrossRef]
237. Pozina, G.; Hemmingsson, C.; Paskov, P.P.; Bergman, J.P.; Monemar, B.; Kawashima, T.; Amano, H.; Akasaki, I.; Usui, A. Effect of annealing on metastable shallow acceptors in Mg-doped GaN layers grown on GaN substrates. *Appl. Phys. Lett.* **2008**, *92*, 151904. [CrossRef]
238. Gelhausen, O.; Phillips, M.R.; Goldys, E.M.; Paskova, T.; Monemar, B.; Strassburg, M.; Hoffmann, A. Dissociation of H-related defect complexes in Mg-doped GaN. *Phys. Rev. B* **2004**, *69*, 125210. [CrossRef]
239. Pozina, G.; Paskov, P.P.; Bergman, J.P.; Hemmingsson, C.; Hultman, L.; Monemar, B.; Amano, H.; Akasaki, I.; Usui, A. Metastable behavior of the UV luminescence in Mg-doped GaN layers grown on quasibulk GaN templates. *Appl. Phys. Lett.* **2007**, *91*, 221901. [CrossRef]
240. Callsen, G.; Wagner, M.R.; Kure, T.; Reparaz, J.S.; Bügler, M.; Brunnmeier, J.; Nenstiel, C.; Hoffmann, A.; Hoffmann, M.; Tweedie, J.; et al. Optical signature of Mg-doped GaN: Transfer processes. *Phys. Rev. B* **2012**, *86*, 075207. [CrossRef]
241. Liu, H.; Su, P.-Y.; Wu, Z.; Liu, R.; Ponce, F.A. Influence of substrate misorientation on the optical properties of Mg-doped GaN. *J. Appl. Phys.* **2020**, *127*, 195701. [CrossRef]
242. Levanyuk, A.P.; Osipov, V.V. Edge luminescence of direct-gap semiconductors. *Sov. Phys. Usp.* **1981**, *24*, 187–215. [CrossRef]
243. Takahashi, M.; Tanaka, A.; Ando, Y.; Watanabe, H.; Deki, M.; Kushimoto, M.; Nitta, S.; Honda, Y.; Shima, K.; Kojima, K.; et al. Impact of high-temperature implantation of Mg ions into GaN. *Jap. J. Appl. Phys.* **2020**, *59*, 056502. [CrossRef]
244. Kumar, A.; Yi, W.; Uzuhashi, J.; Ohkubo, T.; Chen, J.; Sekiguchi, T.; Tanaka, R.; Takashima, S.; Edo, M.; Hono, K. Influence of implanted Mg concentration on defects and Mg distribution in GaN. *J. Appl. Phys.* **2020**, *128*, 065701. [CrossRef]
245. Itoh, Y.; Watanabe, H.; Ando, Y.; Kano, E.; Deki, M.; Nitta, S.; Honda, Y.; Tanaka, A.; Ikarashi, N.; Amano, H. Effect of beam current on defect formation by high-temperature implantation of Mg ions into GaN. *Appl. Phys. Express* **2022**, *15*, 021003. [CrossRef]
246. Sukarai, H.; Omori, M.; Yamada, S.; Furukawa, Y.; Suzuki, H.; Narita, T.; Kataoka, K.; Horita, M.; Bockowski, M.; Suda, J.; et al. Highly effective activation of Mg-implanted p-type GaN by ultra-high-pressure annealing. *Appl. Phys. Lett.* **2019**, *115*, 142104. [CrossRef]
247. Tsuge, H.; Ikeda, K.; Kato, S.; Nishimura, T.; Nakamura, T.; Kuriyama, K.; Mishima, T. Impact of Mg-ion implantation with various fluence ranges on optical properties of n-type GaN. *Nucl. Instr. Meth. Phys. Res. B* **2017**, *409*, 50–52. [CrossRef]
248. Uedono, A.; Iguchi, H.; Narita, T.; Kataoka, K.; Egger, W.; Koschine, T.; Hugenschmidt, C.; Dickmann, M.; Shima, K.; Kojima, K.; et al. Annealing Behavior of Vacancy-Type Defects in Mg- and H-Implanted GaN Studied Using Monoenergetic Positron Beams. *Phys. Stat. Sol. B* **2019**, *256*, 1900104. [CrossRef]
249. Monemar, B.; Paskov, P.P.; Bergman, J.P.; Paskova, T.; Figge, S.; Dennemarck, J.; Hommel, D. The dominant shallow 0.225 eV acceptor in GaN. *Phys. Stat. Sol. B* **2006**, *243*, 1604–1608. [CrossRef]
250. Kamiura, Y.; Kaneshiro, M.; Tamura, J.; Ishiyama, T.; Yamashita, Y.; Mitani, T.; Mukai, T. Enhancement of blue emission from Mg-doped GaN using remote plasma containing atomic hydrogen. *Jap. J. Appl. Phys.* **2005**, *44*, L926–L928. [CrossRef]
251. Alves, H.; Leiter, F.; Pfisterer, D.; Hofmann, D.M.; Meyer, B.K.; Einfeld, S.; Heinke, H.; Hommel, D. Mg in GaN: The structure of the acceptor and the electrical activity. *Phys. Stat. Sol. C* **2003**, 1770–1782. [CrossRef]
252. Shahedipour, F.; Wessels, B.W. Investigation of the formation of the 2.8 eV luminescence band in p-type GaN:Mg. *Appl. Phys. Lett.* **2000**, *76*, 3011–3013. [CrossRef]
253. Nayak, S.; Gupta, M.; Waghmare, U.V.; Shivaprasad, S.M. Origin of Blue Luminescence in Mg-Doped GaN. *Phys. Rev. Appl.* **2019**, *11*, 014027. [CrossRef]

254. Yan, Q.; Janotti, A.; Scheffler, M.; Van de Walle, C.G. Role of nitrogen vacancies in the luminescence of Mg-doped GaN. *Appl. Phys. Lett.* **2012**, *100*, 142110. [CrossRef]
255. Shklovskii, B.I.; Efros, A.L. *Electronic Properties of Doped Semiconductors*; Springer: Berlin/Heidelberg, Germany, 1984; pp. 53–73, 253–313.
256. Zeng, S.; Aliev, G.N.; Wolverson, D.; Davies, J.J.; Bingham, S.J.; Abdulmalik, D.A.; Coleman, P.G.; Wang, T.; Parbrook, P.J. The role of vacancies in the red luminescence from Mg-doped GaN. *Phys. Stat. Sol. C* **2006**, *3*, 1919–1922. [CrossRef]
257. Shima, K.; Tanaka, R.; Takashima, S.; Ueno, K.; Edo, M.; Kojima, K.; Uedono, A.; Ishibashi, S.; Chichibu, S.F. Improved minority carrier lifetime in p-type GaN segments prepared by vacancy-guided redistribution of Mg. *Appl. Phys. Lett.* **2021**, *119*, 182106. [CrossRef]
258. Bayerl, M.W.; Brandt, M.S.; Glaser, E.R.; Wickenden, A.E.; Koleske, D.D.; Henry, R.L.; Stutzmann, M. The Origin of Red Luminescence from Mg-doped GaN. *Phys. Stat. Sol. B* **1999**, *216*, 547–550. [CrossRef]
259. Bayerl, M.W.; Brandt, M.S.; Ambacher, O.; Stutzmann, M.; Glaser, E.R.; Henry, R.L.; Wickenden, A.E.; Koleske, D.D.; Suski, T.; Grzegory, I.; et al. Optically detected magnetic resonance of red and near-infrared luminescence in Mg-doped GaN. *Phys. Rev. B* **2001**, *63*, 125203. [CrossRef]
260. Zajac, M.; Konczewicz, L.; Litwin-Staszewska, E.; Iwinska, M.; Kucharski, R.; Juillaguet, S.; Contreras, S. P-type conductivity in GaN:Zn monocrystals grown by ammonothermal method. *J. Appl. Phys.* **2021**, *129*, 135702. [CrossRef]
261. Reshchikov, M.A. Two-step thermal quenching of photoluminescence in Zn-doped GaN. *Phys. Rev. B* **2012**, *85*, 245203. [CrossRef]
262. Reshchikov, M.A.; Olsen, A.J.; Bishop, M.F.; McMullen, T. Superlinear increase of photoluminescence with excitation intensity in Zn-doped GaN. *Phys. Rev. B.* **2013**, *88*, 075204. [CrossRef]
263. Monemar, B.; Lagerstedt, O.; Gislason, H.P. Properties of Zn-doped VPE-grown GaN. I. Luminescence data in relation to doping conditions. *J. Appl. Phys.* **1980**, *51*, 625–639. [CrossRef]
264. Pankove, J.I. Luminescence in GaN. *J. Lumin.* **1973**, *7*, 114–126. [CrossRef]
265. Shi, L.; Xu, K.; Wang, L.-W. Comparative study of ab initio nonradiative recombination rate calculations under different formalisms. *Phys. Rev. B* **2015**, *91*, 205315. [CrossRef]
266. Bergman, P.; Ying, G.; Monemar, B.; Holtz, P.O. Time-resolved spectroscopy of Zn- and Cd-doped GaN. *J. Appl. Phys.* **1987**, *61*, 4589–4592. [CrossRef]
267. Henry, M.O.; Deicher, M.; Magerle, R.; McGlynn, E.; Stötzler, A. Photoluminescence analysis of semiconductors using radioactive isotopes. *Hyperfine Interact.* **2000**, *129*, 443–460. [CrossRef]
268. Stötzler, A.; Weissenborn, R.; Deicher, M.; The ISOLDE Collaboration. Identification of Ag and Cd in photoluminescence in ^{111}Ag-doped GaN. *Phys. B* **1999**, *273–274*, 144–147. [CrossRef]
269. Monteiro, T.; Boemare, C.; Soares, M.J.; Alves, E.; Liu, C. Green and red emission in Ca implanted GaN samples. *Phys. B* **2001**, *308–310*, 42–46. [CrossRef]
270. Shen, J.-X.; Wickramaratne, D.; Dreyer, C.E.; Alkauskas, A.; Young, E.; Speck, J.S.; Van de Walle, C.G. Calcium as a nonradiative recombination center in InGaN. *Appl. Phys. Express* **2017**, *10*, 021001. [CrossRef]
271. Lyons, J.L.; Wickramaratne, D.; Van de Walle, C.G. A first-principles understanding of point defects and impurities in GaN. *J. Appl. Phys.* **2021**, *129*, 111101. [CrossRef]
272. Eider, E.; Grimmeiss, H.G. Optical Investigations of Zn, Hg and Li Doped GaN. *Appl. Phys.* **1974**, *5*, 275–279.
273. Van de Walle, C.G.; Neugebauer, J. Arsenic impurities in GaN. *Appl. Phys. Lett.* **2000**, *76*, 1009–1011. [CrossRef]
274. Mattila, T.; Zunger, A. Deep electronic gap levels induced by isovalent P and As impurities in GaN. *Phys. Rev. B* **1998**, *58*, 1367–1373. [CrossRef]
275. Gil, B.; Morel, A.; Taliercio, T.; Lefebre, P.; Foxon, C.T.; Winser, A.J.; Novikov, S.V. Carrier relaxation dynamics for As defects in GaN. *Appl. Phys. Lett.* **2001**, *79*, 69–71. [CrossRef]
276. Li, X.; Kim, S.; Reuter, E.E.; Bishop, S.G.; Coleman, J.J. The incorporation of arsenic in GaN by metalorganic chemical vapor deposition. *Appl. Phys. Lett.* **1998**, *72*, 1990–1992. [CrossRef]
277. Jin, S.R.; Ramsteiner, M.; Grahn, H.T.; Ploog, K.H.; Zhu, Z.Q.; Shen, D.X.; Li, A.Z.; Metev, P.; Guido, L.J. Suppression of yellow luminescence in As-doped GaN epilayers grown by metalorganic chemical vapor deposition. *J. Cryst. Growth* **2000**, *212*, 56–60. [CrossRef]
278. Guido, L.J.; Mitev, P.; Gherasimova, M.; Gaffey, B. Electronic properties of arsenic-doped gallium nitride. *Appl. Phys. Lett.* **1998**, *72*, 2005–2007. [CrossRef]
279. Sierakowski, K.; Jakiela, R.; Jaroszynski, P.; Fijalkowski, M.; Sochacki, T.; Iwinska, M.; Turek, M.; Uedono, A.; Reshchikov, M.A.; Bockowski, M. Analysis of Zn diffusion in various crystallographic directions of GaN grown by HVPE. *Mater. Sci. Semicond. Process.* **2023**, *167*, 107808. [CrossRef]
280. Skromme, B.J.; Martinez, G.L.; Suvkhanov, A.; Krasnobaev, L.; Poker, D.B. Optical characterization of acceptor implantation in GaN. In *High-Speed Compound Semiconductor Devices for Wireless Applications and State-of-the-Art Program on Compound Semicon-*

ductors (XXXIII); Baca, A.G., Kopf, R.F., Eds.; The Electrochemical Society, Inc.: Pennington, NJ, USA, 2000; Volume 2000-18, pp. 120–131, ISBN 1-56677-285-0.
281. Zhao, F.; Turiansky, M.E.; Alkauskas, A.; Van de Walle, C.G. Trap-Assisted Auger-Meitner Recombination from First Principles. *Phys. Rev. Lett.* **2023**, *131*, 056402. [CrossRef] [PubMed]
282. Espenlaub, A.C.; Myers, D.J.; Young, E.C.; Marcinkevičius, S.; Weisbuch, C.; Speck, J.S. Evidence of trap-assisted Auger recombination in low radiative efficiency MBE-grown III-nitride LEDs. *J. Appl. Phys.* **2019**, *126*, 184502. [CrossRef]
283. Lähnemann, J.; Kaganer, V.M.; Sabelfeld, K.K.; Kireeva, A.E.; Jahn, U.; Chèze, C.; Calarco, R.; Brandt, O. Carrier Diffusion in GaN: A Cathodoluminescence Study. III. Nature of Nonradiative Recombination at Threading Dislocations. *Phys. Rev. Appl.* **2022**, *17*, 024019. [CrossRef]
284. Xu, Z.; Daeumer, M.; Cho, M.; Yoo, J.-H.; Detchprohm, T.; Bakhtiary-Noodeh, M.; Shao, Q.; Laurence, T.A.; Key, D.; Letts, E.; et al. Breakdown characteristics analysis of kV-class vertical GaN PIN rectifiers by wafer-level sub-bandgap photoluminescence mapping. *J. Appl. Phys.* **2024**, *135*, 205704. [CrossRef]
285. Pauc, N.; Phillips, M.R.; Aimez, V.; Drouin, D. Carrier recombination near threading dislocations in GaN epilayers by low voltage cathodoluminescence. *Appl. Phys. Lett.* **2006**, *89*, 161905. [CrossRef]
286. Shiozaki, N.; Hashizume, T. Improvements of electronic and optical characteristics of n-GaN-based structures by photoelectrochemical oxidation in glycol solution. *J. Appl. Phys.* **2009**, *105*, 064912. [CrossRef]
287. Martinez, G.L.; Curiel, M.R.; Skromme, B.J.; Molnar, R.J. Surface recombination and sulfide passivation of GaN. *J. Electron. Mat.* **2000**, *29*, 325–331. [CrossRef]
288. Liu, W.; Sun, X.; Zhang, S.; Chen, J.; Wang, H.; Wang, X.; Zhao, D.; Yang, H. Photoluminescence degradation in GaN induced by light enhanced surface oxidation. *J. Appl. Phys.* **2007**, *102*, 076112. [CrossRef]
289. Pfüller, C.; Brandt, O.; Grosse, F.; Flissikowski, T.; Cheze, C.; Consonni, V.; Geelhaar, L.; Grahn, H.T.; Riechert, H. Unpinning the Fermi level of GaN nanowires by ultraviolet radiation. *Phys. Rev. B* **2010**, *82*, 045320. [CrossRef]
290. Reshchikov, M.A. Strong suppression of the yellow luminescence in GaN in air ambient. *Appl. Phys. Lett.* **2006**, *89*, 232106. [CrossRef]
291. Reshchikov, M.A.; Foussekis, M.; Baski, A.A. Surface photovoltage in undoped *n*-type GaN. *J. Appl. Phys.* **2010**, *107*, 113535. [CrossRef]
292. Reshchikov, M.A.; Sabuktagin, S.; Johnstone, D.K.; Morkoç, H. Transient photovoltage in GaN as measured by atomic force microscope tip. *J. Appl. Phys.* **2004**, *96*, 2556–2560. [CrossRef]
293. Barbet, S.; Aubry, R.; di Forte-Poisson, M.A.; Jacquet, J.-C.; Deresmes, D.; Melin, T.; Theron, D. Surface potential of n- and p-type GaN measured by Kelvin force microscopy. *Appl. Phys. Lett.* **2008**, *93*, 212107. [CrossRef]
294. Wolkenstein, T.; Peka, G.P.; Malakhov, V.V. The influence of adsorption on the luminescence of semiconductors. Part II. Exciton luminescence. *J. Lumin.* **1972**, *5*, 261–268. [CrossRef]
295. Kumakura, K.; Makimoto, T.; Kobayashi, N.; Hashizume, T.; Fukui, T.; Hasegawa, H. Minority carrier diffusion length in GaN: Dislocation density and doping concentration dependence. *Appl. Phys. Lett.* **2005**, *86*, 052105. [CrossRef]
296. Matys, M.; Adamowicz, B.; Kachi, T.; Hashizume, T. Effect of carrier drift-diffusion transport process on thermal quenching of photoluminescence in GaN. *J. Phys. D: Appl. Phys.* **2021**, *54*, 055106. [CrossRef]
297. Foussekis, M.A.; Baski, A.A.; Reshchikov, M.A. Electrical and optical properties of GaN studied by surface photovoltage and photoluminescence. *Phys. Stat. Sol. C* **2011**, *8*, 2148–2150. [CrossRef]
298. Foussekis, M.; McNamara, J.D.; Baski, A.A.; Reshchikov, M.A. Temperature-dependent Kelvin probe measurements of band bending in p-type GaN. *Appl. Phys. Lett.* **2012**, *101*, 082104. [CrossRef]
299. Long, J.P.; Bermudez, V.M. Band bending and photoemission-induced surface photovoltages on clean *n*- and *p*-GaN (0001) surfaces. *Phys. Rev. B* **2002**, *66*, 121308. [CrossRef]
300. Curie, D.; Garlick, G.F.J. *Luminescence in Crystals*; Methuen and Co., Ltd.: London, UK, 1963; 332p.
301. Riehl, N. Intrinsic defects and luminescence in II-VI compounds. *J. Lumin.* **1981**, *24/25*, 335–342. [CrossRef]
302. Zvanut, M.E.; Paudel, S.; Glaser, E.R.; Iwinska, M.; Sochacki, T.; Bockowski, M. Incorporation of Carbon in Free-Standing HVPE-Grown GaN Substrates. *J. Electron. Mater.* **2019**, *48*, 2226–2232. [CrossRef]
303. Zvanut, M.E.; Paudel, S.; Sunay, U.R.; Willoughby, W.R.; Iwinska, M.; Sochacki, T.; Bockowski, M. Charge transfer process for carbon-related center in semi-insulating carbon-doped GaN. *J. Appl. Phys.* **2018**, *124*, 075701. [CrossRef]
304. Paudel, S.; Zvanut, M.E.; Iwinska, M.; Sochacki, T.; Bockowski, M. A Deep Carbon-Related Acceptor Identified through Photoinduced Electron Paramagnetic Resonance. *Phys. Stat. Sol. B* **2020**, *257*, 1900593. [CrossRef]
305. Hofmann, D.M.; Kovalev, D.; Steude, G.; Meyer, B.K.; Hoffmann, A.; Eckey, L.; Heitz, R.; Detchprom, T.; Amano, H.; Akasaki, I. Properties of the yellow luminescence in undoped GaN epitaxial layers. *Phys. Rev. B* **1995**, *52*, 16702–16706. [CrossRef] [PubMed]
306. Honda, U.; Yamada, Y.; Tokuda, Y.; Shiojima, K. Deep levels in n-GaN doped with carbon studied by deep level and minority carrier transient spectroscopies. *Jap. J. Appl. Phys.* **2012**, *51*, 04DF04. [CrossRef]
307. Look, D.C. Defect-Related Donors, Acceptors, and Traps in GaN. *Phys. Stat. Sol. B* **2001**, *228*, 293–302. [CrossRef]

308. Horita, M.; Narita, T.; Kachi, T.; Suda, J. Nitrogen displacement-related electron traps in n-type GaN grown on a GaN freestanding substrate. *Appl. Phys. Lett.* **2021**, *118*, 012106. [CrossRef]
309. Endo, M.; Horita, M.; Suda, J. Hole traps related to nitrogen displacement in p-type GaN grown by metalorganic vapor phase epitaxy on freestanding GaN. *Appl. Phys. Lett.* **2022**, *120*, 142104. [CrossRef]
310. Zajac, M.; Kaminski, P.; Kozlowski, R.; Litwin-Staszewska, E.; Piotrzkowski, R.; Grabianska, K.; Kucharski, R.; Jakiela, R. Formation of Grown-In Nitrogen Vacancies and Interstitials in Highly Mg-Doped Ammonothermal GaN. *Materials* **2024**, *17*, 1160. [CrossRef]
311. Narita, T.; Horita, M.; Tomita, K.; Kachi, T.; Suda, J. Why do electron traps at EC-0.6 eV have inverse correlation with carbon concentrations in n-type GaN layer? *Jap. J. Appl. Phys.* **2020**, *59*, 105505. [CrossRef]
312. Albrecht, F.; Reislöhner, U.; Hülsen, C.; Witthuhn, W.; Grillenberger, J.; Dietrich, M.; the ISOLDE collaboration. Observation of a Be-correlated donor state in GaN. *Appl. Phys, Lett.* **2004**, *84*, 3876–3878. [CrossRef]
313. Polyakov, A.Y.; Lee, I.-H. Deep traps in GaN-based structures as affecting the performance of GaN devices. *Mater. Sci. Eng. R Rep.* **2015**, *94*, 1–56. [CrossRef]
314. Bisi, D.; Meneghini, M.; De Santi, C.; Chini, A.; Dammann, M.; Brückner, P.; Mikulla, M.; Meneghesso, G.; Zanoni, E. Deep-Level Characterization in GaN HEMTs-Part I: Advantages and Limitations of Drain Current Transient Measurements. *IEEE Trans. Electron. Devices* **2013**, *60*, 3166–3175. [CrossRef]
315. Stötzler, A.; Weissenborn, R.; Deicher, M.; The ISOLDE Collaboration. Identification of As, Ge and Se Photoluminescence in GaN Using Radioactive Isotopes. *MRS Internet J. Nitride Semicond. Res.* **2000**, *5*, 990–996. [CrossRef]
316. Stötzler, A.; Deicher, M.; The ISOLDE Collaboration. Photoluminescence in platinum doped GaN. *Phys. B* **2003**, *340–342*, 377–380. [CrossRef]
317. Neugebauer, J.; Van de Walle, C.G. Chemical trends for acceptor impurities in GaN. *J. Appl. Phys.* **1999**, *85*, 3003–3005. [CrossRef]
318. Freysoldt, C.; Grabowski, B.; Hickel, T.; Neugebauer, J.; Kresse, G.; Janotti, A.; Van de Walle, C.G. First-principles calculations for point defects in solids. *Rev. Mod. Phys.* **2014**, *86*, 253–305. [CrossRef]
319. Heyd, J.; Scuseria, G.E.; Ernzerhof, M. Hybrid functionals based on a screened Coulomb potential. *J. Chem. Phys.* **2003**, *118*, 8207–8215. [CrossRef]
320. Nichols, L.R.; Li, G.; Yu, Y.; Jiang, J.; O'Hara, A.; Barmparis, G.D.; Pantelides, S.; Zhang, X.-G. Multiphonon carrier capture by defects in semiconductors. *Phys. Rev. B* **2025**, *111*, 045201. [CrossRef]
321. Deák, P.; Aradi, B.; Frauenheim, T.; Janzén, E.; Gali, A. Accurate defect levels obtained from the HSE06 range-separated hybrid functional. *Phys. Rev. B* **2010**, *81*, 153203. [CrossRef]
322. Freysoldt, C.; Neugebauer, J.; Van de Walle, C.G. Fully Ab Initio Finite-Size Corrections for Charged-Defect Supercell Calculations. *Phys. Rev. Lett.* **2009**, *102*, 016402. [CrossRef] [PubMed]
323. Freysoldt, C.; Neugebauer, J.; Van de Walle, C.G. Electrostatic interactions between charged defects in supercells. *Phys. Stat. Sol. B* **2010**, *248*, 1067–1076. [CrossRef]
324. Meneghini, M.; De Santi, C.; Abid, I.; Buffolo, M.; Cioni, M.; Abdul Khadar, R.; Nela, L.; Zagni, N.; Chini, A.; Medjdoub, F.; et al. GaN-based power devices: Physics, reliability, and perspectives. *J. Appl. Phys.* **2021**, *130*, 181101. [CrossRef]